Max-Planck-Institut für Metallforschung
Stuttgart

The Initial Stages of the Oxidation of Zirconium

Andrey Lyapin

Dissertation
an der
Universität Stuttgart

Bericht Nr.169
April 2005

The Initial Stages of the Oxidation of Zirconium

von der Fakultät Chemie der Universität Stuttgart
zur Erlangung der Würde eines Doktors der
Naturwissenschaften (Dr. rer. nat.) genehmigte Abhandlung

vorgelegt von

Andrey Lyapin

aus St.-Petersburg/Russland

Hauptberichter:	Prof. Dr. Ir. E. J. Mittemeijer
Mitberichter:	Prof. Dr. Dr. h. c. M. Rühle
Mitprüfer:	Prof. Dr. F. Aldinger
Tag der Einreichung:	27.01.2005
Tag der mündlichen Prüfung:	27.04.2005

MAX-PLANCK-INSTITUT FÜR METALLFORSCHUNG STUTTGART
INSTITUT FÜR METALLKUNDE DER UNIVERSITÄT STUTTGART

Stuttgart 2005

Contents

Chapter 1

General introduction

1.1. Background

The reaction of a metal surface with oxygen is one of the solid-gas reactions which has great scientific and technological interest due to its importance in numerous application areas such as catalysis, microelectronics, surface coatings and corrosion protection. Oxidation of metals is often associated with corrosion, which causes unwanted destruction and loss of metal. However, upon contact with an oxygen-containing gas atmosphere, many metals (e.g. Al, Zn, Mg, Fe and Zr) form a thin protective oxide layer on their surface, which isolates the metal from its gaseous environment, thereby protecting the underlying material from further oxidation. The chemical composition, morphology and microstructure of the grown oxide film have a direct bearing to a variety of important properties such as: corrosion resistance, friction, adhesion and dielectric capacity etc. Therefore, thin metal-oxide films also play an important role in the production of, for example, electronic devices (such as contacts and integrated circuits) and gas sensors for gas-impurity measurement.

Oxidation of a bare metal surface is a very complex process, which can be subdivided into several different steps: oxygen molecule impingement from the gas phase, physisorption, dissociation and chemisorption of oxygen molecules, initial place exchange between oxygen and metal atoms, oxide nucleation, and continued oxide-film growth by charged particle transport through the developing oxide film (see Fig. 1.1). Impurities, the crystallographic structures of the oxide and the underlying metal substrate, the morphology, the chemical composition and defect structure of the oxide film, the mechanisms of ion and electron movement in the oxide, and the oxidation conditions (e.g. temperature and oxygen partial pressure), all play a vital role in the oxidation process [1-4]. In some cases, the oxidation process is further complicated due to additional processes, which take place upon oxidation, such as the formation of intermediate non-stoichiometric oxides and/or, especially at elevated temperatures, the dissolution of oxygen into the metal substrate associated with a partial decomposition of the oxide film [5].

This study addresses the mechanisms governing the growth kinetics, chemical composition, morphology and microstructure of zirconium-oxide films grown by dry, thermal oxidation of polycrystalline zirconium substrates at different oxidation conditions (e.g. partial oxygen pressure and temperature).

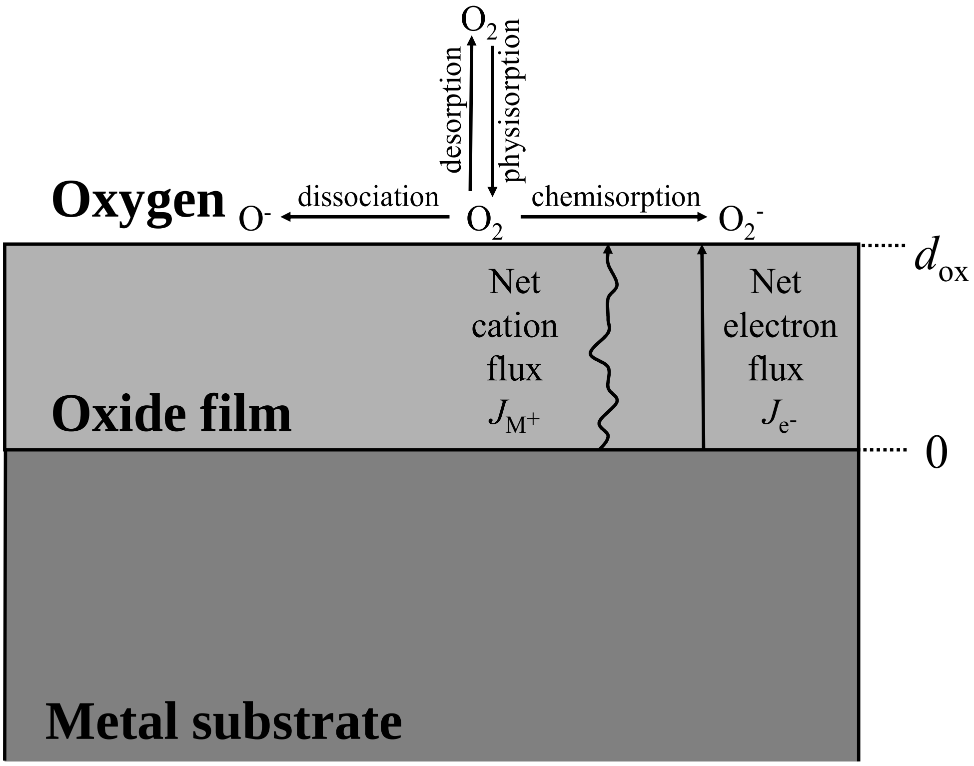

Figure 1.1. Schematic illustration of some processes involved during the initial and subsequent stages of dry, thermal oxidation of a bare metal substrate. In the case depicted here, continuing oxide-film growth is realised by the coupled currents of cationic and electronic species. The total oxide-film thickness, net cation flux and net electron flux are denoted with d_{ox}, J_{M+} and J_{e-}, respectively.

1.2. Zirconium and zirconium oxide

Zirconium appears in two crystalline forms: the hexagonal α-form (stable up to 1135 K) and the face-centred cubic β-form (stable above 1135 K). Pure zirconium is ductile and can be readily worked by forging, rolling into sheets and drawing. The presence of oxygen, nitrogen, carbon and hydrogen strongly affect the properties of zirconium, which therefore depend upon the method of production of the metal. Zirconium is stable in water, air, acids (except hydrofluoric and concentrated sulphuric acids) at room temperature, but actively absorbs gases (like O_2 and H_2) at elevated temperatures (> 500 K) [6].

Zirconium oxide appears in three crystalline forms: the monoclinic phase at low temperatures, the tetragonal phase above 1400 K and the cubic phase above 2600 K [7]. Both the monoclinic and tetragonal phases can be obtained by distortion of the simple cubic structure. In general, at room temperature crystalline zirconium oxide exists in the monoclinic phase, however, the cubic phase can be “stabilized” by the addition of substitutional cations, such as Ca^{2+}, Mg^{2+} and Y^{3+} [8]. Further, it is noted that a metastable, amorphous Zr-oxide phase has also been reported in the literature for the initial, thermal oxidation of Zr substrates at low temperatures (up to about 573 K) (as observed by high-resolution transmission electron microscopy in Ref. [9]).

Both zirconium and zirconium oxide are technologically important materials. Due to their specific physical and chemical properties, they are widely used in a large number of application areas (cf. Refs. [6, 10]). For example, Zr metal is used in the nuclear industry for cladding fuel elements, since it has a low absorption cross section for neutrons. Zirconium is used extensively by the chemical industry due to high resistance to corrosion by many common acids and alkalis, and by seawater. The metal is also used as an alloying agent in steel, and as a "getter" in vacuum tubes and in lamp filaments. Zirconium oxide is an important wide band gap transition metal oxide. Its current applications range from jewellery, semiconductor substrates, fuel cells and oxygen sensors to nuclear fuel rods (cf. Refs. [6, 11]). Recently, zirconium-oxide related research has received an additional boost due to an intensive search for new dielectric materials capable of substituting silicon dioxide in its role as gate dielectric in many microelectronic devices [10, 12].

Up to date, the initial oxidation of zirconium has been investigated using different surface analysis techniques at different oxidation conditions (cf. Refs. [13-17]). However, the processes that occur and the changes that take place at the metal surface, in the developing oxide film, and at the metal/oxide and oxide/gas interfaces during the initial and subsequent stages of oxide-film growth are still poorly understood. For example, the effect of temperature and partial oxygen pressure on the oxide-film growth kinetics and the developing oxide-film microstructure, such as the formation of different intermediate, non-stoichiometric oxides, is still unclear.

1.3. Methods of characterization

An ultra-high-vacuum (UHV) chamber in combination with in situ surface-sensitive analytical techniques are prerequisites to investigate the initial oxidation of bare metal surfaces. In the present work, the combination of two powerful surface-sensitive analytical techniques, namely angle-resolved X-ray photoelectron spectroscopy and in situ multi-wavelength ellipsometry, is used to study the initial and subsequent stages of oxide nucleation and growth on bare Zr substrates.

1.3.1. AR-XPS

Angle-resolved X-ray photoelectron spectroscopy (AR-XPS) is based on the photon-induced emission of electrons with kinetic energies characteristic for the elements they originate from. From the measured electron-energy spectrum of an oxidized metal, information about the oxide-film thickness, composition and chemical state can be obtained for oxide-film thicknesses of the order of the attenuation length of the emitted photoelectrons in the oxide (i.e. up to about 5 nm). The angle-resolved feature of the state-of-the-art XPS instrument employed in the current investigation is based on the simultaneous recording of the emitted photoelectrons at various detection angles Θ (with respect to the sample surface). Since the analysis depth is defined by the effective attenuation length (EAL, symbol λ^{eff}) of the detected photoelectrons in the solid times the cosine of the detection angle Θ, i.e. $\lambda^{eff}\cos\Theta$, it follows that different depths within the oxide film are probed for different detection angles Θ. An angle-resolved measurement of the oxidized metal therefore allows the investigation of the depth distribution of the various chemical species within the oxide film. As shown in Chapters 3 and 4, angle-resolved XPS analysis of the bare and oxidized metal substrates has been applied to determine the thickness, chemical composition and constitution of the developing oxide-films.

The accuracy in the quantitative analysis of recorded photoelectron spectra depends on the method used for the calculation (and subsequent subtraction) of the background of inelastically scattered electrons to the measured spectrum. Usually for the case of photoelectron spectra constituted of a single spectral component, the inelastic background is removed using arbitrary methods, such as a linear background or a Shirley-type background [18]. However, if the measured spectrum contains two or more overlapping peaks, as for the case of a spectrum of an oxidized metal (which is constituted of at least one metallic and one or more oxidic components) (see Fig. 1.2), each peak provides its own contribution to the background of inelastically scattered electrons, and the aforementioned arbitrary methods for background subtraction are no longer valid. Therefore, a procedure for the evaluation of the Zr 3*d* XPS spectra of zirconium metal and zirconium oxide has been developed that is based on the reconstruction of the reference spectra by a convolution of physically realistic functions for the X-ray energy distribution, the core-level main peak, the cross-sections for intrinsic and extrinsic excitations and instrumental broadening (Chapter 2). This procedure was further modified for the quantification of the spectra of the oxidized Zr substrate (Chapter 3).

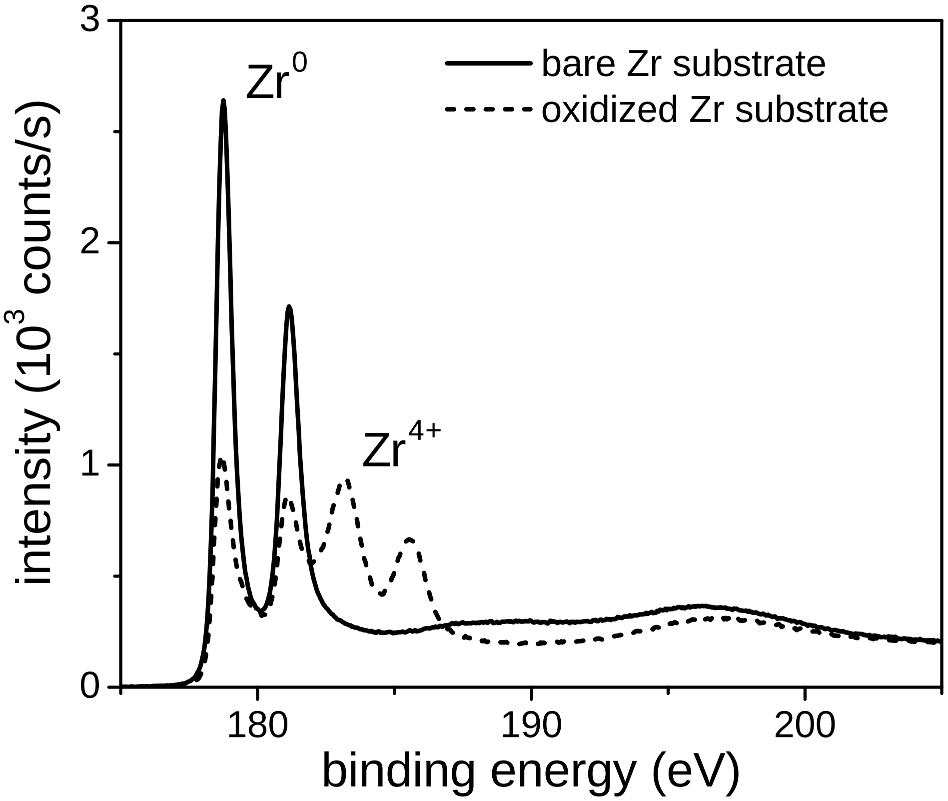

Figure 1.2. Measured Zr 3*d* XPS spectra, as recorded from a bare Zr substrate (solid line) and the Zr substrate after dry, thermal oxidation for 3600 s at 373 K and $pO_2 = 2\times10^{-6}$ Pa (dashed line). The Zr 3*d* spin-orbit doublets of metallic and oxidic Zr 3*d* peaks have been indicated as Zr^0 and Zr^{4+}, respectively.

1.3.2. In situ ellipsometry

In situ ellipsometry provides a dynamic, non-destructive analysis of the oxide film during growth (i.e. the specimen can be monitored continuously as oxidation proceeds). In the present work, in situ ellipsometry was applied to determine the oxide-film growth kinetics and the development of the oxide-film constitution as a function of the partial oxygen pressure (Chapter 3) and the oxidation temperature (Chapter 4).

The principle of ellipsometry is based on the measurement of the change in the polarization state of light reflected from the surface of the sample [19]. The measured parameters, Ψ and Δ, represent the changes in amplitude and phase of the polarized light, reflected from the analyzing surface. More specific, Ψ is the angle whose tangent equals the ratio of the amplitude attenuation (or magnification) upon reflection for the p and s polarizations (i.e. the components of the electric field vector of the polarized light vibrating in the plane of incidence and perpendicular to it, respectively); Δ is the difference between the phase shifts experienced upon reflection by the p and s polarizations.

The multi-wavelength ellipsometer used in the present work is equipped with an incident Xe light source, covering a wavelength range from 250 nm to 850 nm, thereby obtaining information on the variation of Ψ and Δ as a function of both the oxidation time and the wavelength. From such measurements recorded from the oxidizing Zr substrate, the oxide-film thickness and constitution, as well as the optical constants of the metal and the oxide phase(s) involved, were determined as a function of the oxidation conditions (oxidation time, temperature and pO_2).

1.4. Modelling of the oxide-film growth kinetics

A large number of theories and physical models have been put forward to describe the oxide-film growth kinetics for the oxidation of bare metal surfaces at low temperatures (of, say, up to about 573 K; see e.g. Refs. [1-4, 20-24]). Most of these theories assume that after formation of a ‘closed’ oxide film (i.e. covering the entire metal substrate), continued oxide-film growth is realised by the transport of the charged species (i.e. cations, anions and electrons) through the developing oxide film.

A comprehensive treatment of low-temperature oxidation should consider at least one electronic and one ionic current in the so-called coupled-currents conception, which is the central point of the theoretical model put forward by Fromhold and Cook [23, 24]. The coupled-current constraint implies that no net electric charge is transported through the oxide-film during growth (i.e. the sum of all currents of charged species equals zero). By considering various mechanisms for the electron transport (e.g. electron transport by tunnelling and by thermal emission) in combination with the electric-field enhanced diffusion of cations and/or anions through the developing oxide film, theoretical oxide-film growth curves can be calculated (under the coupled-current constraint). In this work the initial, thermal oxidation of a bare Zr substrate is described by adopting a coupled-currents constraint for the fluxes of Zr cations and electrons (by both tunnelling and thermionic emission) in a homogeneous surface-charge field comprising the developing oxide film (Chapter 5).

1.5. Outline

In Chapter 2, a new method for the quantitative analysis of the 3*d* XPS spectra of zirconium and zirconium oxide is presented, which allows the determination of the intrinsic and extrinsic contributions to the measured reference spectra. In the Chapters 3 and 4, in situ ellipsometry and angle-resolved X-ray photoelectron spectroscopy were used to determine the growth kinetics and developing microstructure (i.e. structure, constitution, morphology and chemical composition) of thin (< 6 nm) zirconium-oxide films grown on polycrystalline zirconium substrates by dry, thermal oxidation at various partial oxygen pressures (1.3×10^{-6} – 1.3×10^{-4} Pa) and temperatures (305 – 773 K). Finally, to establish the underlying mechanisms governing the oxide-film growth on the Zr substrates, the kinetics of oxide-film growth of a bare Zr substrate was modelled as a function of time, temperature and partial oxygen pressure (Chapter 5).

Chapter 2

Quantitative analysis of the X-ray photoelectron spectra of zirconium and zirconium oxide.

A. Lyapin, P.C.J. Graat

Abstract

A procedure for evaluation of XPS spectra is presented that allows the determination of intrinsic and extrinsic contributions to the spectra. It is based on convolution of physically realistic functions for the X-ray energy distribution, the core-level main peak, the cross-sections for intrinsic and extrinsic excitations and instrumental broadening. Surface effects have been accounted for by describing the material as a bulk substrate covered with a surface layer of the same material but with different excitation properties. The procedure has been applied to angle resolved Zr 3*d* spectra of pure zirconium and pure zirconium oxide. The results show that in the case of Zr about 28% and in the case of ZrO_2 about 21% of the total intrinsic intensity of the Zr 3*d* spectrum is not contained in the main peak.

2.1. Introduction

The spectra obtained with X-ray photoelectron spectroscopy (XPS) contain contributions originating from the X-ray energy distribution, the intrinsic core-level excitations, the extrinsic energy losses and the instrumental factors. Usually one is interested in the intrinsic part of the spectrum and the standard procedure to obtain this part is by subtraction of a background, representing the extrinsic contribution of inelastically scattered electrons, from the main peak region. The remaining background-corrected main peak is used then for further analysis. However, an additional intrinsic contribution can arise at the high binding energy side of a peak due to coupling of the core hole with collective electron oscillations (plasmons). One way to conceive this coupling is that the conduction electrons are scattered into an excited state by the core hole. The required energy for this excitation must be supplied by the photoemission process, i.e. the photoelectron gets a lower kinetic energy and appears at a higher binding energy in the spectrum. Neglecting this contribution, which is not contained in the main peak, leads to falsified results, e.g. for composition or layer thickness, obtained from the spectra.

In a recent paper the intrinsic and extrinsic surface and bulk contributions to the 2*p* spectrum of Mg have been separated, by fitting the spectrum with physically realistic functions for the different contributions [25]. The material has thereby been considered as a substrate covered with a thin film of the same material, with possibly different electron energy loss properties of substrate and film. In this paper a similar procedure has been applied to angle-resolved XPS 3*d* spectra of Zr and ZrO_2.

It should be noted that the procedure used here is a spectrum reconstruction technique. Another way to treat the problem of extracting the intrinsic and extrinsic surface and bulk contributions from a photoelectron spectrum is by using a spectrum decomposition technique as has been introduced by Werner et al. [26, 27]. The advantage of their so-called direct deconvolution method is that no functions have to be adopted for the different contributions beforehand. The disadvantage of their method, as with any deconvolution technique, is that it is much more sensitive to noise in the data and that incorrect assumptions in the first stages of the deconvolution will propagate and can have a strong influence on the final stage of the deconvolution (i.e. the stage that gives the intrinsic spectrum).

2.2. Theory: calculation of the Zr 3*d* spectrum

The XPS Zr 3*d* spectra of Zr metal and ZrO_2 have been calculated as described below. Thereby largely the procedure introduced in Ref. [25] has been followed.

2.2.1. X-ray energy distribution

The spectral broadening caused by the natural energy spread of the incoming X-rays is described by a Lorentz function:

$$I_X(E) = \frac{1}{\pi \cdot (\gamma_X/2)} \cdot \frac{1}{\left(\frac{E_X}{(\gamma_X/2)}\right)^2 + 1} \tag{2.1}$$

where E_X is the photon energy relative to the energy of the Al Kα_1 line and γ_X is the full width at half maximum (FWHM) of the X-ray line. Since in this work monochromatic Al Kα_1 radiation has been used, the contributions of the Al Kα_2 and other X-ray satellites do not have to be considered.

2.2.2. Core level main peak

The Zr 3*d* core level is split into Zr $3d_{5/2}$ and Zr $3d_{3/2}$ levels. Thus the main peak is calculated as a sum of two lines:

$$I_M(E) = H_M \cdot I_{MP}(E) + a_{3d3} \cdot H_M \cdot I_{MP}(E - E_{3dS}) \tag{2.2}$$

where E is the electron binding energy, E_{3dS} is the core level splitting, H_M is height of the Zr $3d_{5/2}$ peak, a_{3d3} is area of Zr $3d_{3/2}$ peak relative to Zr $3d_{5/2}$ peak. For pure zirconium a Doniach-Sunjic function [28] can be used for the line shape $I_{MP}(E)$:

$$I_{MP}(E) = \frac{\Gamma(1-\alpha_M) \cdot \cos\left(\frac{\pi \cdot \alpha_M}{2} + (1-\alpha_M) \cdot a\tan\left(\frac{E_M - E}{(\gamma_M/2)}\right)\right)}{\left((E_M - E)^2 + (\gamma_M/2)^2\right)^{(1-\alpha_M)/2}} \tag{2.3}$$

where Γ is the gamma function, E_M is the core level binding energy, γ_M is the FWHM of the line shape and α_M is the singularity index, determining the magnitude of asymmetric tail towards higher binding energies. Since the surface core level shift for Zr is 0 eV [29], a shift of the main peak originating from the surface region relative to that of the bulk region has not been considered. For pure zirconium oxide a Lorentz function (cf. Eq. (2.1)) can be used for the line shape $I_{MP}(E)$, i.e.: $I_{MP}(E) = 2 / (\pi\cdot\gamma_M)\cdot 1 / ((2 (E_M - E)/\gamma_M)^2 + 1)$, where E_M and γ_M have the same meaning as in Eq. (2.2). Like for Zr a surface core level shift has not been considered for ZrO_2. It might be argued that other line shapes, for example a Gauss shape, give theoretically a better description of the oxide main peak. However, for the purpose of the present paper it is mainly important that a good mathematical description of the main peak is obtained. By adopting a Lorentz function that is later convoluted with a Gauss function (to account for instrumental broadening; see below) a line shape is obtained that gives a better description of the experimental main peak than would be obtained with a Lorentz or Gauss function alone. Actually, the final results obtained for the relative intensities of the different contributions to the spectrum are not sensitive to the precise line shape used for the main peak, as long the shape gives a good description of the main peak.

2.2.3. Intrinsic energy loss

To obtain the contribution due to intrinsic excitations, $I_{Pi}(E)$, to the Zr 3*d* spectrum, the Zr 3*d* main peak is convoluted with the cross section for intrinsic excitation, $K_i(E_L)$, with E_L being the electron energy loss. The cross section $K_i(E_L)$ is unknown. In Ref. [25] it has been assumed that $K_i(E_L)$ can be described with the same function as the cross section for extrinsic plasmon excitation (see Eqs. (2.13) and (2.14) below). This assumption is applied here too. Additionally, $K_i(E_L)$ is represented in this work by a Lorentz function, i.e. $K_i(E_L) = 2 / (\pi\gamma_i) \cdot 1 / ((2 (E_L - E_{Li})/\gamma_i)^2 + 1)$, where E_{Li} is the position of the maximum and γ_i is the FWHM of the intrinsic loss function. In both cases the intrinsic contribution to the spectrum is given by:

$$I_{Pi,b}(E) = I_M(E) * b_b \cdot K_{i,b}(E_L) \quad \text{and} \quad I_{Pi,s}(E) = I_M(E) * b_s \cdot K_{i,s}(E_L) \tag{2.4}$$

for the bulk and surface region, respectively. The asterisk symbol represents a convolution, and b_b and b_s are the intensity ratios of the intrinsic bulk and surface loss peaks to the main peak, respectively. Only the 1st intrinsic loss is considered here; higher orders of intrinsic excitations are neglected. The total intrinsic Zr 3*d* excitation spectrum, $I_i(E)$, is then calculated as the sum of the main peak and the intrinsic loss peaks convoluted with the X-ray energy distribution:

$$I_{i,b}(E) = I_X(E) * \left(I_M(E) + I_{Pi,b}(E)\right) \quad \text{and} \quad I_{i,s}(E) = I_X(E) * \left(I_M(E) + I_{Pi,s}(E)\right) \tag{2.5}$$

for the bulk and surface regions, respectively.

2.2.4. Extrinsic energy loss

The contribution of extrinsic excitations to the Zr 3*d* spectrum has been calculated using the formalism, introduced by Werner [30-32]. This formalism gives exactly the same results as Tougaard's formalism [33] used in Ref. [25], but has the advantage that it allows faster calculation. In Werner's formalism the electrons reaching the surface of the sample are subdivided according to the number of inelastic scattering events they have undergone. Then, a spectrum, $I_{i+e,s}(E)$, comprising intrinsic and extrinsic contributions and originating from a surface region is given by:

$$I_{i+e,s}(E) = \sum_{n=0}^{\infty} P_{n,s} \cdot L_{n,s}(E_L) * I_{i,s}(E) \tag{2.6}$$

where $P_{n,s}$ are the so-called partial intensities, i.e. the relative contribution of n times inelastically scattered electrons to the spectrum, and $L_{n,s}(E_L)$ describes the probability for extrinsic energy loss E_L after n inelastic collisions. Considering the surface region as a layer with thickness D_s separated with a sharp interface from the bulk region and neglecting elastic scattering of electrons, the partial intensities are given by:

$$P_{n,s} = \int_0^{D_s} C_s \cdot \phi_{n,s}(z) \cdot dz = C_s \cdot \lambda_s \cdot \cos(\Theta) \cdot \left(1 - \sum_{j=0}^{n} \phi_{j,s}(D_s) \right) \tag{2.7}$$

where C_s is the concentration of the element considered in the surface region, λ_s is the inelastic mean free path (IMFP) of the electrons in the surface region, Θ is the detection angle relative to the surface normal and the so-called depth distribution function $\phi_{n,s}(z)$ for the surface region is given by:

$$\phi_{n,s}(z) = \frac{1}{n!} \cdot \left(\frac{z}{\lambda_s \cdot \cos(\Theta)} \right)^n \cdot \exp\left(- \frac{z}{\lambda_s \cdot \cos(\Theta)} \right) \tag{2.8}$$

where z is the depth below the surface. The partial loss functions, $L_{n,s}(E_L)$, for $n > 0$, are given by:

$$L_{n,s}(E_L) = L_{n-1,s}(E_L) * K_{e,s}(E_L) \tag{2.9}$$

where $K_{e,s}(E_L) = L_{1,s}(E_L)$ is the cross section for a single inelastic scattering event in the surface region (see below). For $n = 0$, $L_{0,s}(E_L) = 1$ for $E_L = 0$ and $L_{0,s}(E_L) = 0$ for $E_L > 0$.

For calculation of the spectrum $I_{i+e,b}(E)$ originating from the bulk region, both scattering in the bulk and in the surface region has to be considered. In that case:

$$I_{i+e,b}(E)=\sum_{n=0}^{\infty}\sum_{p=0}^{n}P_{p,n-p,b}\cdot L_{p,n-p}(E_L)*I_{i,b}(E) \tag{2.10}$$

where $P_{p,n\text{-}p,b}$ and $L_{p,n\text{-}p}(E_L)$ are the partial intensities and partial loss functions of electrons that have inelastically scattered p times in the bulk region and $n\text{-}p$ times in the surface region. The partial intensities $P_{p,n\text{-}p,b}$ are given by:

$$P_{p,n-p,b}=C_b\cdot\lambda_b\cdot\cos(\Theta)\cdot\phi_{n-p,s}(D_s) \tag{2.11}$$

where C_b is the concentration of the element considered in the bulk region, λ_b is the IMFP of the electrons in the bulk region and $\phi_{n\text{-}p,s}(D_s)$ is given by Eq. (2.8) with $z = D_s$. The partial loss functions $L_{p,n\text{-}p}(E_L)$ are given by:

$$L_{p,n-p}(E_L)=L_{p,b}(E_L)*L_{n-p,s}(E_L) \tag{2.12}$$

The partial loss function $L_{n\text{-}p,s}(E_L)$ of the surface region is given by Eq. (2.9); the partial loss function $L_{p,b}(E_L)$ of the bulk region is calculated likewise, i.e.: $L_{p,b}(E_L) = L_{p\text{-}1,b}(E_L) * K_{e,b}(E_L)$, with $K_{e,b}(E_L)$ being the cross section for a single inelastic scattering event in the bulk region (see below).

The cross section for extrinsic excitation $K_e(E_L)$, i.e. probability that an electron moving in the solid with energy E will lose the energy E_L, is given by [34, 35]:

$$K_e(E_L)=\frac{1}{\pi\cdot E\cdot a_0}\int_{k-}^{k+}\mathrm{Im}\left[-\frac{1}{\varepsilon(k,E_L)}\right]\cdot\frac{1}{k}\cdot dk \tag{2.13}$$

where $k=\sqrt{2m_e/\hbar^2}\sqrt{E}\pm\sqrt{E-E_L}$, a_0 = 0.053 nm is the Bohr radius and $\varepsilon(k,E_L)$ is the complex dielectric function of the solid which describes the response of the solid to the moving electron in term of energy and momentum transfers to the electron of the solid. The dielectric loss function can be described by Drude-Lindhard terms:

$$\mathrm{Im}\left(-\frac{1}{\varepsilon(k,E_L)}\right)=\sum_j\frac{A_j\cdot\gamma_j\cdot E_L}{\left[\left(E_{Le,j}+\left(\hbar^2k^2/2m\right)\right)^2-\left(E_L\right)^2\right]^2+\left(\gamma_j\cdot E_L\right)^2}\times\Theta(\hbar\omega-E_g) \tag{2.14}$$

where m is the electron mass, A_j, $E_{Le,j}$ and γ_j represent the magnitude, position and width of the individual loss peaks, respectively. The function $\Theta(\hbar\omega-E_g)$ has been included to describe the effect of an energy band gap, E_g, for zirconium oxide, so that $\Theta(\hbar\omega-E_g)=0$ if $\hbar\omega<E_g$ and $\Theta=1$ if $\hbar\omega>E_g$. To calculate the cross-sections the analytical solution of

Eqs. (2.13) and (2.14) from Ref. [35] has been used (see Appendix). After that the cross section has been normalised such that its total area (integral from $E_L = 0$ to ∞) is equal to a.

2.2.5. Instrumental broadening

The instrumental broadening can be described by a Gauss function:

$$I_G(E) = \frac{1}{\sqrt{\pi}\cdot(\gamma_G/2)}\cdot\exp\left(-\left(\frac{E}{(\gamma_G/2)}\right)^2\right) \tag{2.15}$$

where E is the detected electron energy relative to the true energy and γ_G is the FWHM.

2.2.6. Total spectrum

Finally, the total spectrum $I(E)$ is obtained by convolution of the sum of bulk and surface spectra with the instrumental broadening:

$$I(E) = \left(I_{i+e,b}(E) + I_{i+e,s}(E)\right) * I_G(E) \tag{2.16}$$

2.3. Experimental.

A piece of Zr has been cut from a zirconium crystal bar of 99.5% purity (Alfa Aesar). This piece has been melted using an arc melting furnace and subsequently cold rolled down to a thickness of 0.5 mm. A disc with a diameter of 10 mm has been punched out the foil obtained after cold rolling. The Zr disc has been ground successively by hand with SiC paper of decreasing grain size (15 μm to 8 μm grains) and polished using diamond paste of decreasing grain size (6 μm to 1 μm grains) on rotating disks with a smooth textile cover. As a lubricant, a mixture of ethanol, soap and distilled water has been used for all polishing procedures. After polishing the sample has been cleaned successively by ethanol, acetone and propanol in an ultrasonic bath and is introduced in the ultra high vacuum chamber of the XPS instrument. In the UHV chamber the sample has been sputter cleaned with 4 kV Ar^+ ions before and after annealing at 973 K during 45 minutes until no peaks due to other elements than Zr appeared in XPS survey spectra.

The ZrO_2 sample has been prepared by annealing a Zr sample that was obtained like described above at 973 K in an oxygen atmosphere ($pO_2 = 9.3\times10^4$ Pa). With X-ray diffraction it has been verified that a thick layer of monoclinic ZrO_2 has been formed at the surface of the sample. This sample has been introduced in the XPS instrument and measured with XPS without any further treatment.

XPS spectra have been recorded in a VG Thetaprobe XPS system using monochromatic Al Kα_1 radiation. The energy scale of the hemispherical analyser has been calibrated using the Ag 3$d_{5/2}$ peak set at 368.26 eV. The intensity scale has not been corrected for the analyser transmission function, but it has been verified that applying the transmission function supplied by the manufacturer had no significant influence on the results. The Zr 3*d* spectra of the Zr metal and the ZrO_2 layer have been measured in the binding energy range from 170 to 230 eV with a pass energy of 50 eV and a step size of 0.05 eV. Electrons have been detected simultaneously at detection angles of 23 to 83°, subdivided in 6 intervals of 10°. To keep the Zr surface free of oxygen the sample was sputter-cleaned between each measurement cycle. During measurement of the ZrO_2 layer the sample was (instead of sputter-cleaning) bombarded with low energy electrons to compensate for surface charging.

2.4. Results and discussion.

The main aim of this paper has been to determine the contribution of intrinsic energy losses to the Zr 3*d* spectra, so that a correct determination of the total intrinsic intensity of the spectra is possible for further quantitative analysis of the spectra (see Ref. [36]). This has been achieved by comparing theoretical spectra, calculated as described above in Sec. 2.2, with the experimental spectra. By varying the intrinsic contribution (b_b and b_s in Eq. (2.4)) and several other parameters it has been tried to obtain optimum values for these parameters. Before comparison of the calculated and experimental spectra, a constant background intensity equal to the average intensity in the range 170 – 170.5 eV has been subtracted from the experimental spectra.

The following fit parameters have been used: H_M, E_M, γ_M, α_M, E_{3dS} and a_{3d3}, describing the Zr 3*d* main peak for the pure metal (Eqs. (2.2) and (2.3)) and the same parameters except α_M for the Zr 3*d* main peak of the pure oxide layer (which, as mentioned in Sec. 2.2, is described by a Lorentz function).

For the intrinsic loss function the width, γ_i, and intensity relative to the main peak, b, have been used as fitting parameters (Eq. (2.4)). The same values have been used for the intrinsic energy losses in the bulk and the surface region, thus $\gamma_{i,b}=\gamma_{i,s}=\gamma_i$ and $b_b=b_s=b$. The positions of the intrinsic loss function, $E_{Li,b}$ and $E_{Li,s}$, have been taken equal to the positions of the extrinsic bulk plasmon peaks (see below).

Table 2.1. Parameters used for the calculation of the cross sections for inelastic scattering. The parameters have been obtained in Ref. [37] from REELS measurements using 500 eV electrons for Zr and 400 eV electrons for ZrO_2.

material	$E_{Le,j}$ (eV)	A_j (eV2)	γ_j (eV)	assignment
Zr	4.3	0.65	3	Zr 4*d* → Zr 4*d*
	8.5	5.0	4.5	Zr 4*d* → Zr 5*p*
	16.3	168	5.5	bulk plasmon
	30	5.0	5	Zr 4*p* → Zr 4*d*
	38	366	11.5	Zr 4*p* resonance
	52	33	14	Zr 4*s* → Zr 4*d*
ZrO_2	8.5	3.3	3.5	O 2*p* → Zr 4*d*
	14.3	63	4.3	bulk plasmon
	20.5	37	7	O 2*s* → Zr 4*d*
	26	110	8	O 2*p* → Zr 5*sp*
	34	8	2	Zr 4*p* → Zr 4*d*
	41	270	9	Zr 4*p* resonance
	57.5	65	13	O 4*s* → Zr 4*d*

The extrinsic cross-sections, $K_{e,b}(E)$ and $K_{e,s}(E)$, for the bulk and surface region, respectively (Eqs. (2.13) and (2.14)), have been calculated using data obtained by reflection electron energy loss spectroscopy (REELS) measurements [37]. These data have been reproduced in Table 2.1. In Ref. [37] an additional adjustable parameter has been introduced in Eq. (2.14) for the calculation of the cross section of the oxide. Since with this parameter relatively poor fits were obtained for the present XPS spectra it has been omitted here (i.e. set to 1 like for the metal in Ref. [37]). The positions $E_{Le,j}$ (see Table 2.1) have been multiplied with a factor f_{ELe} to allow for a small shift of the whole cross section. This factor as well as the total area a of the cross section have been used as fitting parameters. The band gap of ZrO_2 has been taken as 5.42 eV [38]. The same parameter values have been used for the surface and bulk extrinsic cross sections, with the exception of the position of loss peak that has been indicated as bulk plasmon peak in Table 2.1. For the calculation of the surface extrinsic cross section, $K_{e,s}(E)$, the position of this loss peak ($E_{Le,3}$ for the metal and $E_{Le,2}$ for the oxide, cf. Table 2.1) has been used as fitting parameter. Furthermore, the thickness of the

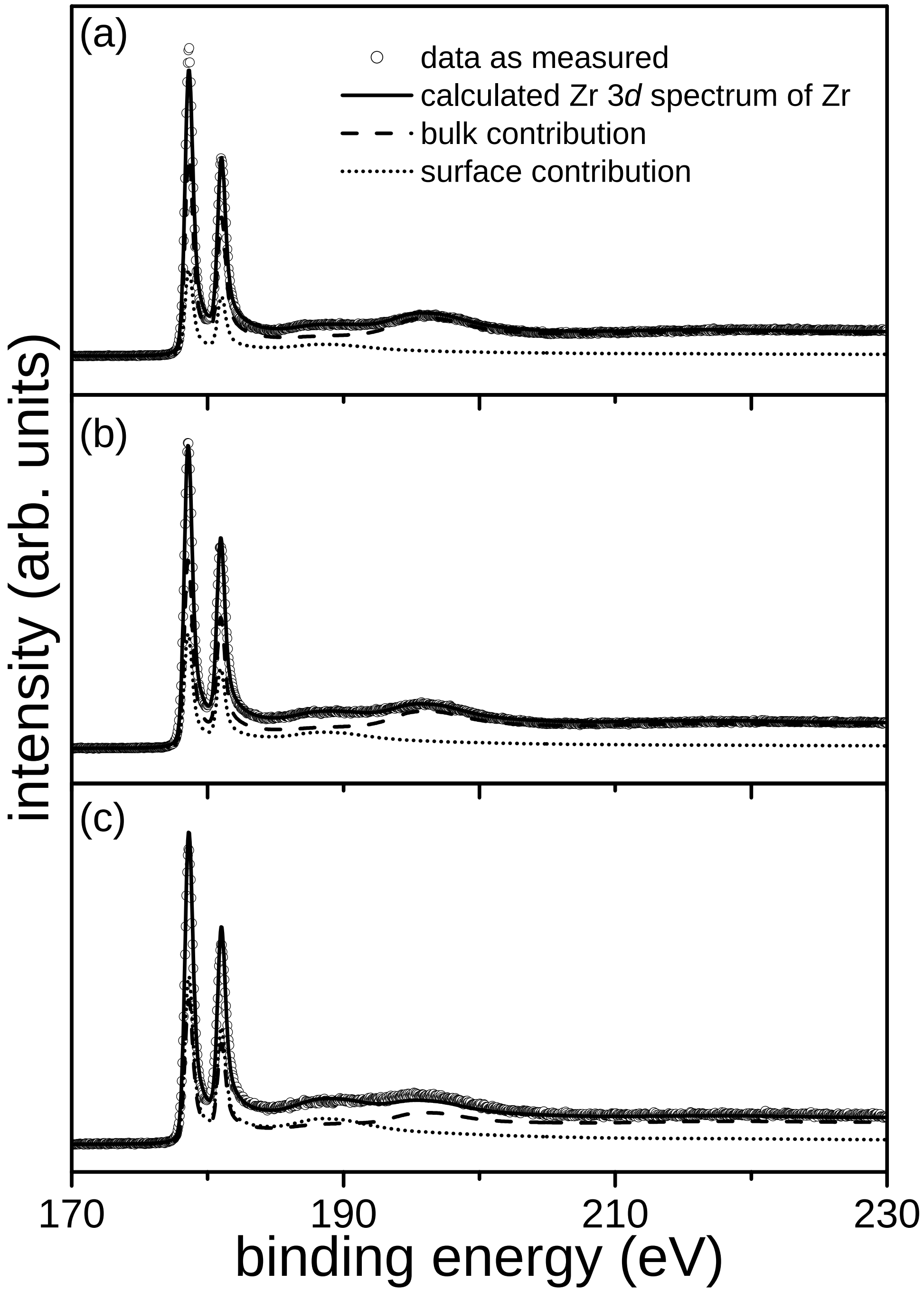

Figure 2.1. The experimental and calculated Zr 3*d* spectra for pure zirconium, for detection angles of 28 **(a)**, 58 **(b)** and 78 **(c)** degrees with respect to the surface normal.

surface region, D_s (Eqs. (2.7) and (2.11)) has been used as fitting parameter. The IMFP values (Eqs. (2.7), (2.8) and (2.11)) of Zr 3*d* electrons in Zr (2.54 nm) and ZrO_2 (2.39 nm) have been obtained from Ref. [39]. The same values have been taken for the bulk and the surface region. The values for the concentration of Zr (Eqs. (2.7) and (2.11)) have no influence on the fitting procedure as long as the same values are taken for the bulk and surface region.

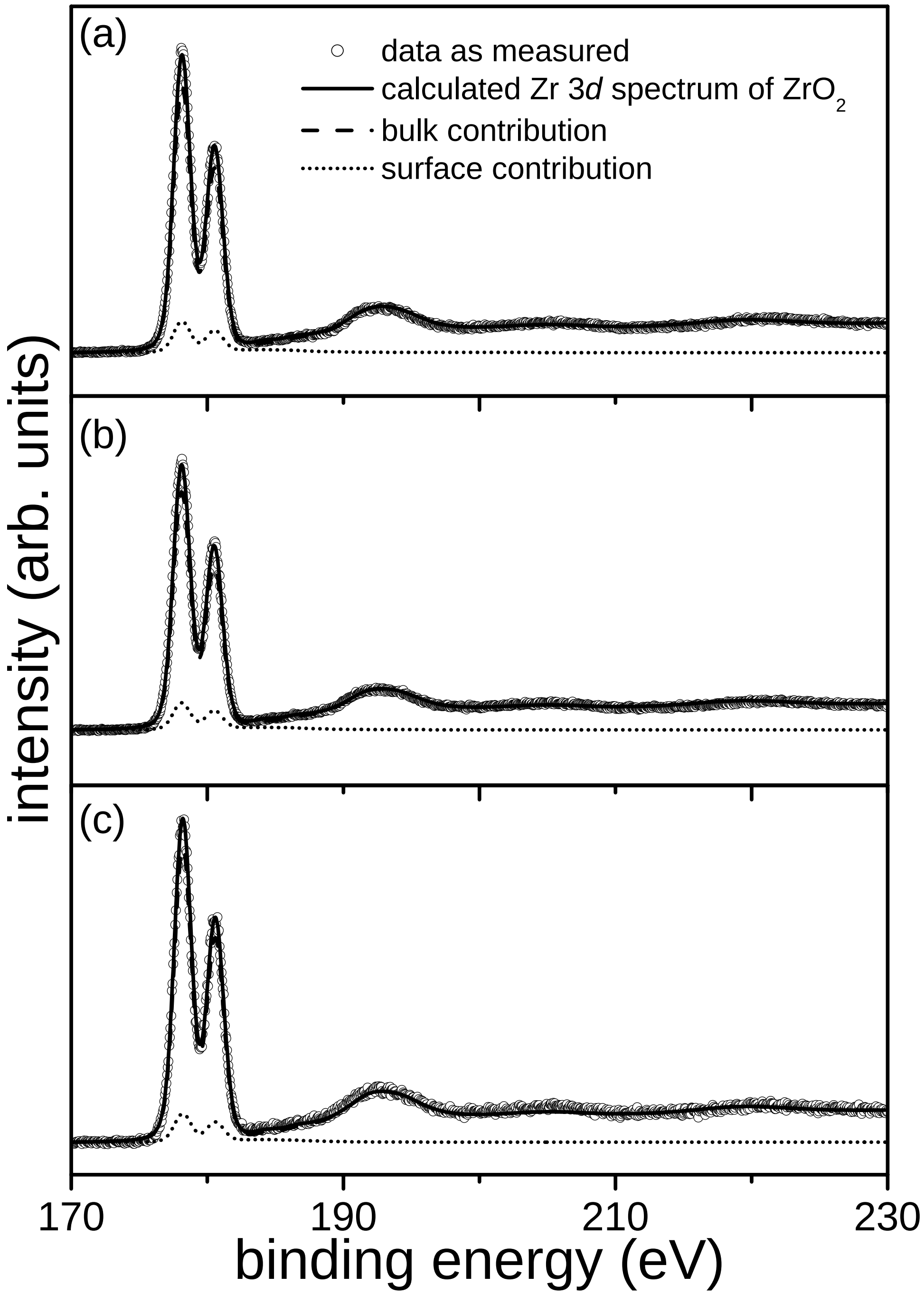

Figure 2.2. The experimental and calculated Zr 3*d* spectra for pure zirconium oxide, for detection angles of 28 **(a)**, 58 **(b)** and 78 **(c)** degrees with respect to the surface normal.

For the calculation of the extrinsic contribution up to 4 inelastic scattering events (Eqs. (2.6) and (2.10) were sufficient for the energy range considered (170 – 230 eV).

Since the instrumental broadening and the X-ray broadening are difficult to determine separately, a linear combination of the two broadening functions has been applied:

$$I_{GX}(E) = f_G \cdot I_G(E) + (1 - f_G) \cdot I_X(E) \tag{2.17}$$

Table 2.2. Resulting values of the fit parameters for the calculation of the Zr 3*d* spectra of Zr. The second column gives the results for the case that Eqs. (2.13) and (2.14) have been used to calculate the intrinsic cross section. The third column gives the results for the case that a Lorentz function has been used to calculate the intrinsic cross section. The values are averages of the values obtained on fitting spectra measured at 6 different detection angles. The indicated errors are the corresponding standard deviations.

fit parameter	$K_i(E_L)$ given by Eqs. (2.13) and (2.14)	$K_i(E_L)$ given by Lorentz function
E_M (eV)	178.54 ± 0.03	178.53 ± 0.03
γ_M (eV)	0.12 ± 0.01	0.12 ± 0.01
α_M	0.18 ± 0.01	0.18 ± 0.01
E_{3dS} (eV)	2.40 ± 0.00	2.40 ± 0.00
a_{3d3}	0.61 ± 0.00	0.61 ± 0.00
b	0.41 ± 0.07	0.38 ± 0.08
γ_i (eV)	2.99 ± 0.59	4.13 ± 0.65
f_{ELe}	1.04 ± 0.01	1.01 ± 0.01
a	0.73 ± 0.05	0.77 ± 0.05
$E_{Le,SP}$ (eV)	8.93 ± 0.07	9.13 ± 0.12
D_s (nm)	0.68 ± 0.25	0.68 ± 0.25
γ_{GX} (eV)	0.68 ± 0.02	0.68 ± 0.02
f_G	0.98 ± 0.03	0.98 ± 0.03

where f_G is the Gaussian contribution. For both functions $I_G(E)$ and $I_X(E)$ now the same width $\gamma_G=\gamma_X=\gamma_{GX}$ has been used. Both f_G and γ_{GX} have been used as fit parameter. Since the order of convolution of functions is unimportant $I_{GX}(E)$ can replace either $I_X(E)$ in Eq. (2.5) or $I_G(E)$ in Eq. (2.16).

Optimum values for the fit parameters have been found by minimizing the sum of squared intensity differences between calculated and measured Zr 3*d* spectrum using the Nelder-Mead simplex search algorithm implemented in Matlab [40]. Figures 2.1 and 2.2 shows a perfect agreement between the calculated and measured spectrum for the zirconium metal and the zirconium oxide layer, for three different detection angles, 28°, 58° and 78°, respectively. Since the difference between the calculated spectra using Eqs (2.13) and (2.14) or using a Lorentz function to describe the cross section for intrinsic excitation $K_i(E_L)$

Table 2.3. Resulting values of the fit parameters for the calculation of the Zr 3*d* spectra of ZrO_2. The second column gives the results for the case that Eqs. (2.13) and (2.14) have been used to calculate the intrinsic cross section. The third column gives the results for the case that a Lorentz function has been used to calculate the intrinsic cross section. The values are averages of the values obtained on fitting spectra measured at 6 different detection angles. The indicated errors are the corresponding standard deviations.

fit parameter	$K_i(E_L)$ given by Eqs. (2.13) and (2.14)	$K_i(E_L)$ given by Lorentz function
E_M (eV)	178.14 ± 0.04	178.14 ± 0.04
γ_M (eV)	0.33 ± 0.02	0.31 ± 0.03
E_{3dS} (eV)	2.40 ± 0.00	2.40 ± 0.00
a_{3d3}	0.68 ± 0.01	0.68 ± 0.01
b	0.26 ± 0.04	0.27 ± 0.04
γ_i (eV)	2.93 ± 0.64	4.44 ± 0.83
f_{ELe}	1.07 ± 0.00	1.05 ± 0.00
a	0.95 ± 0.01	0.98 ± 0.01
$E_{Le,SP}$ (eV)	5.25 ± 0.73	5.38 ± 0.84
D_s (nm)	0.16 ± 0.07	0.16 ± 0.10
γ_{GX} (eV)	1.56 ± 0.02	1.57 ± 0.02
f_G	0.97 ± 0.05	0.98 ± 0.05

(see Sec. 2.2) is not visible on the scale of Figs. 2.1 and 2.2, only the results for the case of the Lorentz function have been presented. Actually, the case of the Lorentz function gives a slightly better fit than the case of Eqs. (2.13) and (2.14). The resulting values of the fit parameters have been presented in Table 2.2 for Zr and Table 2.3 for ZrO_2. The values given in Tables 2.2 and 2.3 are the averages of the values obtained on fitting spectra measured at 6 different detection angles. The indicated errors are the corresponding standard deviations.

The value obtained for the position E_M of the Zr 3*d* main peak of the pure metal agrees well with literature (178.27 eV is the average value obtained from the NIST database [41] for pure zirconium metal). The values for the core level splitting of the Zr $3d_{5/2}$ and Zr $3d_{3/2}$ peaks E_{3dS} and the intensity ratios of these peaks a_{3d3} are also close to the values, obtained in other studies (2.39 eV for the splitting [14] and 0.64 for the intensity ratio [42]). However the values for the full width at half maximum γ_M and singularity index α_M of the Zr 3*d* core level main peak reported in Refs. [14] and [42] are larger than those found here, probably because of the instrumental resolution and a proper accounting for the instrumental broadening in the present work. The value obtained for the position of the Zr 3*d* main peak of the ZrO_2 layer is too small. This is caused by the low energy electron bombardment, applied for charge compensation, during XPS measurement of the ZrO_2 layer, which results in an "overcompensation". If the O 1*s* peak (shifted to 526.2 eV due to the charge compensation) is used as a reference peak set at 531.03 eV (the average value of the position of the O 1*s* peak of ZrO_2 in the NIST database [41]) then the position of the Zr 3*d* peak becomes 182.96 eV, which agrees well with literature (182.82 eV is the average value obtained from the NIST database [41]). Values for the other parameters of the Zr 3*d* main peak of ZrO_2 have not been found in literature. It is noted that the larger value found for the instrumental broadening (γ_{GX}) in case of ZrO_2 as compared to Zr indicates that, despite the electron bombardment during measurement, there still is some broadening due to charging. Thus also the value found for γ_M of ZrO_2 might be influenced by charging.

The position of the extrinsic cross section is close to that given in Ref. [37] as is indicated by the values of f_{ELe} being close to 1. The positions of the surface plasmon peaks $E_{Le,SP}$ are lower than the theoretical ratio between bulk and surface plasmon energy loss (i.e. $E_{Le,s} = E_{Le,b} / \sqrt{2}$). For ZrO_2 the values are probably not very reliable because of the very small surface contribution to the spectrum (see Fig. 2.2). No values for the other fitting parameters a, b, γ_i and D_s regarding Zr or ZrO_2 have been found in the literature. The value found for the thickness D_s of the surface region of Zr, is practically the same as that found for Mg in Ref. [25], i.e. approximately 2 atomic layers. For ZrO_2 it is less than an atomic layer. It should be noted that in reality there is probably not a sharply defined interface, as has been assumed here, between the regions where surface excitations occur and where bulk excitations occur. An exponential decay of the probability for a surface excitation with distance to the surface might be more realistic. In that case the values found here for the thickness of the surface layer underestimate the depth range where surface excitations occur.

The values found for b indicate that the Zr 3*d* main peak contains only 100 / (1+0.41) = 71% (or 72% when a Lorentz function is used for the cross section for intrinsic energy loss) of the total intrinsic intensity in case of Zr and 100 / (1+0.26) = 79% (also 79% when a Lorentz function is used for the cross section for intrinsic energy loss) in case of ZrO_2. The rest of the intrinsic intensity is contained in the background. These values agree well with the average value of 78% found for several metals in Ref. [43].

The standard deviations of the parameters b, γ_i and D_s (see Table 2.2) are relatively large (>15%). The individual values of these parameters, as well as of the parameter a, show a dependency on detection angle (a and D_s generally decrease and b and γ_i generally increase with increasing detection angle relative to the surface normal). This apparent dependency on detection angle is probably caused by the effect of elastic scattering of electrons, which has been neglected in this paper.

Finally, Tables 2.2 and 2.3 show that both for Zr and ZrO_2 the values obtained for the fitting parameters, taking the standard deviations into account, do not depend much on which function has been used for the intrinsic cross section.

2.5. Conclusions

The Zr 3*d* spectra of Zr and ZrO_2 have quantitatively be described using physically realistic functions to describe the different contributions. As a result the intrinsic and extrinsic as well as surface and bulk contributions to the spectra have been determined. It was found, that a significant part of the intrinsic contribution (about 40% of the main peak intensity for pure zirconium and about 27% of the main peak intensity for pure zirconium oxide) is contained in the part of the spectrum that is usually considered as background.

Appendix A: Analytical solution of Eqs. (2.13) and (2.14) [35]

The integral over k in Eq. (2.13) with Im(1/ε) given by Eq. (2.14) is:

$$K_e(E_L) = \frac{1}{2\pi E a_0} \sum_j \frac{A_j \gamma_j E_L}{\left(E_{Le,j}^2 - E_L^2\right)^2 + \left(\gamma_j E_L\right)^2} \left\{ \ln\left(\frac{k_+^2}{k_-^2}\right) - \frac{T_j(c_j) - T_j(-c_j)}{2\gamma_j E_L c_j} \right\} \tag{2.A1}$$

where:

$$\begin{aligned} T_j(c_j) = {} & \left\{(\gamma_j E_L)\left(E_{Le,j} g_j + c_j\right) - (E_{Le,j} h_j)\left(E_{Le,j}^2 - E_L^2\right)\right\} Q_j \\ & + \left\{\left(E_{Le,j} g_j + c_j\right)\left(E_{Le,j}^2 - E_L^2\right) + (\gamma_j E_L)(E_{Le,j} h_j)\right\} R_j \end{aligned} \tag{2.A2}$$

$$c_j = \left(E_L^4 + (\gamma_j E_L)^2\right)^{1/4} \tag{2.A3}$$

$$g_j = \left\{\frac{1}{2}\left(1 + \frac{E_L^2}{c_j^2}\right)\right\}^{1/2} \tag{2.A4}$$

$$h_j = \left\{\frac{1}{2}\left(1 - \frac{E_L^2}{c_j^2}\right)\right\}^{1/2} \tag{2.A5}$$

$$Q_j = \frac{1}{2} \ln\left(\frac{x_{j+}^2 + (c_j h_j)^2}{x_{j-}^2 + (c_j h_j)^2}\right) \tag{2.A6}$$

$$R_j = \arctan\left(\frac{(-c_j h_j)}{x_{j+}}\right) - \arctan\left(\frac{(-c_j h_j)}{x_{j-}}\right) \tag{2.A7}$$

$$x_{j\pm} = E_{Le,j} + \frac{\hbar^2 k_\pm^2}{2m} - c_j g_j \tag{2.A8}$$

Note that the arctan(r) function in Eq. (2.A7) is applied such that when an absolute jump larger than π occurs (when r changes from $+\infty$ to $-\infty$ and vice versa) the function value is changed to its 2π complement such that a continuous evolution of arctan(r) results.

Chapter 3

The initial, thermal oxidation of zirconium at room temperature

A. Lyapin, L. P. H. Jeurgens, P. C. J. Graat, E. J. Mittemeijer

Abstract

Angle-resolved X-ray Photoelectron Spectroscopy (AR-XPS) and in situ spectroscopic ellipsometry have been used to investigate the initial oxidation of polycrystalline zirconium at room temperature in the partial oxygen pressure range of 1.3×10^{-7} – 1.3×10^{-4} Pa. Detailed quantitative analysis of the measured Zr 3*d* AR-XPS spectra of the oxidized metal allowed separation of the intrinsic and extrinsic metallic and oxidic contributions to the spectra. It was shown that, in addition to the metallic contribution from the substrate and the oxidic contribution from stoichiometric ZrO_2, two additional suboxidic components are contained in the measured Zr 3*d* spectra of the oxidized Zr metal. As evidenced by angle-resolved XPS and in situ ellipsometry, both of these components can be attributed to a gradient of Zr-enrichment in the region of the oxide film adjacent to the metal/oxide interface (with the highest Zr-enrichment at the metal/oxide interface). Investigation of the oxide-film growth kinetics at various pO_2, as determined independently using both techniques, showed the occurrence of an initial regime of very fast, electric-field controlled growth, followed by a much slower oxidation stage. As a result, an, on average, non-stoichiometric oxide film develops. The observed effect of the pO_2 on the low-temperature oxidation of Zr has been discussed in terms of the relationship between the fraction of coverage of the surface with physi- and chemisorbed oxygen and the applied pO_2.

3.1. Introduction

The presence of a thin oxide film on the surface of a pure metal or alloy substrate has a direct bearing to a variety of its chemical and physical properties, such as corrosion resistance, adhesion, thermal stability, friction, and dielectric capacity. In order to control the properties of such thin oxide films grown on bare metal substrates by, e.g., thermal oxidation, comprehensive and fundamental knowledge on the initial stages of the oxidation is required. For example, knowledge on the relationship(s) between growth mechanism(s) and the resulting thickness, composition, morphology and microstructure of the grown oxide film is of great interest for a large number of application areas, such as microelectronics, surface coatings, and catalysis.

This paper addresses the initial stages of dry, thermal oxidation of polycrystalline zirconium at room temperature in the partial oxygen pressure (pO_2) range of 10^{-4} – 10^{-7} Pa. Both zirconium and zirconium oxide are technologically important materials, and in many applications, their surface properties are of particular interest. For example, zirconium is used in the nuclear industry as a structural material for nuclear power reactors and in the chemical industry for corrosion protection (cf. Ref. [6]). Zirconium oxide is, for example, used for its high-temperature resistance in the glass, ceramic, and coating industry and has recently been highlighted as a serious candidate for the replacement of SiO_2 in microelectronic devices, because of its high-dielectric constant (~ 25; cf. Ref. [10]).

The oxidation of zirconium has been investigated in a few studies using different surface analysis techniques (cf. Refs. [13–15]). However, large disagreement exists regarding the origin, number and type of intermediate oxidic components and the oxidation kinetics. For example, the formation of a single suboxide species (ZrO_x) [15], two suboxide species (Zr_2O and Zr_2O_3) [44], or even three suboxide species (Zr_2O, ZrO, and Zr_2O_3) [14, 45] upon the thermal oxidation of Zr has been postulated. Moreover, in most of these studies, no explanation is given for the origin of such suboxide species.

In the current investigation, very thin (< 2 nm) oxide films have been grown on a bare, polycrystalline Zr substrate at room temperature by exposure to pure oxygen gas in the partial oxygen pressure (pO_2) range of 10^{-4} – 10^{-7} Pa. Angle-resolved X-ray Photoelectron Spectroscopy (AR-XPS) has been applied to determine the oxide-film thickness, the constitution, and the overall composition, whereas the oxide-film growth kinetics as a function of pO_2 have been measured applying in situ ellipsometry (Secs. 3.2 and 3.3). The relationship(s) between the growth kinetics, pO_2, constitution and chemical composition of the developing oxide film have been established and discussed (Sec. 3.4).

3.2. Experimental

3.2.1. Sample preparation

A piece of Zr was cut from a zirconium polycrystalline bar (supplied by Alfa Aesar), and then arc-melted in a vacuum furnace. Next, the thus obtained Zr piece was cold-rolled from 10 mm down to a thickness of 0.5 mm, after which disc-shaped specimens (diameter 10 mm and thickness 0.5 mm) were punched out of the resulting foil. Prior to introduction into UHV, the specimen surface was prepared by grinding and polishing, successively. The polishing was performed on soft clothes with a paste of 6 μm, then 3 μm and finally 1 μm diamond grains, and using a mixture of ethanol, soap and distilled water as a lubricant. After the polishing, the specimens were thoroughly cleaned ultrasonically by ethanol, acetone and isopropanol, successively.

In the UHV chamber for the XPS analysis (base pressure $< 5\times10^{-8}$ Pa) directly coupled to the UHV reaction chamber (RC; base pressure $< 2.5\times10^{-8}$ Pa), first the native oxide film was removed by sputter cleaning with 4 kV Ar^+ ions, until no surface contamination of C, O, Ar or some other impurity elements were detected by XPS measurement in the binding energy (BE) range from 0 to 1400 eV (for instrumental details see Sec. 3.2.2). Next, the specimen was stress-relieved and outgassed by a treatment of annealing for 45 minutes at 973 K under UHV in the RC. Finally, the annealed specimen was again sputter-cleaned with 4 kV Ar^+ ions. Zr specimens, as obtained after the series of treatments described above, are further designated as *bare* Zr substrates. Chemical analysis of a bare Zr substrate showed the following impurity concentrations (in ppm wt. %): $O < 2$ and $N < 1$ (as determined by Carrier Gas-Hot Extraction), $C = 40 \pm 4$ and $S < 20$ (as determined by Oxygen Combustion), $Hf < 20$ and $Fe < 50$ (as determined by Inductively Coupled Plasma Optical Emission Spectroscopy), and $H < 62$ (as determined by Elastic Recoil Detection Analysis). Optical light microscopic analysis of a bare Zr substrate showed that the sizes of the grains of the polycrystalline Zr substrate are within the range of 10 to 50 μm.

A ZrO_2 reference sample was produced by sealing a bare Zr substrate (see above) in a quartz tube filled with pure oxygen gas at a pressure of 9.3×10^4 Pa, and subsequently annealing it for 7 h in a conventional tube furnace at 973 K. As shown by X-ray diffraction and light optical microscopy, an approximately 6-μm-thick layer of monoclinic ZrO_2 had formed on the substrate surface. Prior to the XPS analysis of the thus obtained ZrO_2 reference, a short sputter-cleaning step was performed with low energy 1 kV Ar^+ ions.

3.2.2. Thermal oxidation and XPS and ellipsometric analyses

Oxide films were grown in the RC at 304±1 K as a function of total oxygen exposure time (t) by exposing a *bare* Zr substrate (see Sec. 3.2.1) to pure oxygen gas (99.997 vol.%) at partial oxygen pressures (pO_2) of 1.3×10^{-7}, 1.3×10^{-6}, 1.3×10^{-5}, and 1.3×10^{-4} Pa. Total exposure times varied from 120 to 7200 s. The oxygen gas was introduced into the RC by a needle valve and adjusted by hand to the required partial pressure within about 30 s. During oxidation, the pO_2 was recorded as a function of oxidation time with a quadrupole mass spectrometer (Vacscan 100 Dual × 100). For each oxidation experiment, the total oxygen exposure time was taken equal to the value obtained by dividing the integrated area below the recorded curve of pO_2 versus t, by the (averaged) constant value of the pO_2 attained within about 30 s after opening of the needle valve. All oxidation experiments were executed on the same specimen. Before each oxidation experiment, the sample was sputter-cleaned as described in Sec. 3.2.1.

Before and during the oxidation, the changes in the value of the ellipsometric phase and amplitude parameters, Ψ and Δ, were measured *in situ* as a function of oxidation time using a Woollam M 2000 L spectroscopic ellipsometer (mounted directly on the flanges of the RC), equipped with a Xe light source. From the Xe spectrum a wavelength (λ) range of 245 – 850 nm was used with a step size of 0.8 nm. A polarizer span of 180° was applied. The Ψ and Δ values were corrected for the in-plane and out-of-plane window effects. The angle of incidence and reflection of the light were 70° relative to the surface normal. Spectra of both Ψ and Δ as a function of λ were recorded at an interval of 6 s.

XPS analysis of the specimen surface before and after oxidation was performed with a VG Thetaprobe system using monochromatic incident Al Kα radiation ($h\nu$ = 1486.68 eV; spot size = 400 μm). Electrons were detected simultaneously over the angular range (with respect to the surface normal) of 23 to 83° in six ranges of 10°. XPS survey spectra, covering a binding energy (BE) range of 0 eV to 1400 eV, were recorded with a step size of 1.0 eV at a constant pass energy range of 200 eV. The energy scale of the hemispherical analyzer spectrometer was calibrated according to the procedure described in Ref. [46]. Detailed spectra of the Zr 3*d* and O 1*s* photoelectron lines were measured in the BE range from 170 to 230 eV and from 520 to 540 eV, respectively, with a pass energy of 50 eV and a step size of 0.05 eV. The spectra were measured at 64 points homogeneously distributed over an entire analysis area of 3×3 mm^2 and then averaged for each angular range (see above) of photoelectron detection. It is noted that the entire area analysed with AR-XPS and ellipsometry included more than 1000 grains of the weakly-textured polycrystalline Zr sample, thereby averaging out possible grain-orientation effects on the oxidation.

3.3. Data Evaluation

3.3.1. XPS

First, a single Zr 3*d* and O 1*s* XPS spectrum was determined for each measurement of the bare or oxidized Zr substrate (as well as for the ZrO_2 reference; see Sec. 3.2.1) by averaging each corresponding series of spectra recorded over the entire angular detection range from 23 to 83° (for the deviating procedure followed to construct the effective depth plot, see Sec. 3.4.1). Next, to correct for possible variations of the XPS instrument parameters, e.g. flux of photons from the X-ray source and/ or count rate of the electron analyzer, each intensity of the thus obtained Zr 3*d* and O 1*s* spectra of the bare and oxidized metal was divided by the average intensity of a “snapshot” spectrum (i.e., a short measurement) of the corresponding sputtered-clean Zr substrate. Then, all Zr 3*d* and O 1*s* spectra measured from the bare and oxidized metal, were corrected for the electron-kinetic-energy dependent transmission of the hemispherical analyzer of the spectrometer by adopting the corresponding correction factor as provided by the manufacturer (see Sec. 3.2.2). Finally, the lower binding energy (BE) sides of the Zr 3*d* and O 1*s* main peaks were set to zero (background) intensity by subtraction of a constant background, as taken equal to the average minimum intensity at the lower BE side of the main peak concerned.

For the photoemission process from a solid, the excitation energies of the emitted photoelectrons, as well as their respective intrinsic (i.e. core-hole induced) and extrinsic (i.e. photoelectron-induced) energy loss functions, may be different for the surface and bulk regions of the solid (cf. Refs. [47, 48]). However, the excitation energies of the Zr 3*d* photoelectrons emitted from their ground state can be taken the same for the bulk and surface regions of Zr, as well as for the bulk and surface region of ZrO_2 [29, 47]. For the quantitative analysis of the measured XPS spectra, the bare Zr substrate and the ZrO_2 reference are therefore treated as a bulk substrate with a thin surface region of the same material, but with different intrinsic and extrinsic electron-energy loss properties. Then, the corresponding *intrinsic* Zr 3*d* photoelectron spectrum of the bulk (or surface) region of the bare Zr substrate is described by the convolution of a Doniach-Sunjic line shape function, representing the Zr 3*d* doublet for photoemission from its ground state, with the corresponding intrinsic energy loss function for the bulk (or surface) region of the Zr metal. Likewise, the *intrinsic* Zr 3*d* spectrum of the bulk (or surface) region of ZrO_2 is calculated by the convolution of a Lorentzian line shape function, describing the Zr 3*d* doublet of ZrO_2 for photoemission from its ground state, with the corresponding intrinsic energy loss function for the bulk (or surface) region of ZrO_2. Next, the thus obtained, purely intrinsic, spectra are convoluted with: (*i*) a symmetrical, mixed Gaussian-Lorentzian function, accounting for the instrumental and X-ray broadening, and (*ii*) the appropriate extrinsic electron energy loss function, describing the background of inelastically scattered electrons associated with the intrinsic Zr 3*d* main peak concerned. The extrinsic loss functions for the bulk and surface regions of the Zr metal and ZrO_2 are calculated using Werner's formalism [31, 32], while adopting the appropriate cross section for inelastic electron scattering [37]. For further details on the reconstruction of the Zr 3*d* spectra, see Ref. [47].

Then, for the case of the *oxidized* Zr substrate, the intrinsic metallic and oxidic contributions plus their associated inelastic background were resolved from the measured Zr 3*d* spectrum of the oxidized metal, as follows. First, the individual (intrinsic plus extrinsic) metallic and oxidic Zr 3*d* contributions were calculated for the case of a Zr substrate covered with a thin, homogeneous oxide film of uniform thickness *d* (cf. Refs. [48, 49]). To this end, the intrinsic spectra and the extrinsic loss functions as previously determined for the bulk Zr metal[1] and the bulk and surface region of ZrO_2 were employed (see above and Ref. [47]). This calculation was performed repeatedly for variable oxide-film thickness, while minimizing the rest spectrum, as obtained by subtraction of the calculated spectra from the measured spectrum within the BE range from 170 to 185 eV, by Nonlinear Least Squares (NLLS) fitting (cf. Fig. 3.1). During this minimization procedure, the BE positions of the oxidic Zr 3*d* main peaks were allowed to shift relative to that of the metallic main peak. For all oxidations, the Zr 3*d* spectra measured from the oxidized specimen could be accurately fitted with one metallic, one oxidic, and two weaker suboxidic contributions (cf. Fig. 3.1). These two suboxidic components are associated with non-stoichiometric interface-oxide species (see discussion in Sec. 3.4.1), and will therefore be designated as '*lower-BE interface-oxide*' and '*higher-BE interface-oxide*' components, respectively. Except for the full width at half maximum (FWHM) and the BE position, all other parameters required for the description of the intrinsic spectra of the oxidic and suboxidic components were taken equal to those determined previously for the oxidic Zr 3*d* main peak of the monoclinic ZrO_2 reference (see Ref. [47]). The values for the position of each of these (sub)oxidic main peaks, as well as for

---

[1] As soon as the Zr metal becomes covered with an oxide monolayer, the ' free' electrons in the surface region of the Zr metal become localised as a result of the chemical bonding to oxygen. Consequently, the probabilities for intrinsic and extrinsic loss processes in the surface region of the metal become strongly reduced (cf. Refs. [48, 50]). Therefore, for the reconstruction for the Zr 3*d* spectra of the oxidized Zr metal, the spectral contribution of the ' hypothetical' surface layer of the Zr metal was neglected.

the FWHM (taken the same for all (sub)oxidic main peaks), were allowed to vary during fitting.

The intrinsic O 1*s* spectra were obtained from the measured O 1*s* spectra by subtraction of a Shirley type background in the BE range from 528 to 538 eV.

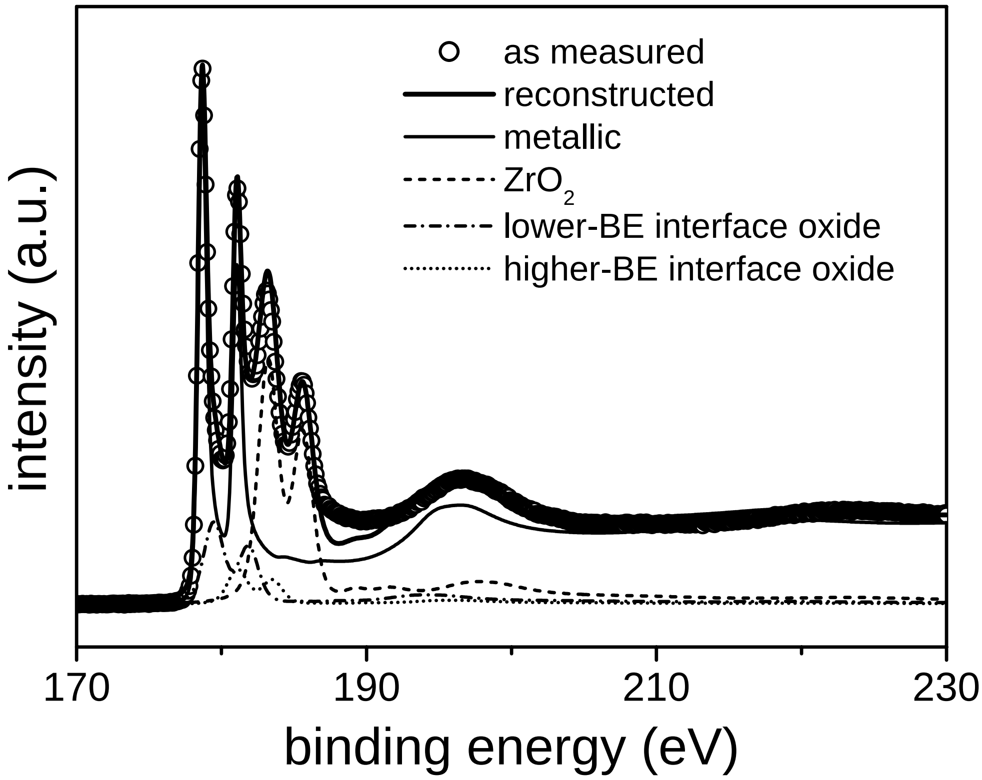

Figure 3.1. Decomposition of a measured Zr 3*d* XPS spectrum, recorded from a Zr substrate after oxidation for 6000 s at a temperature of 304 K and pO_2 of 1.3×10^{-7} Pa into the intrinsic metallic and oxidic contributions plus their associated inelastic backgrounds. Besides the metallic contribution of the Zr substrate, three different oxidic contributions can be recognized: one stoichiometric and two non-stoichiometric oxide contributions designated as 'ZrO_2', 'lower-BE interface oxide', and 'higher-BE interface oxide', respectively. See text for details.

The thus obtained *total* primary zero loss (PZL) intensities of the resolved metallic and oxidic Zr 3*d* and O 1*s* components (i.e. including the intrinsic plasmon loss intensity associated with each main peak; cf. Refs. [47, 48]), as well as the resolved metallic Zr 3*d* PZL intensity of the bare metal (designated as $I_{\mathrm{Zr,\,met}}$, $I_{\mathrm{Zr,\,ox}}$, $I_{\mathrm{O,\,ox}}$, and $I^{\infty}_{\mathrm{Zr,\,met}}$, respectively; where $I_{\mathrm{Zr,\,ox}}$ corresponds to the sum of the PZL intensities of all resolved oxidic Zr 3*d* components; cf. Fig. 3.1), were used to determine the *total thicknesses* of the grown oxide films, as follows. To check the consistency in the evaluation of the thicknesses (and thus also of the resulting composition, see below), the value for the total oxide-film thickness for each oxidation experiment was calculated by six different methods (cf. Refs. [51]): (**1**) from the $I^{\infty}_{\mathrm{Zr,\,met}}/I_{\mathrm{Zr,\,met}}$ intensity ratio; (**2**) from the $I_{\mathrm{Zr,\,ox}}/I_{\mathrm{Zr,\,met}}$ intensity ratio, while taking, as an approximate for the average molar volume density of Zr in the grown oxide films, the corresponding value of $C_{\mathrm{Zr,\,ox}}$ = 46.095 mole/dm^3 for monoclinic ZrO_2 [52]; (**3**) from the $I_{\mathrm{Zr,\,ox}}/I_{\mathrm{Zr,\,met}}$ intensity ratio, while solving the value of $C_{\mathrm{Zr,\,ox}}$ for each grown oxide-film, according to the iterative procedure described in Ref. [51] (taking the values for the ionic radii of Zr and O in the grown oxide film equal to 0.092 and 0.123 nm, respectively [53]); (**4**) from the $I_{\mathrm{O,\,ox}}/I_{\mathrm{Zr,\,met}}$ intensity ratio, while taking as an approximate for the average molar volume density of O in the grown oxide films, the corresponding value of $C_{\mathrm{O,\,ox}}$= 92.191 mole/dm^3 for monoclinic ZrO_2 [52]; (**5**) from the $I_{\mathrm{O,\,ox}}/I_{\mathrm{Zr,\,met}}$ intensity ratio, while solving the value of $C_{\mathrm{O,\,ox}}$ for each grown oxide film by iteration (analogously to calculation 4); (**6**) from the $I_{\mathrm{Zr,\,met}}$, $I_{\mathrm{Zr,\,ox}}$, and $I_{\mathrm{O,\,ox}}$ PZL intensities, while solving the values of both $C_{\mathrm{Zr,\,ox}}$ and $C_{\mathrm{O,\,ox}}$ by iteration (cf. Appendix B in Ref. [51]).

If required in the above calculations, the molar volume density of Zr atoms in the Zr substrate was taken equal to $C_{\mathrm{Zr,\,met}}$ = 71.308 mole/dm^3 (see Ref. [52]). To account for the effect of elastic scattering on the resolved PZL intensities, the values for the inelastic mean free paths (IMFP) in the concerned equations (see Appendix A1 in Ref. [51]) were replaced by the corresponding values of the effective attenuation lengths (EALs) (as calculated according to Eq. (35) in Ref. [54]). All values required for the above calculations are reported in Table 3.1.

The value of and the error in the values determined for the total oxide-film thickness were taken equal to the average of the values obtained from the various thickness calculations and the corresponding standard deviation, respectively.

Each of the above thickness calculations also resulted in a value for the average *composition* (i.e., O/Zr-ratio) of the oxide film, as determined from the resolved $I_{\mathrm{O,\,ox}}/I_{\mathrm{Zr,\,ox}}$ intensity ratio for the given total oxide-film thickness, using as a reference the corresponding intensity ratio of the sputtered-clean, monoclinic ZrO_2 reference (see Sec. 3.2.1) with a known O/Zr-ratio of 2 (see Ref. [51]). The value of and the error in the values determined for the oxide-film composition were then taken equal to the average of these calculated values and their corresponding standard deviation, respectively.

Table 3.1. Physical constants used for the calculation of the thicknesses and compositions of the Zr-oxide films grown at 304 K from measured Zr 3*d* XPS spectra, as described in Sec. 3.3.1.

Constant	Value	Units	Reference
Density of cold-rolled Zr	6.505	g/m^3	[52]
Density of monoclinic ZrO_2	5.68	g/m^3	[52]
Band gap energy for monoclinic ZrO_2	5.42	eV	[38]
Asymmetry parameter β for:			[55]
Zr 3*d* electrons	1.16		
O 1*s* electrons	2		
Kinetic energy for:			[41]
Zr 3*d* electrons emitted from Zr	1308.02	eV	
Zr 3*d* electrons emitted from ZrO_2	1303.43	eV	
O 1*s* electrons emitted from ZrO_2	955.48	eV	
IMFP for:			[39]
Zr 3*d* electrons in Zr	2.55	nm	
Zr 3*d* electrons in ZrO_2	2.39	nm	
O 1*s* electrons in ZrO_2	1.89	nm	
EAL for:			[54]
Zr 3*d* electrons in Zr	2.32	nm	
Zr 3*d* electrons in ZrO_2	2.23	nm	
O 1*s* electrons in ZrO_2	1.71	nm	

3.3.2. Ellipsometry

To determine the growth kinetics and the optical constants[2] from the in situ ellipsometric measurement of the oxidizing Zr substrate, a model has to be constructed, which fits the measured changes in Ψ and Δ as a function of oxidation time over the wavelength range considered. Ψ is the angle whose tangent equals the ratio of the amplitude attenuation (or magnification) upon reflection for the p and s polarizations (i.e., the components of the

---

[2] i.e., the complex index of refraction $N = n - \mathrm{i}k$, where the real part of N is denoted as the index of refraction n and the imaginary part is designated as the extinction coefficient k (cf. Ref. [19]).

electric field vector of the polarized light vibrating in the plane of incidence and perpendicular to it), respectively; Δ is the difference between the phase shifts experienced upon reflection by the p and s polarizations, respectively (for details, cf. Ref. [19]). The fitting of the calculated data to the measured data was performed using the WVASE32 software package (version 3.363) [56].

As evidenced by the angle-resolved XPS analysis of the oxidized Zr substrates (see Sec. 3.4.1), the grown Zr-oxide films exhibit a strong deviation from the stoichiometric composition of ZrO_2 in the region adjacent to the metal/oxide interface. Indeed, the measured ellipsometric data could only be fitted accurately adopting a model that incorporates a Zr substrate covered with a double-layered oxide structure, including a bottom layer of non-stoichiometric Zr oxide and a (surface adjacent) top layer of stoichiometric ZrO_2. For a single-oxide layer model (i.e., ZrO_2 on top of the Zr substrate), the averaged, mean-squared differences between the measured and calculated data points for Ψ and Δ are relatively 42% and 62% higher, as compared to the two-layer model. Moreover, a single-layer model cannot describe the course of the measured change in Ψ with increasing oxidation time.

For the description of the optical constants of the stoichiometric ZrO_2 *top layer* as a function of the wavelength in the above-described two-layer model, the following Cauchy-type of function was used to describe the refractive index n, while setting the extinction coefficient k to zero over the entire concerned wavelength range (i.e., ZrO_2 is transparent over the considered wavelength range),

$$n(\lambda) = a + b/\lambda^2 + c/\lambda^4 \qquad (3.1),$$

where $n(\lambda)$ denotes the refractive index at wavelength λ and a, b and c are constants. The non-stoichiometric Zr-oxide *bottom layer*, on the other hand, was modelled as a layer with optical properties calculated by the effective medium approximation (EMA) using the Maxwell-Garnett formulation [56] and taking stoichiometric ZrO_2 as the matrix. This implies that the shift in the optical constants of this non-stoichiometric oxide layer (with respect to those of ZrO_2), due to its relative Zr-enrichment (see Sec. 3.4.3), is modelled by treating this oxide layer as a random distribution of small (as compared to λ) spherical particles of Zr metal embedded in a dielectric matrix of stoichiometric ZrO_2. Such an inhomogeneous system can be proven to be equivalent (for its optical properties) to a homogeneous one with an *effective* complex refractive index N_e given by (cf. Chapter 4.8 in Ref. [19])

$$\frac{N_{\mathrm{e}}^2 - N_{\mathrm{met}}^2}{N_{\mathrm{e}}^2 + 2N_{\mathrm{met}}^2} = f_{\mathrm{met}} \frac{N_{\mathrm{ox}}^2 - N_{\mathrm{met}}^2}{N_{\mathrm{ox}}^2 + 2N_{\mathrm{met}}^2} \qquad (3.2),$$

where N_{met} and N_{ox} (= n_{ox}; see above) are the (complex) refractive indices of Zr metal (as obtained from the measurement of the bare Zr substrate) and stoichiometric ZrO_2 (as represented by a Cauchy function), respectively, and f_{met} is the volume fraction of Zr metal. Note that this assessment of optical properties does not imply that in reality Zr metallic particles occur in the oxide bottom layer. It is recognized that this EMA bottom layer also effectively describes effects of any roughness present at the metal/oxide interface. It is noted that the adding of an additional layer to the model solely describing surface or interface roughness (cf. Ref. [56]) did not lead to a decrease of the mean-squared error, and was therefore omitted.

The optical constants for Zr metal as a function of λ were straightforwardly determined from the time-averaged values of the Ψ and Δ (cf. Ref. [19]), as recorded in situ from the bare Zr substrate over a time interval of about 120 s prior to the oxidation. Next, the values for the Cauchy constants a, b, and c pertaining to the ZrO_2 top layer, as well as the value for the volume fraction f_{met} of the Zr-oxide EMA bottom layer, were determined as follows. First, for each pO_2, a total of 10 sets of measured spectra of Ψ and Δ versus λ were selected at various oxidation times between 1 and 120 minutes (i.e. a total of 40 sets of spectra for all 4 pO_2's). Next, corresponding sets of spectra were calculated by employing different thickness values for the top (Cauchy) and bottom (EMA) layer for each oxidation time considered, but using the same values for a, b, c, and f_{met} for all oxidation times. This calculation was performed repeatedly for variable layer thicknesses per oxidation time and variable values of a, b, c and f_{met} (but constant for all oxidation times), while minimizing the mean-squared difference between the calculated and experimental sets of spectra using the Levenberg-Marquardt algorithm. This resulted in optimized values for the Cauchy constants of the stoichiometric ZrO_2 top layer of $a = 1.9412$, $b = 0$ [μm^2] and $c = 6.146\times10^{-3}$ [μm^4] (see Eq. (3.1) with λ in micrometer), and an optimized fraction f_{met} for the EMA bottom layer of 50.1% (as well as in optimized values for the thicknesses of the top and bottom oxide layers for each oxidation time considered). The thus obtained value for the refraction index of ZrO_2 (as calculated using Eq. (3.1), adopting the optimized values of a, b, and c) decreases with increasing wavelength λ from $n = 2.35$ at $\lambda = 350$ nm to $n = 1.98$ at $\lambda = 650$ nm. These values can be compared with the corresponding literature values reported for (undoped) monoclinic ZrO_2 [57] and amorphous ZrO_2 [58] of $n = 2.17$ at $\lambda = 632.8$ nm and $n = 1.98$ at $\lambda = 600$ nm, respectively. The value for $n = 1.99$ at $\lambda = 600$ nm, is almost identical to the corresponding value of $n = 1.98$, as determined for amorphous ZrO_2 in Ref. [58], suggesting that the low temperature Zr-oxide films grown in the present study are amorphous.

Finally, the total oxide-film growth curves (i.e., the sums of the top ("Cauchy") and bottom ("EMA") layer thickness) were determined for each pO_2 by fitting the calculated to the experimental spectra of Δ and Ψ within the wavelength range of 350 – 650 nm, while using the previously obtained optical constants for Zr and ZrO_2 and the optimized value of f_{met}, and adopting only the thickness of the Cauchy and the EMA layer as fit parameters.

3.4. Results and discussion

3.4.1. Oxide-film constitution

The Zr 3*d* photoelectron spectra measured from the oxidized Zr metal, could be accurately fitted with one metallic, one oxidic, and two weaker suboxidic components (designated as ZrO_2, lower-BE and higher-BE interface-oxide components, respectively; see Fig. 3.1 and Sec. 3.3.1). It is noted that, for all different oxidation experiments performed, a small part of the measured Zr 3*d* spectra of the oxidized metal within the BE range of about 187 – 192 eV (i.e. at the higher-BE side of the ZrO_2 oxidic main peak) is systematically unaccounted for in the corresponding reconstructed Zr 3*d* spectra. This systematic inconsistency at the higher BE side of the 3*d* oxidic main peak has also been reported in previous XPS investigations of oxidized substrates of Zr (cf. Ref. [15]) and other transition metal compounds (cf. Ref. [59]), and is generally attributed to the presence of an intrinsic 'shake-up' satellite peak in the 3*d* spectrum of the transition-metal compound.[3] Since NLLS fitting of the rest spectra (see Sec. 3.3.1) has been performed within the BE range from 170 to 185 eV (i.e. excluding the BE range of the intrinsic satellite peak), this inconsistency in the reconstructed spectra has no effect on the fit results.

The two resolved interface-oxide components, as well as the ZrO_2 component, are somewhat broader than the oxidic main peak in the monoclinic ZrO_2 reference spectrum (FWHM = 1.9 ± 0.1 eV versus 1.54 ± 0.03 eV, respectively; see also Ref. [47]). This might be attributed to a lower degree of ordering (leading to a larger spread of metal-oxygen bond energies; cf. Ref. [60]) in the overall non-stoichiometric (see Sec. 3.4.3), amorphous

---

[3] these intrinsic 3*d* 'shake-up' satellites originate from the screening of the core hole created in the 3*d* photoemission process of the transition metal cation (here: Zr 3*d*) by a polarization of the surrounding ligands (here: O 1*s*) (cf. Ref. [59]).

(see Sec. 3.3.2) oxide films grown at low temperatures in the present study. The average BE values of 179.43 ± 0.05 and 180.99 ± 0.05 eV, as determined for the positions of the Zr 3*d* main peak of the lower-BE and higher-BE interface-oxide components, are in between the corresponding BE values of 178.66 ± 0.05 and 183.25 ± 0.05 eV, as determined for the metallic and ZrO_2 main peaks, respectively (cf. Fig. 3.1). The intermediate BE positions for the two interface-oxide species can be interpreted as that the Zr ions in the region of the oxide film adjacent to the oxide/metal interface have an, on average, lower valence state (as compared to the valence state of Zr^{IV} for stoichiometric ZrO_2) (with the Zr ions corresponding to the lower-BE interface-oxide species having the, on average, lowest valence state) (cf. Ref. [51]). This relatively lower valence state of the Zr ions in the oxide film adjacent to the oxide/metal interface is due to the relative Zr-enrichment in this region (as evidenced from in situ ellipsometry; see Secs. 3.3.2 and 3.4.2). Consequently, the grown oxide films have an overall, non-stoichiometric composition with an average O/Zr-ratio < 2 as determined using XPS (see Sec. 3.4.3).

To validate that the designated lower-BE and higher-BE interface-oxide species are indeed located in the oxide film adjacent to the metal/oxide interface, effective depth plots have been constructed from the corresponding Zr 3*d* PZL intensities, as resolved from the AR-XPS spectra of the oxidized Zr metal (see Fig. 3.2). This plot provides a direct indication of the (average) effective depth of a given oxidic (or metallic) species below the sample surface and is constructed as follows. Assuming that the signal from a given oxidic species arises from a layer buried at an effective depth <*z*> below the sample surface, the corresponding total oxidic PZL intensity I_{ox}, as observed in a measured XPS spectrum of the oxidized metal, is given by

$$I_{\mathrm{ox}} = I_{\mathrm{ox}}^{\infty} \exp\left(-\frac{<z>}{\lambda_{\mathrm{ox}} \cos\Theta} \right) \tag{3.3a}$$,

where Θ is the detection angle (with respect to the sample surface normal), λ_{ox} denotes the EAL of the concerned photoelectrons travelling from depth <*z*> towards the sample surface, and I_{ox}^{∞} is the total oxidic PZL intensity recorded from a relatively thick (i.e. as compared to λ_{ox}) layer of the corresponding bulk oxide. If the intensity I_{ox} is detected at two different angles Θ_1 and Θ_2, then the logarithm of the corresponding intensity ratio $I_{\mathrm{ox},\Theta_1}/I_{\mathrm{ox},\Theta_2}$ equals

$$\ln\left(I_{\mathrm{ox},\Theta_1}/I_{\mathrm{ox},\Theta_2}\right) = \; <z> \left[1/\lambda_{\mathrm{ox}}\cos\Theta_2 - 1/\lambda_{\mathrm{ox}}\cos\Theta_1\right] \tag{3.3b}$$

Since the term [$1/(\lambda_{ox} \cdot \cos \Theta_2) - 1/(\lambda_{ox} \cdot \cos \Theta_1)$] in Eq. (3.3b) is a constant (for a given set of Θ_1 and Θ_2), the logarithm of the intensity ratio is a direct measure of the relative value of $<z>$.

The effective depth plot constructed from the PZL intensities of the resolved metallic and oxidic Zr 3*d* main peaks, pertaining to the oxidation of the bare Zr substrate for 7200 s at 304 K for various pO_2, is presented in Fig. 3.2. For the construction of this plot, surface and bulk sensitive detection angular ranges of Θ_1 = 53 – 63° and Θ_2 = 23 – 33°, respectively, have been used. Photoelectron detection angles higher than 65° (i.e. even more surface sensitive) have not been considered, because the resolved photoelectron intensities become strongly affected by elastic scattering and surface roughness effects.

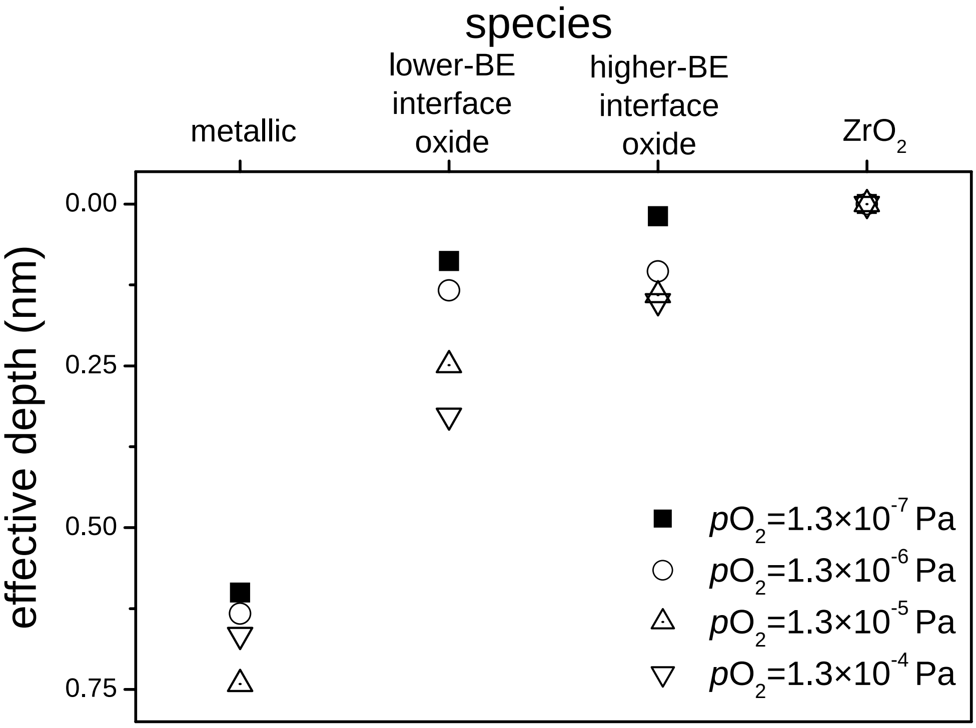

Figure 3.2. Effective depth plot for the Zr 3*d* PZL intensities of the resolved metallic and oxidic (i.e. the ZrO_2 and both interface-oxide) components (see Fig. 3.1) for selected surface and bulk sensitive detection angular ranges of Θ_1 = 53 – 63° and Θ_2 = 23 – 33°, respectively. The data pertain to the oxidation of the bare Zr substrate for 7200 s at 304 K within the pO_2 range of 1.3×10^{-7} – 1.3×10^{-4} Pa. The points indicate the effective depth of the species. See text for details.

Evidently, the metallic Zr species, corresponding to the Zr substrate, is located at the largest depth. The stoichiometric ZrO_2 species is indeed located at the outer oxide surface, whereas both interface-oxide components are positioned at depths in between those of the Zr substrate and the outer oxide surface region of stoichiometric ZrO_2 (i.e. in the region of the oxide film adjacent to the metal/oxide interface): the interface-oxide species with the lower BE value is located closer to the Zr substrate than the higher-BE interface-oxide species[4].

3.4.2. Oxide-film growth kinetics

The average, total oxide-film thickness, as determined by XPS and in situ ellipsometry (cf. Secs. 3.3.1 and 3.3.2), is shown as a function of the oxidation time in Fig. 3.3, for the oxidation of the bare polycrystalline Zr substrate at a temperature of 304 K and at partial oxygen pressures of 1.3×10^{-7}, 1.3×10^{-6} and 1.3×10^{-5} Pa. The values for the total oxide-film thickness, as determined from the measured Zr 3*d* XPS spectra of the oxidized Zr substrate (see Sec. 3.3.1), are in good agreement with the corresponding total thickness values (i.e. sum of the thicknesses of the non-stoichiometric Zr-oxide bottom and ZrO_2 top layer; see Sec. 3.3.2), as determined *independently* from in situ ellipsometry.

For all the pO_2's studied, the oxidation is characterized by an initial regime of very fast oxide-film growth, which is succeeded by a second, very slow oxidation stage in which the oxide-film growth rate slowly, but continuously, decreases and becomes very small. This growth behaviour is typical for the oxidation of metals at low temperatures, where the diffusion of the reactants (i.e. Zr and/or O) into and through the developing oxide film under influence of the (electro)chemical potential becomes negligibly small and the rate of electron transport by thermal emission is effectively zero (cf. Refs. [3, 23, 24]). The extremely high, initial oxidation rates are induced by the presence of an electrostatic potential across the developing oxide film, which lowers the energy barriers for the interstitial, outward migration of Zr cations from the parent metal substrate into and through the developing oxide film towards the reacting oxide/gas interface. The so-called Mott potential V_M is the result of the equilibrium set up between the electronic states at the Fermi level in the metal and the acceptor levels provided by oxygen molecules, atoms and/or ions adsorbed onto the oxide

---

[4] In a preliminary investigation on the oxidation of Zr at 304 K [36], NLLS fitting of the rest spectra was performed over the entire BE of the measured Zr 3*d* spectra. (i.e. including the BE range of the intrinsic Zr 3*d* 'shake-up' satellite peak). Consequently, the systematic underestimation of the reconstructed spectra in the BE range of 187 – 192 eV (see Sec. 3.4.1) was more or less compensated for in the fitting procedure by a broadening of the oxidic Zr 3*d* main peaks. Although, this deviating fit procedure had no effect on the outcome of the XPS data evaluation in terms of the total oxide-film thickness and composition values, it did led to the erroneous result that the lower-BE interface-oxide species on the basis of the reconstructed effective depth plots would occur at the surface rather than at the metal/oxide interface.

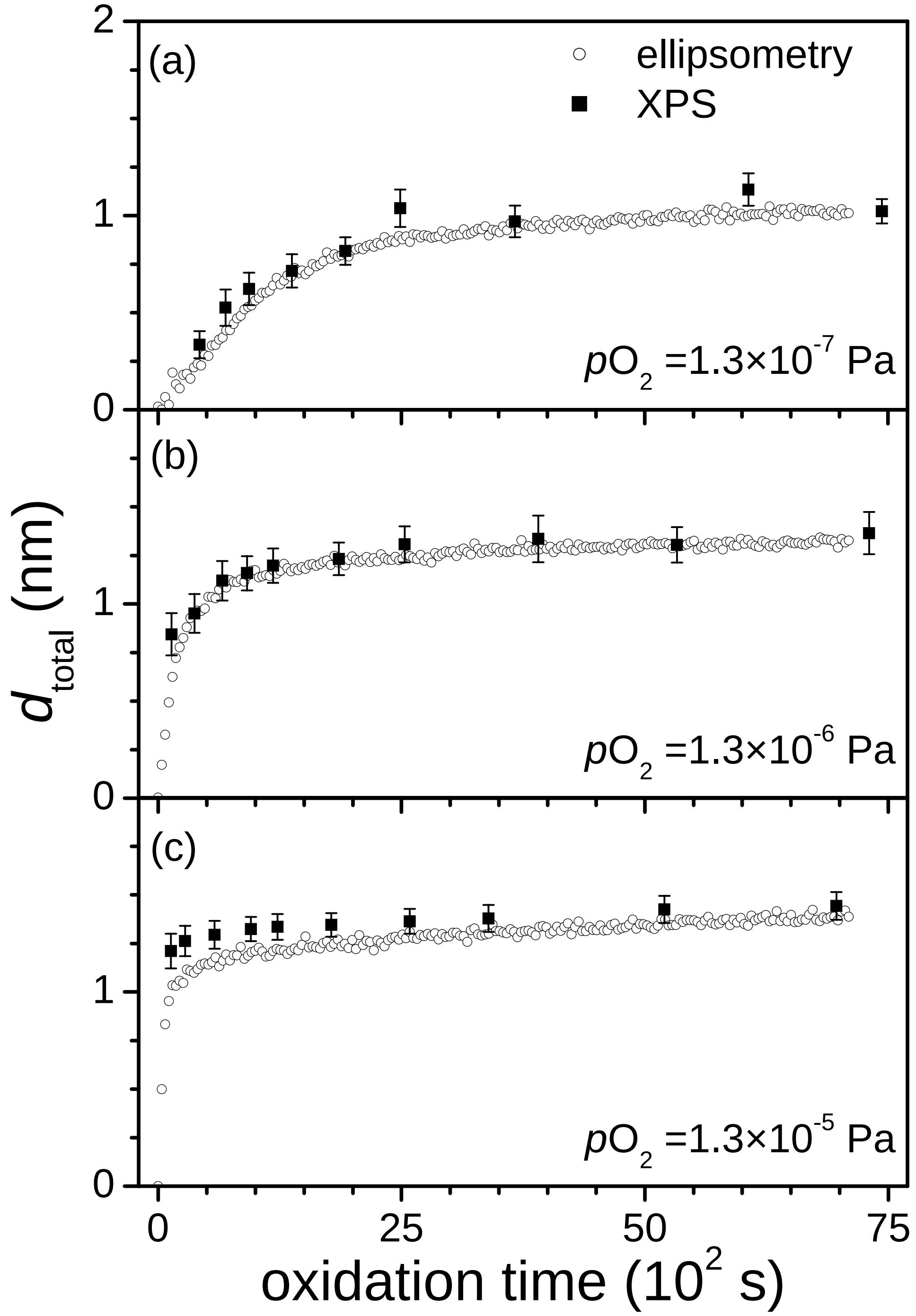

Figure 3.3. Total oxide-film thickness (d_{total}) as a function of oxidation time, for the oxidation of the bare Zr substrate at 304 K and a pO_2 of **(a)** 1.3×10^{-7} Pa, **(b)** 1.3×10^{-6} Pa and **(c)** 1.3×10^{-5} Pa. The total oxide-film thickness values were determined *independently* from (*i*) the measured Zr 3*d* photoelectron spectra recorded from the bare and oxidized Zr substrate using XPS, and (*ii*) from the measured spectra of the phase and amplitude parameters, Δ and Ψ, over the wavelength range of 350 – 650 nm as recorded with in situ ellipsometry.

surface (lying at an energy eV_M below the Fermi level of the metal). The Mott potential is sustained by the difference between the relatively fast, forward and reverse flux of electrons tunnelling through the developing oxide film. The electron-tunnelling current decreases exponentially with increasing oxide-film thickness. Consequently, at a certain critical thickness (usually around 1 nm for most metal-oxide systems; cf. Refs. [23, 24]) the Mott potential breaks down, and then the constraint of coupled currents of electrons and cations (i.e. overall charge neutrality) implies that, at low temperatures, a significant drop in the oxide-film growth rate occurs (cf. Fig. 3.3).

As described in Sec. 3.3.2, the total oxide-film thickness values as determined from in situ ellipsometry, correspond to the sum of the individual thickness values determined for the non-stoichiometric Zr-oxide bottom layer (attributed to both interface-oxide species) and the stoichiometric ZrO_2 top layer (attributed to the ZrO_2 species). The total oxide-film thickness, as well the corresponding individual thicknesses of the interface-oxide and ZrO_2 sublayers, have been plotted as a function of the oxidation time for the various partial oxygen pressures in Figs. 3.4a-c.

A distinct difference in the oxide-film growth kinetics is observed for the ZrO_2 species and the non-stoichiometric interface-oxide species. The thicknesses of the stoichiometric ZrO_2 and interface-oxide sublayers both show a rapid increase during the initial, fast oxidation regime. However, the thickness for the interface-oxide sublayer attains a constant thickness of around 0.75 nm, independent of the value of pO_2, at the onset of the second, slow oxidation stage, whereas the thickness of the ZrO_2 sublayer still slightly, but continuously, increases during the slow oxidation stage. Moreover, for the lowest pO_2 of 1.3×10^{-7} Pa, a significant delay in the growth of stoichiometric ZrO_2 occurs, indicating that the very first stage of oxidation involves the nucleation and growth of non-stoichiometric Zr-oxide.

The individual thicknesses for the interface-oxide and ZrO_2 sublayers as obtained from the ellipsometric analysis can be confirmed by an independent (rough) estimation of these thicknesses from the metallic and all three oxidic Zr 3*d* PZL intensities, as resolved from the AR-XPS spectra of the oxidized Zr metal (see Sec. 3.3.1). Adopting the appropriate equations in Appendix A1 of Ref. [51] for (*i*) the sum of the oxidic PZL intensities of the lower-BE and higher-BE interface-oxides, (*ii*) the PZL intensity of the oxidic ZrO_2 species, and (*iii*) the metallic Zr 3*d* PZL intensity, the aforementioned thicknesses can be solved

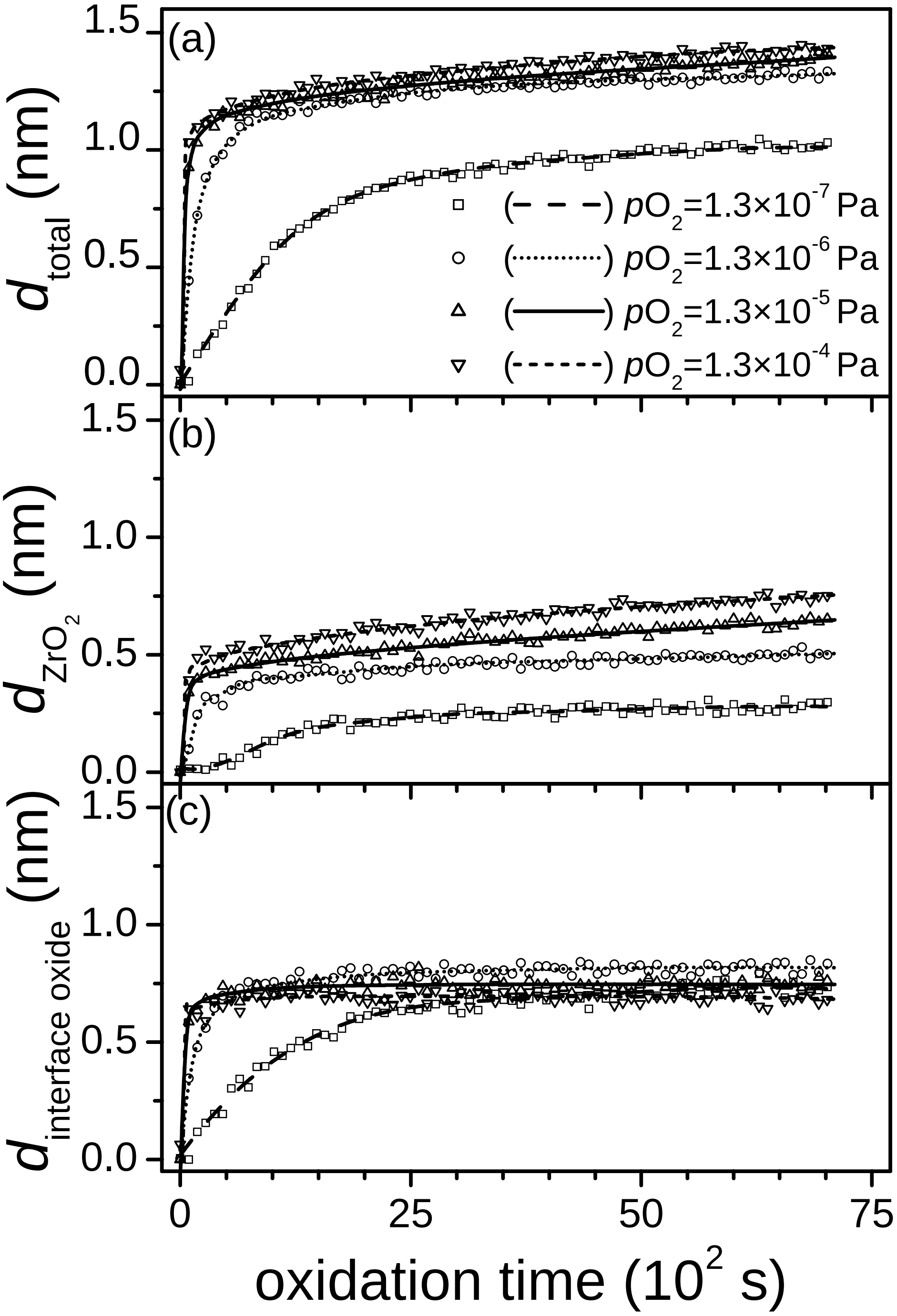

Figure 3.4. **(a)** The total oxide-film thickness (d_{total}), as well as the corresponding individual thicknesses of the **(b)** ZrO_2 top (d_{ZrO_2}) and **(c)** the relatively Zr-enriched bottom ($d_{interface\ oxide}$) oxide sublayers, as a function of oxidation time, for the oxidation of the bare Zr substrate at 304 K and a pO_2 of 1.3×10^{-7}, 1.3×10^{-6}, 1.3×10^{-5} and 1.3×10^{-4} Pa. The oxide-film thickness values were determined from the measured spectra of the phase and amplitude parameters, Δ and Ψ, over the wavelength range of 350 – 650 nm as recorded with in situ ellipsometry. The ZrO_2 top sublayer and the relatively Zr-enriched bottom sublayer correspond with the stoichiometric ZrO_2 and sum of the lower-BE and higher-BE interface-oxide species as identified with AR-XPS, respectively (cf. Figs. 3.1 and 3.2). The lines for each pO_2 represent spline fits through the data points.

by iteration. For the second, slow oxidation stage, this resulted in an average value of 0.6 ± 0.1 nm for the sum of individual thicknesses of the lower-BE and higher-BE interface-oxide species; the corresponding value for the thickness of the stoichiometric ZrO_2 oxide sublayer increases from 0.4 nm at $pO_2 = 1.3\times10^{-7}$ to 0.6 nm at $pO_2 = 1.3\times10^{-4}$ Pa, respectively. These independently obtained estimates are consistent with the corresponding thickness values as obtained from the ellipsometric analysis (see Figs. 3.4b and 3.4c), confirming the supposition made that the interface-oxide sublayer as exhibited by the ellipsometric analysis corresponds to the sum of the lower-BE and higher-BE interface-oxide species as identified by AR-XPS.

As clearly reflected in Fig. 3.4a, the length of the initial, very fast growth regime decreases, and the value of the total oxide-film thickness attained during the slow oxidation regime (after 7200 s) increases with increasing pO_2. For the oxidations at a pO_2 of 1.3×10^{-7}, 1.3×10^{-6}, 1.3×10^{-5} and 1.3×10^{-4} Pa, on average, a total oxide-film thickness of about 1.0 ± 0.2 nm is reached at the onset of the second, slow oxidation stage that begins after approximately 2500, 350, 85 and 85 s, respectively. Oxide-film thicknesses of 1.0, 1.3, 1.4 and 1.5 nm are observed during the second, slow oxidation stage after 7200 s of oxidation, respectively. It follows that, for $pO_2 < 1.3\times10^{-6}$, a change of the pO_2 has a significant effect on the growth kinetics, whereas for $pO_2 > 1.3\times10^{-5}$ Pa the effect of a change in pO_2 on the growth kinetics is rather small.

To understand the observed effect of the pO_2 on the low-temperature oxidation of Zr, the relationship between the fraction of coverage of the (initially) metal and/or oxide surface with physi- and chemisorbed oxygen, θ_{O_2}, the applied pO_2 and the Mott potential has to be considered[5]. As mentioned above, for the initial, electric-field controlled oxide-film growth regime, the growth rate and the thickness reached at the end of the growth stage are controlled by the magnitude of the established Mott-potential. The magnitude of this potential is determined by the amount and type (i.e. O^-, O^{2-}, O_2^-) of charged oxygen particles chemisorbed on the oxide surface, which in turn are dependent on the total number of electron acceptor levels provided by the neutral oxygen molecules/atoms attached (physisorbed) to the oxide surface. It is noted that the formation of charged oxygen chemisorbed particles can occur with or without dissociation of the oxygen molecules, i.e.

---

[5] It is assumed that the initially fast oxide-film growth rate is realised by the electric-field controlled migration of cation interstitials into and through the developing oxide film. In this case, the effect of the pO_2 on the oxide-film growth rate through the pressure dependence of the O^{z-} defect concentrations at the oxide surface can be neglected (cf. Ref. [3]).

$$\begin{aligned} &O_{2\,(\mathrm{phys})} \underset{\leftarrow}{\overset{\rightarrow}{}} 2O_{(\mathrm{phys})} \\ &O_{(\mathrm{phys})} + e \underset{\leftarrow}{\overset{\rightarrow}{}} O^{-} \end{aligned} \qquad (3.4),$$

or

$$O_{2\,(\mathrm{phys})} + z\mathrm{e} \underset{\leftarrow}{\overset{\rightarrow}{}} O_2^{z-}, \text{ where } z = 1 \text{ or } 2 \qquad (3.5),$$

respectively. In both cases the neutral oxygen attached to the surface (physisorbed) provides acceptor sites for the electron current, which leads to charged, chemisorbed oxygen species on the oxide surface. For relatively low pO_2 and low temperatures, the coverage of the surface with physisorbed oxygen (i.e. the number of acceptor levels) is directly proportional to the pO_2. Consequently, the amount of chemisorbed oxygen species, and thus the magnitude of the Mott potential, increases with increasing pO_2; as a result a higher thickness is attained at the end of the initial growth regime (see Figs. 3.3 and 3.4). Further, the time to saturate the oxide surface with physi- and chemisorbed oxygen will decrease with increasing pO_2 and, consequently, the end of the initial growth regime is reached at a time that decreases with increasing pO_2 (cf. Fig. 3.4). Ultimately, with increasing pO_2, at low temperatures, the growth kinetics for the initial, electric-field-controlled growth stage will become independent of the pO_2. Reversibly, at very low pO_2 and at high temperatures, the coverage of the surface with physisorbed and chemisorbed oxygen will be extremely small, because the desorption rate of physisorbed oxygen will be relatively high, and then the oxide-film growth rate may be directly determined by the rate of oxygen impingement (constant at constant pO_2), resulting in a constant oxide-film growth rate.

3.4.3. Oxide-film composition

The average composition of the grown oxide films, expressed as the O/Zr-ratio, has been plotted as a function of the oxidation time for the various pO_2 in Fig. 3.5. For all pO_2‘s and at all oxidation times studied, the grown oxide-film has an overall non-stoichiometric composition. The average O/Zr-ratio of the initial oxide film after 5 min of oxidation is about 1.0, 1.4 and 1.6. The O/Zr ratio increases during the fast oxidation stage, attaining a more or less constant value of about 1.5, 1.6 and 1.7 at the onset of the second, slow oxidation stage at a pO_2 of 1.3×10^{-7}, 1.3×10^{-6} and 1.3×10^{-5} Pa, respectively. Thus, for all pO_2‘s and at all oxidation times studied, the grown oxide film has an overall O/Zr-ratio lower than the stoichiometric value of 2 for ZrO_2.

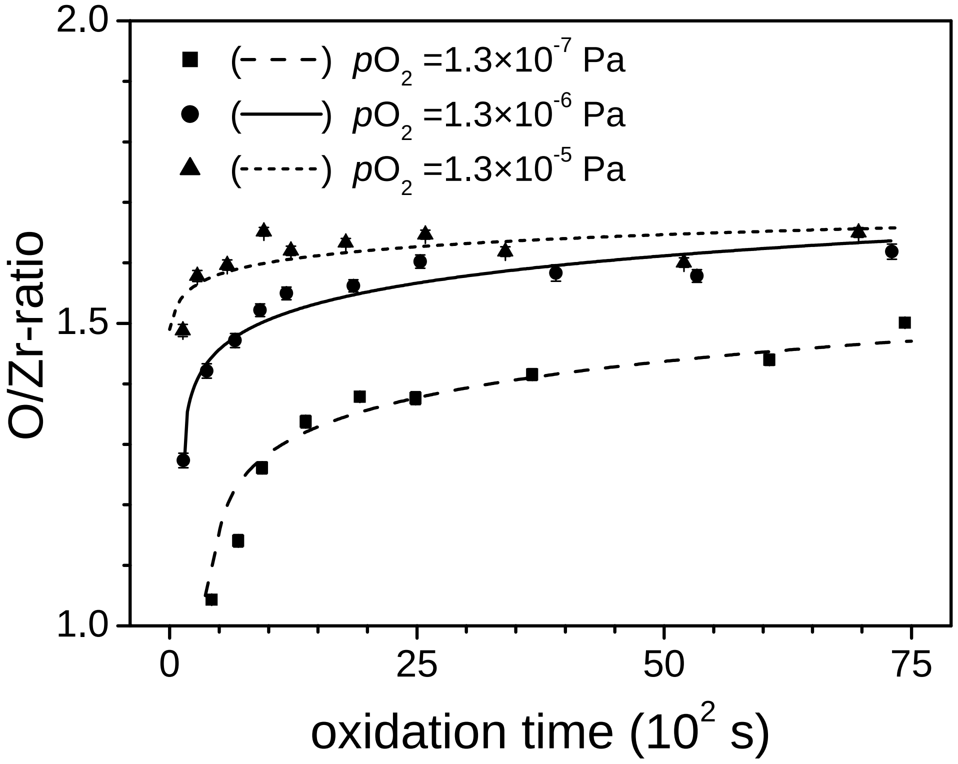

Figure 3.5. The overall composition, expressed as the average O/Zr-ratio, of the grown oxide film as a function of oxidation time, for the oxidation of the bare Zr substrate at 304 K and a pO_2 of 1.3×10^{-7}, 1.3×10^{-6} and 1.3×10^{-5} Pa. The values for the O/Zr-ratio were determined from the total oxidic Zr 3*d* and O 1*s* PZL intensities as resolved from the measured Zr 3*d* and O 1*s* photoelectron spectra recorded from the oxidized Zr substrate using XPS (see Sec. 3.3.1).

The average O/Zr-ratio, as well as the corresponding average O and Zr molar densities, of the grown oxide-films have been plotted as a function of the total oxide-film thickness for the various pO_2‘s in Figs. 3.6a-c, respectively. As evidenced from Figs. 3.6b and 3.6c, the initial increase of the O/Zr-ratio with oxidation time/thickness is due to an increase of the O molar density in combination with a decrease of the Zr molar density of the developing oxide film. The molar density of O in the initially grown oxide film decreases with decreasing pO_2, whereas the corresponding Zr molar density increases with decreasing pO_2. The average values of the molar densities of O and Zr attained during the second, slow oxidation stage are still slightly lower for O and higher for Zr than the corresponding values for stoichiometric ZrO_2 (as indicated by the dotted and dashed lines in Figs. 3.6b and 3.6c, respectively). It can be concluded that the grown oxide films are, on average, enriched in Zr and depleted in O, i.e. the O/Zr ratio < 2.

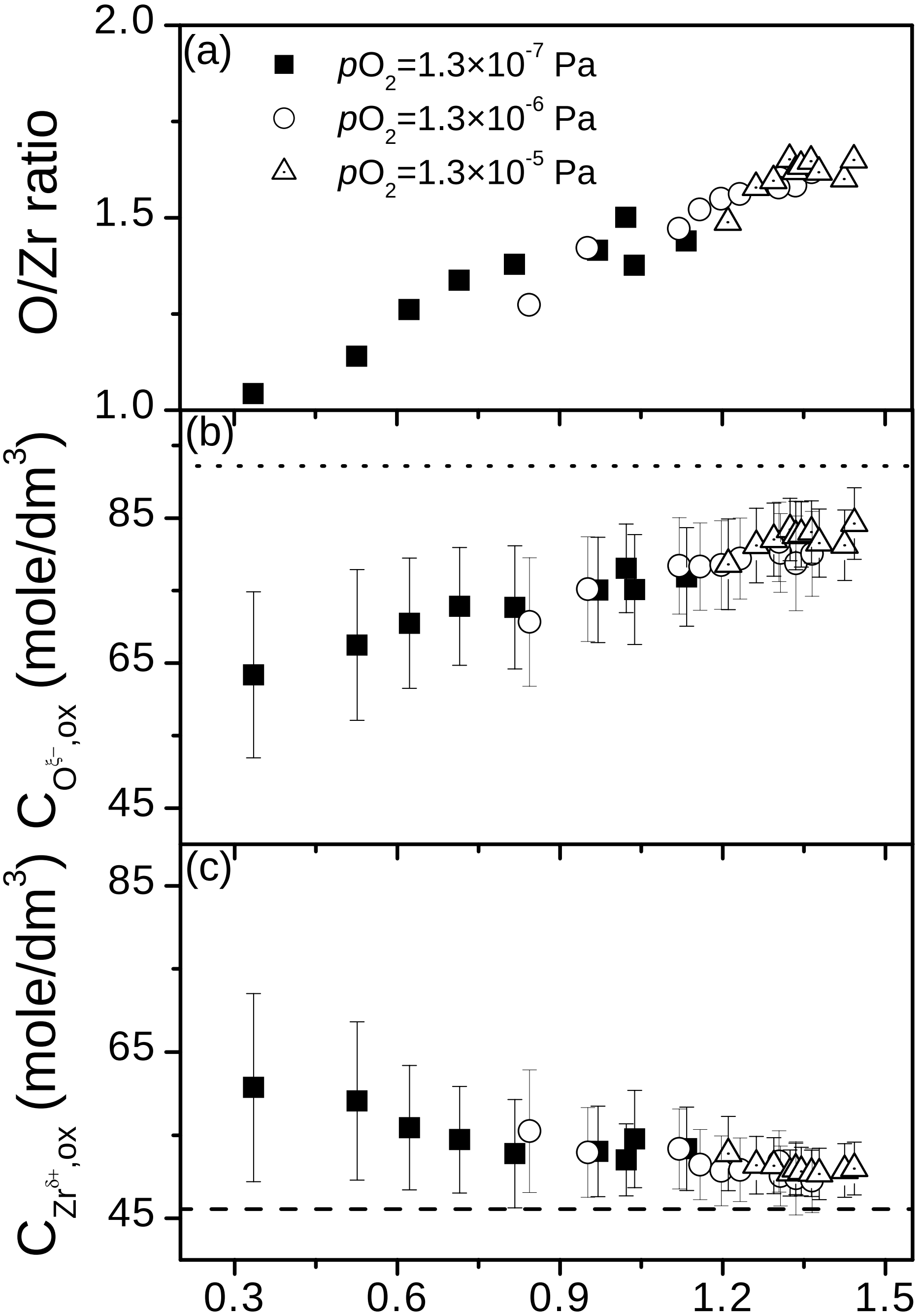

Figure 3.6. (a) The overall composition, expressed as the average O/Zr-ratio, of the grown oxide films as a function of the total oxide-film thickness (d_{total}), for the oxidation of the bare Zr substrate at 304 K and a pO_2 of 1.3×10^{-7}, 1.3×10^{-6} and 1.3×10^{-5} Pa. The corresponding molar densities of the oxygen anions ($C_{O^{\xi-}}$) and of the zirconium cations ($C_{Zr^{\delta+}}$) in the grown oxide films as a function of the total oxide-film thickness are shown in **(b)** and **(c)**, respectively. The molar densities of Zr and O in stoichiometric, monoclinic ZrO_2 of 46.10 and 92.19 mole/dm^3 have been indicated by the dotted line and the dashed line, respectively. See also caption of Fig. 3.5.

Hence, in combination with the evidence obtained from the AR-XPS (cf. Fig. 3.2) and in situ ellipsometric (cf. Fig. 3.4) analyses of the grown oxide films, the overall low O/Zr-ratio of the grown oxide films can be attributed to a relative Zr-enrichment of the oxide films in the region adjacent to the metal/oxide interface, with the degree of Zr-enrichment increasing from the metal/oxide interface towards the oxide surface. These deviations in the overall composition from stoichiometric ZrO_2 correspond with the presence of the associated lower-BE and higher-BE interface-oxide components in the measured Zr 3*d* XPS spectra of the oxidized Zr metal (see Fig. 3.1)

A relative enrichment of cations of the oxide film in the region adjacent to the oxide/metal interface has also been observed for other metal substrate/oxide-film systems (cf. Refs. [51, 61]), and has been conceived as a consequence of the contact potential established at the metal/oxide interface to equilibrate the intrinsic Fermi level of the oxide film with that of the metal substrate (cf. Refs. [62, 63]).

3.5. Conclusions.

Detailed quantitative analysis of the Zr 3*d* XPS spectra recorded from bare, polycrystalline zirconium substrates after oxidations at 304 K in the pO_2 range of 1.3×10^{-7} – 1.3×10^{-4} Pa, showed that *three* oxide species occur in the oxide film.

Angle-resolved XPS and in situ ellipsometric analyses revealed that the oxide film is constituted of stoichiometric ZrO_2 (*ZrO_2 component*) in combination with a Zr-enrichment and oxygen deficiency in oxide-film region adjacent to the metal/oxide interface. The degree of Zr-enrichment (and the oxygen deficiency) decreases from the metal/oxide interface towards the oxide surface (*lower-BE interface-oxide component* → *higher-BE interface-oxide component*). Consequently, the Zr-oxide film has an overall non-stoichiometric composition with an average O/Zr-ratio smaller than 2.

The oxide-film growth kinetics for the oxidation of a bare Zr substrate at 304 K in the pO_2 range of 1.3×10^{-7} – 1.3×10^{-4} Pa, exhibit an initial regime of very fast, electric-field controlled, oxide-film growth, which is succeeded by a second, very slow oxidation stage.

The individual thicknesses determined for both the stoichiometric ZrO_2 sublayer and the Zr-enriched interface-oxide sublayer show a rapid increase during the initial, fast oxidation regime. At the onset of the second slow oxidation stage, the thickness of the interface-oxide becomes constant, whereas that of the stoichiometric ZrO_2 layer still slightly, but continuously, increases. For the lowest pO_2 of 1.3×10^{-7} Pa a significant delay in the development and growth of ZrO_2 occurs, indicating that the very first stage of oxidation involves the development and growth of a Zr-oxide film, enriched in Zr and depleted in O.

The length of the initial oxidation stage, as well as the thickness reached at the onset of the second, slow oxidation regime, increase with increasing pO_2. This is ascribed to an increase of the Mott potential with increasing pO_2, due to the with-increasing-pO_2-associated increase in the density of electron-acceptor sites provided by oxygen molecules/atoms adsorbed onto the oxide surface.

Chapter 4

Effect of temperature on the initial, thermal oxidation of zirconium

A. Lyapin, L.P.H. Jeurgens, E.J. Mittemeijer

Abstract

A novel, methodological approach by combined in situ ellipsometry and angle-resolved X-ray photoelectron spectroscopy (AR-XPS) has been applied to investigate the initial oxidation of zirconium within the temperature range of 373 – 773 K. The effective-depth distributions and individual sublayer thicknesses of the non-stoichiometric and stoichiometric oxide species within the developing oxide film, as established with AR-XPS, are in good agreement with the corresponding results as determined independently with ellipsometry. Oxidation starts with the very fast, electric-field controlled growth of non-stoichiometric Zr-oxide up to a certain limiting thickness that increases with increasing temperature up to about 423 K. Subsequent, continued (for 423 K $< T <$ 523 K) growth is realised by the linear overgrowth of stoichiometric ZrO_2 under influence of the kinetic potential. For $T >$ 573 K, oxide-film growth becomes predominated by the extensive dissolution of oxygen into the substrate that is accompanied by partial decomposition of the growing oxide film.

4.1. Introduction

The initial stages of oxidation of bare metal surface involve a number of different physical and chemical processes, like physi- and chemisorption of oxygen, nucleation and growth of oxide islands and/or a 3-dimensional oxide film covering the metal surface, and subsequent oxide-film growth governed by the coupled currents of cations and/or anions, as well as electrons diffusing through the developing oxide film. For metals such as zirconium, the oxidation process is further complicated by the possible formation of the various intermediate non-stoichiometric oxides and the possible dissolution of oxygen into the metal substrate (cf. Refs. [16, 17, 64]).

The growth kinetics and the developing microstructure (i.e. structure, constitution, morphology and chemical composition) of the grown oxide films, and thereby their chemical and physical properties (e.g. electric conductivity, corrosion resistance, and thermal, chemical and mechanical stability), are related and generally depend on the oxidation conditions (as oxidation temperature and time, partial pressure of oxygen and substrate orientation; cf. Refs. [3, 5, 51, 62, 64]). However, for most metal-oxide systems, the relationships between the oxidation conditions and the resulting oxide-film growth kinetics and microstructure are poorly understood. This is often related to the application of only one dominant experimental technique in most studies. An independent application of a combination of different surface-sensitive analytical techniques (each with its specific advantages and limitations) appears to be required, to arrive at sound, comprehensive conclusions on the oxide-film growth behaviour. In this work it is demonstrated that such a novel, methodologically combined approach, by angle-resolved X-ray Photoelectron Spectroscopy (AR-XPS) and in situ ellipsometry, gives consistent, detailed, and conclusive results on the growth kinetics and the developing constitution and composition of very thin (< 6 nm) oxide-films grown on metal substrates.

Thin oxide films of Zr have recently received considerable attention (cf. Refs. [12, 65]), because they are a serious candidate for the replacement of SiO_2 in thin microelectronic devices. In this work, the initial stages of oxide-film growth on bare Zr substrates by dry, thermal oxidation were investigated at a partial oxygen pressure (pO_2) of 2×10^{-6} Pa within the temperature range of 373 – 773 K. The oxide-film thickness, composition and constitution (i.e. the depth distribution of the different chemical species within the film) were determined by *angle-resolved* X-ray Photoelectron Spectroscopy (AR-XPS). In situ ellipsometry was applied to independently determine quantitatively, in particular, the oxide-film growth kinetics. The obtained results are discussed in terms of the relationships between the oxidation temperature and the resulting oxide-film growth kinetics and microstructure. Quantitative modelling of the observed oxide-film growth kinetics on the bare Zr substrate on the basis of the coupled currents of ions and electrons will be presented in a separate paper [66].

4.2. Experimental details

Disc-shaped, polycrystalline zirconium specimens (diameter of 10 mm; purity > 99.5 wt.%; see Ref. [64]) were prepared (and their surfaces ground and polished) as described in Ref. [64]. The average grain size of the *bare* Zr substrate, as obtained after removal of the native oxide by sputter-cleaning and subsequent annealing at 973 K in UHV, is in the range of 10-50 µm (see the light optical micrograph shown in Fig. 4.1).

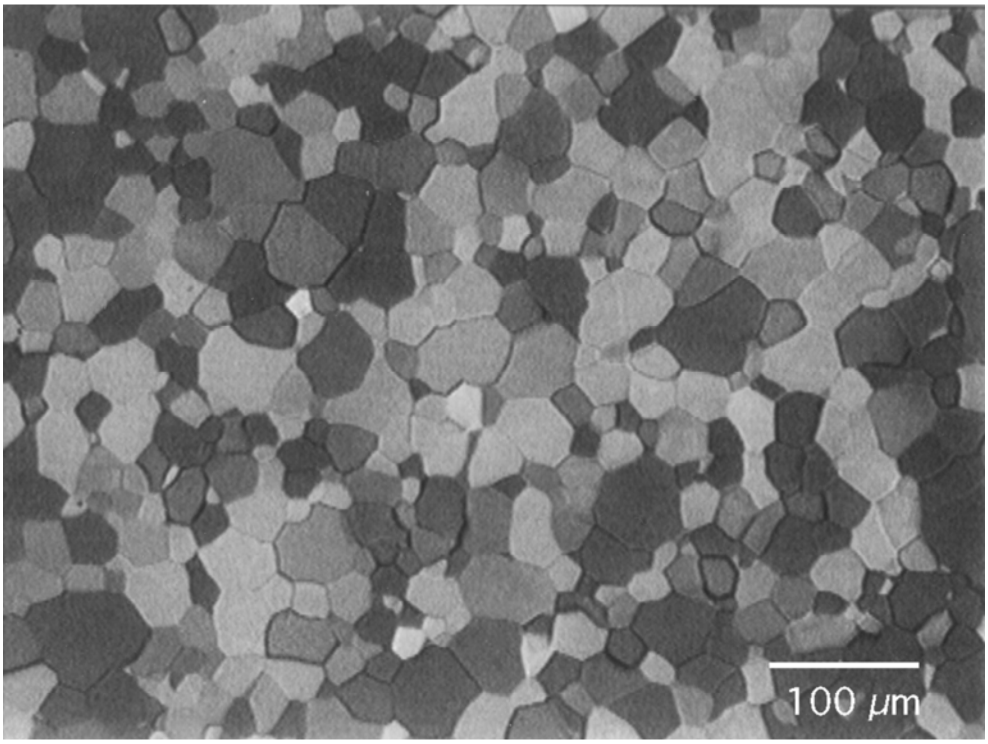

Figure 4.1. Light optical micrograph (in polarized light mode) of an as-prepared polycrystalline Zr specimen after sputter-cleaning and subsequent annealing at 973 K in UHV (short time of etching in a solution (22 ml nitric acid 65%, 5 ml hydrofluoric acid 40 % and 22 ml distilled water) was applied to enhance the contrast between the grains). An average grain size of 10 – 50 µm occur for the Zr crystal bar as obtained by arc melting, cold rolling and subsequent annealing under UHV conditions. For further details on the sample preparation, see Ref. [64].

Oxide films were grown at 375, 475 and 575 K by exposure of a *bare* Zr substrate to pure oxygen gas (99.997 vol.%) at partial oxygen pressures (pO_2) of 2×10^{-6} Pa, for total exposure times varying from 120 to 7200 s. Additionally, four oxidation experiments with a single oxidation time of 7200 s (pO_2 = 2×10^{-6} Pa) were performed at intermediate temperatures of 423 and 523 K, as well as at more elevated temperatures of 673 and 773 K. All oxidations were carried out in a specially designed UHV reaction chamber (RC; base pressure < 2.5×10^{-8} Pa), which is directly coupled to the UHV chamber for the AR-XPS analysis (base pressure < 5×10^{-8} Pa). Before each oxidation experiment, the sample was sputter-cleaned with a 3 kV Ar^+ beam (rastering over an area of about 8×8 mm^2) until no surface contamination of C, O, Ar or some other impurity elements were detected by a XPS measurement over the binding energy (BE) range from 0 to 1400 eV. For further experimental details on sample preparation, sputter-cleaning, annealing and oxidation, see Ref. [64].

Upon oxidation the changes in the value of the ellipsometric phase and amplitude parameters, Δ and Ψ, were measured *in situ* as a function of oxidation time using a Woollam M 2000 L spectroscopic ellipsometer (mounted directly on the flanges of the RC), equipped with a Xe light source. The angles of incidence and reflection of the light were 70° relative to the surface normal. From the Xe spectrum a wavelength (λ) range of 300 nm – 700 nm was used with a step size of 0.8 nm. Spectra of both Δ and Ψ as a function of λ were recorded over a 2-by-8 mm^2 ellipse-shaped area of the sample at time intervals of 3 s.

AR-XPS analysis of the specimen surface before and after oxidation was performed with a VG Thetaprobe system using monochromatic incident Al Kα radiation ($h\nu$ = 1486.68 eV; spot size = 400 μm). Electrons were detected *simultaneously* over the angular range (with respect to the surface normal) of 23 to 83° in six ranges of 10°. The detailed spectra of Zr 3*d* and O 1*s* photoelectron lines were measured with a pass-energy of 50 eV and a step size of 0.05 eV at 64 points equally distributed over an entire analysis area of 3×3 mm^2. It is noted that the entire area analysed with both AR-XPS and ellipsometry included more than 1000 grains of the weakly-textured (as revealed by X-ray diffraction analysis performed in this work) polycrystalline Zr sample (cf. Fig. 4.1), thereby averaging out possible grain-orientation effects on the oxidation.

4.3. Data evaluation

4.3.1. XPS

Before the data evaluation, the series of angle-resolved Zr 3*d* and O 1*s* XPS spectra, as measured at 64 points homogeneously distributed over the analyzed part of the specimen surface (see Sec. 4.2), were averaged for each angular detection range concerned. Next, except for the construction of the effective depth plots in Sec. 4.4.1, single sets of Zr 3*d* and O 1*s* XPS spectra were determined for each measurement of the bare or oxidized Zr substrate by averaging each corresponding series of spectra recorded over the entire angular detection range from 23° to 83°. The thus obtained spectra were then corrected for possible variations of the XPS instrumental parameters, for the transmission function of the hemispherical analyser, as well as for a constant background offset at the lower binding energy (BE) side of each main peak concerned, by adopting the appropriate procedures as described in Ref. [64].

The intrinsic metallic and oxidic contributions to the aforementioned, corrected Zr 3*d* spectra plus their associated inelastic backgrounds were reconstructed following the procedure as described in detail in Refs. [47, 64]. The reconstruction method is based on the convolution of physically realistic functions for the X-ray energy distribution, the core-level main peak, the cross-sections for intrinsic and extrinsic excitations and instrumental broadening.

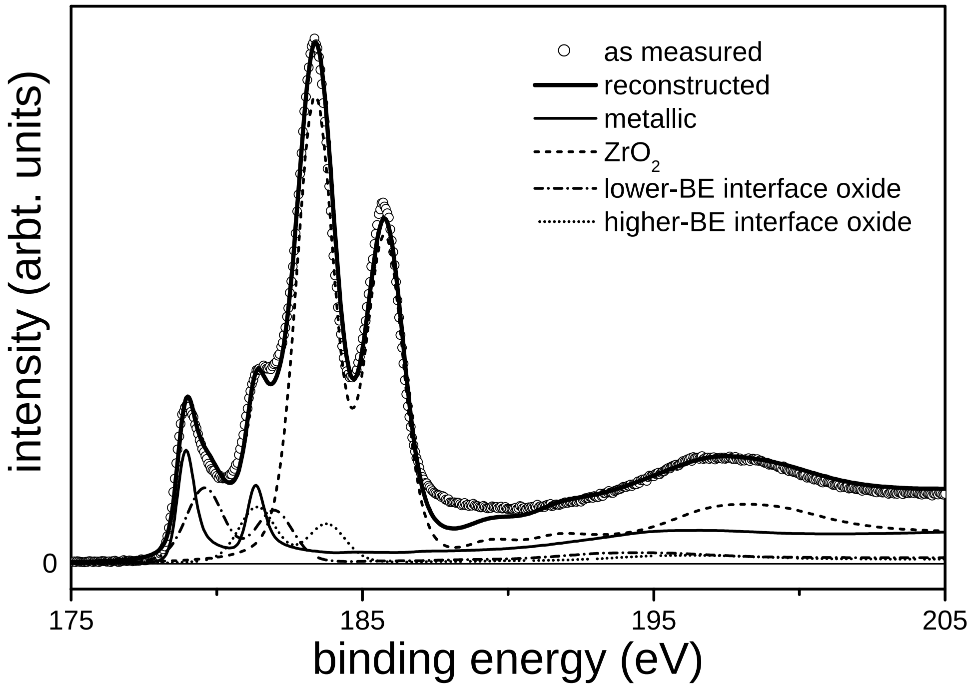

Figure 4.2. Decomposition of a measured Zr 3*d* XPS spectrum of the oxidized Zr metal (averaged over all detection angles from 23° to 83°; see Sec. 4.3.1) into the intrinsic metallic and oxidic contributions plus their associated inelastic backgrounds. The spectrum pertains to the oxidation of a bare Zr substrate for 7200 s at a temperature of 523 K and a pO_2 of 2×10^{-6} Pa. Besides the metallic contribution of the Zr substrate, three different oxidic contributions are recognised: one stoichiometric ZrO_2 and two non-stoichiometric Zr-oxide contributions designated as 'ZrO_2', 'lower-BE interface oxide', and 'higher-BE interface oxide', respectively. See text for details.

The Zr 3*d* spectra recorded from the bare Zr substrate after oxidation could be accurately fitted with one metallic, one oxidic and two weaker suboxidic contributions (Fig. 4.2). As evidenced by the constructed relative depth plot (see Fig. 4.3 in Sec. 4.4.1.1), the two suboxidic components are associated with (non-stoichiometric; see Sec. 4.4.3) oxide species in the region of the oxide film adjacent to the metal/oxide interface, and will therefore be further designated as '*lower-BE interface-oxide*' and '*higher-BE interface-oxide*' component.

Table 4.1. Average binding energy (BE) and full width at half maximum (FWHM) values (and corresponding standard deviations) of the oxidic Zr 3*d* and O 1*s* main peaks, as resolved from the measured Zr 3*d* and O 1*s* XPS spectra of oxidized Zr substrate. The BE values of the resolved oxidic Zr 3*d* and O 1*s* main peaks were all calibrated identifying the BE of the resolved metallic Zr 3*d* main peak with its corresponding reference value of 178.78 eV (see Ref. [67]).

Component	BE, eV	FWHM, eV
Zr 3*d* main peak		
metallic	178.78	0.7
lower-BE interface oxide	179.5 ± 0.1	2.0 ± 0.3
higher-BE interface oxide	181.2 ± 0.1	2.0 ± 0.3
stoichiometric ZrO_2	183.2 ± 0.1	2.0 ± 0.3
O 1*s* main peak		
dissolved ($O_{dissolv}$)	530.1 ± 0.1	0.99 ± 0.1
oxide (O_{ox})	531.2 ± 0.1	1.38 ± 0.1
hydroxide (O_{hydr})	532.5 ± 0.2	1.92 ± 0.1
adsorbed (O_{ads})	534.3 ± 0.4	1.92 ± 0.1

The intrinsic O 1*s* spectra were obtained from the corrected O 1*s* spectra by subtraction of a Shirley type background in the BE range from 528 to 538 eV. Next, the thus obtained O 1*s* spectra were Nonlinear-Least-Squares fitted with up to four symmetrical, mixed Gaussian-Lorentzian peak shapes (while adopting the same Gaussian percentage for each peak shape) (see Fig. 4.4 in Sec. 4.4.1.2 and Table 4.1). This fitting was performed using the Avantage software package (version 2.18) provided by manufacturer (see Sec. 4.2).

The average, total thicknesses and compositions (i.e. O/Zr ratio) of the grown oxide-films were determined following the procedures described in detail in Ref. [64], by using different combinations of the thus obtained total primary zero loss (PZL) intensities of the resolved metallic and oxidic Zr 3*d* and the O 1*s* components, as well as the resolved total PZL Zr 3*d* intensity of the bare metal (including the intrinsic plasmon intensity associated with each main peak [47, 64, 68]). Moreover, values for the individual thicknesses of the stoichiometric ZrO_2 and interface-oxide sublayers were estimated from the corresponding resolved PZL intensities using the procedure described in Appendix A. In the calculations, the molar concentration of Zr in the (top) stoichiometric ZrO_2 sublayer was taking equal to 46.095 mol/dm^3. The value for the molar density of Zr in the Zr-enriched bottom layer was taking equal to the average molar density of Zr in the oxide film, as obtained from the total thickness calculations (see above and Ref. [64]). Its value therefore depends on the oxide-film thickness and the temperature, and varies within the range of 46.1 – 67.4 mol/dm^3. The values for the effective attenuation lengths (EALs; symbol λ^{eff}) used in the calculations were taken from Ref. [64]: i.e. $\lambda^{\mathrm{eff}}_{\mathrm{Zr}^0}$ = 2.32 nm, $\lambda^{\mathrm{eff}}_{\mathrm{Zr}^{\delta+}}$ = 2.23 nm and $\lambda^{\mathrm{eff}}_{\mathrm{O}^{\xi-}}$ = 1.71 nm, for Zr 3*d* electrons traversing through the Zr substrate and through ZrO_2, and for O 1*s* electrons travelling through ZrO_2, respectively.

4.3.2. Ellipsometry

The optical constants and the oxide-film growth kinetics were determined from the in situ ellipsometric measurement of the Zr substrate during oxidation. To this end a model for the developing oxide film has been constructed that is fitted to the measured changes in Ψ and Δ as a function of oxidation time over the wavelength range concerned. It followed that the measured data could be accurately fitted by adopting a Zr substrate covered with a double-layered oxide-film structure, consisting of a sublayer of Zr-enriched oxide adjacent to the metal/oxide interface and a sublayer of stoichiometric ZrO_2 adjacent to the oxide surface. The optical constants of the Zr substrate (as a function of the wavelength) were determined from the in situ measurement of the bare Zr substrate prior to oxidation. For the description of the refractive index of the stoichiometric ZrO_2 sublayer, a Cauchy-type function was used, i.e. $n(\lambda) = a + b/\lambda^2 + c/\lambda^4$ (the extinction coefficient k = 0 over the wavelength range concerned). The optical constants of the non-stoichiometric Zr-oxide sublayer were estimated from the optical constants of the Zr substrate and the ZrO_2 sublayer using the effective medium approximation (EMA) employing the Maxwell-Garnett formulation [56] and taking ZrO_2 as the matrix. For a detailed description of the procedure followed to determine the optical constants of the two oxide sublayers, see Ref. [64]. The thus obtained, optimized values for the Cauchy constants of the ZrO_2 sublayer are a = 1.9412, b = 0 [μm^2] and c = 6.146×10^{-3} [μm^4]. Consequently, the refraction index of ZrO_2 decreases with increasing wavelength λ from n = 2.35 at λ = 350 nm to n = 1.98 at λ = 650 nm. These values agree well with the corresponding literature values reported for (undoped) monoclinic ZrO_2 [57] and amorphous ZrO_2 [58] of n = 2.17 at λ = 632.8 nm and n = 1.98 at λ = 600 nm, respectively. The equivalent volume fraction of Zr metal in the Zr-enriched oxide sublayer (as modelled using the EMA approach; see above and Ref. [64]) is 50.1%.

Values for the oxide-film thicknesses of the two oxide sublayers as a function of the oxidation time (and thereby the total oxide-film growth curves) were determined by fitting the calculated to the experimental spectra of Ψ and Δ with increasing oxidation time over the wavelength range of 350 – 650 nm, using the determined optical constants of the Zr substrate and both oxide sublayers. The fitting was performed as a function of the oxidation time with the WVASE32 software package (version 3.363) [56], while adopting only the thicknesses of both oxide layers as fit parameters.

4.4. Results and discussion

4.4.1. Oxide-film constitution

4.4.1.1. Zr 3d spectra

For all oxidation temperatures and times, the Zr 3*d* photoelectron spectra of the oxidized Zr metal could be accurately fitted with one metallic, one oxidic and two weaker suboxidic components (designated as ZrO_2, lower-BE and higher-BE interface-oxide components, respectively, see Fig. 4.2 and Table 4.1). The relation of the three oxidic components with the oxide-layer microstructure can be deduced on the basis of their relative BE positions in combination with their relative depth-distributions within the oxide film, as evidenced from an effective-depth plot. Such a plot is constructed from the PZL intensities of the metallic and oxidic Zr 3*d* main peaks as resolved from the corresponding AR-XPS spectra recorded at near-normal and grazing photoelectron detection ranges, and provides a direct indication of the effective depth of a given oxidic (or metallic) species below the oxide surface (for further details on the construction of a effective depth plot, see Ref. [64]). The effective depth plot of the resolved metallic and oxidic species, pertaining to the oxidation of the bare Zr substrate

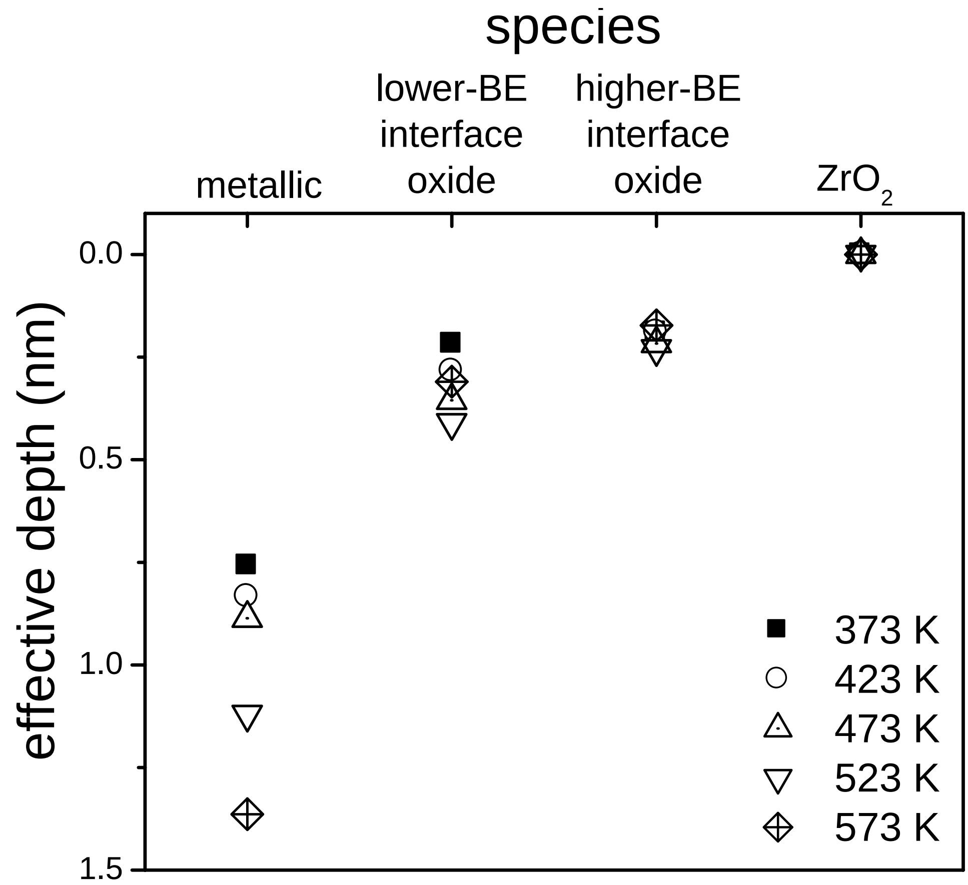

Figure 4.3. Effective depth plot for the metallic Zr, stoichiometric ZrO_2, lower-BE interface-oxide and higher-BE interface-oxide components, as resolved from the measured Zr 3*d* AR-XPS spectra recorded from the bare Zr substrate after oxidation for 7200 s at a pO_2 of 2×10^{-6} Pa for various temperatures (i.e. 373, 423, 473, 523 and 573 K). The markers indicate the effective depths of the species below the oxide surface.

for 7200 s at $pO_2 = 2\times10^{-6}$ Pa and various temperatures, is presented in Fig. 4.3. For the construction of this plot, surface and bulk sensitive detection angular ranges of $\Theta_1 = 53 - 63°$ and $\Theta_2 = 23 - 33°$, respectively, have been used [64].

Evidently, for all temperature applied, the metallic Zr species, corresponding to the Zr substrate, is located at the largest depth and the stoichiometric ZrO_2 species is located at the outer oxide surface. Both interface-oxide components are positioned at depths in between those of the Zr substrate and the outer oxide surface region of stoichiometric ZrO_2 (i.e. in the region of the oxide film adjacent to the metal/oxide interface). The interface-oxide species with the lower BE value (corresponding to the oxide-film region with the higher relative Zr-enrichment; see Ref. [64]) is located closest to the Zr substrate, whereas the higher-BE interface-oxide species (corresponding to the oxide-film region with the lower relative Zr-enrichment; see Ref. [64]) is concentrated in between the lower-BE interface oxide and the outer surface region of stoichiometric ZrO_2. The relative depth distributions and the BE positions of the resolved non-stoichiometric and stoichiometric oxide species indicate the presence of a concentration gradient of Zr and/or O within the grown oxide films going from the metal/oxide interface towards the outer oxide surface (with the degree of relative Zr-enrichment increasing from the stoichiometric ZrO_2 surface region towards the metal/oxide interface). As demonstrated by quantitative AR-XPS analysis, performed as described in Ref. [64], the grown Zr-oxide films are, on average, both enriched in zirconium and depleted of oxygen. This suggests that the initial Zr-oxide films grown on the Zr substrate at low temperatures possess a defect structure consisting of both oxygen vacancies and Zr interstitials that becomes more pronounced towards the metal/oxide interface (the exact defect structure of non-stoichiometric Zr-oxide is still under debate, cf. Refs. [4, 12, 64]). Consequently, the grown oxide films have an overall, non-stoichiometric composition with an average O/Zr-ratio < 2 as determined using XPS (see Sec. 4.4.3).

4.4.1.2. O 1s spectra

For oxidation temperatures $T \leq 573$ K, the background-corrected O 1*s* spectra of the oxidized Zr metal could be accurately fitted with three symmetrical, mixed Gaussian-Lorentzian peak components (see Figs. 4.4a-4.4d, Table 4.1 and Sec. 4.3.1): (*i*) one dominant, lower-BE component (designated as O_{ox}, BE = 531.1 ± 0.1 eV), (*ii*) one weaker, broad, intermediate-BE component (designated as O_{hydr}, BE = 532.5 ± 0.2 eV), and (*iii*) one very weak, broad, higher-BE component (designated as O_{ads}, BE = 534.3 ± 0.4 eV). For higher oxidation temperatures (i.e. $T > 573$ K), one additional, relatively narrow component at the lower BE side of the dominant O_{ox} peak was introduced (designated as $O_{dissolv}$, BE = 530.1 ± 0.1 eV; see Fig. 4.4d and Table 4.1). As for the identified Zr 3*d* oxidic species (see Sec. 4.4.1.1), the relation of the resolved O 1*s* components with the oxide-film microstructure can be deduced on the basis of their relative BE positions in combination with their relative depth distributions within the oxide film.

Effective depth plots of the O_{ox}, O_{hydr}, O_{ads}, $O_{dissolv}$ components, as resolved from the measured O 1*s* XPS spectra of the bare Zr substrate after oxidation for various oxidation times and temperatures ($pO_2 = 2\times10^{-6}$ Pa), are presented in Fig. 4.5. Evidently, the two weak, relatively broad, higher-BE components, O_{hyd} and O_{ads}, are located much closer to the oxide surface than the predominant O_{ox} component, whereas the relatively narrow, lower-BE component, $O_{dissolv}$ (as only observed for $T > 573$ K) is concentrated at the largest depth. This

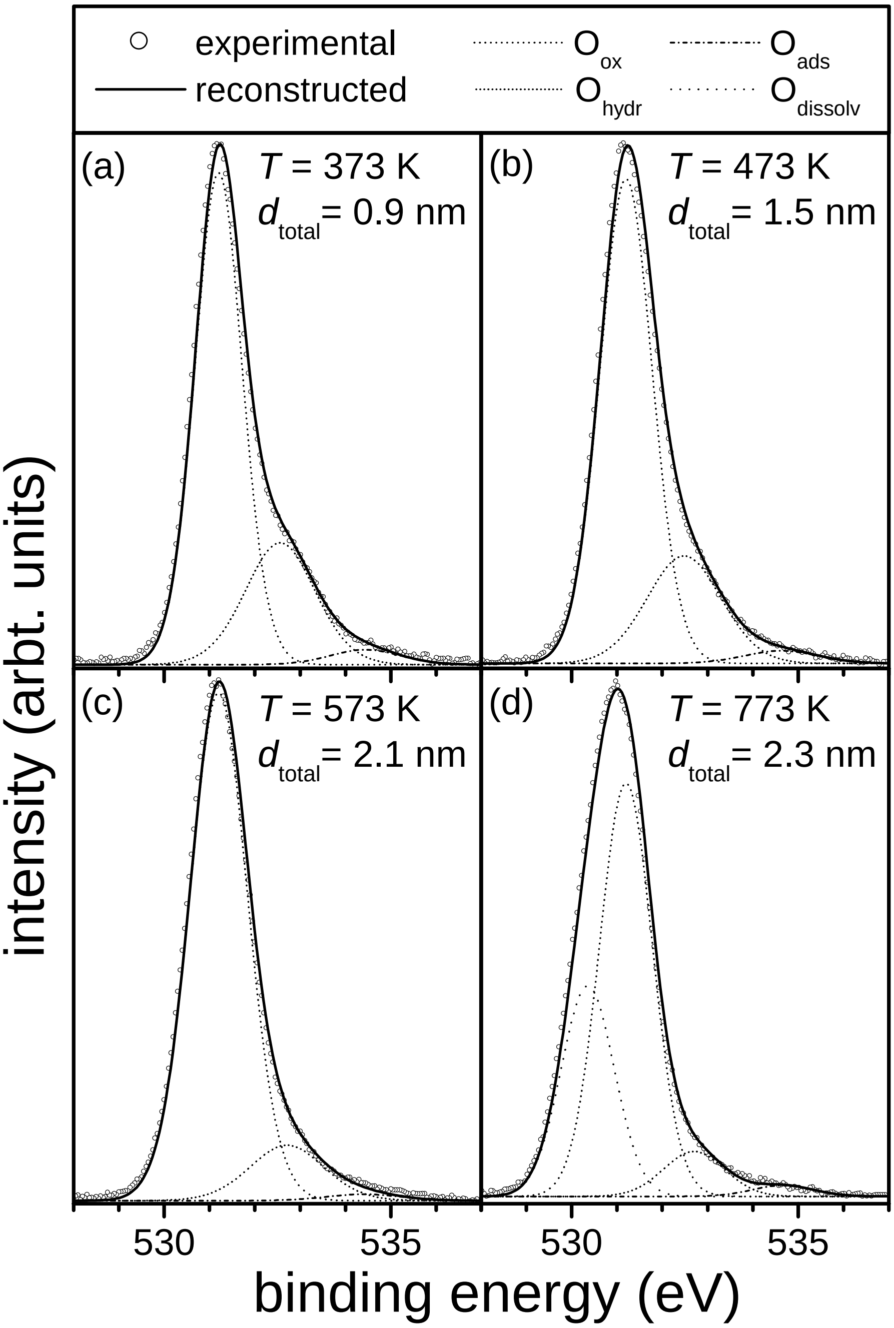

Figure 4.4. O 1*s* main peaks, as resolved by fitting of three (or four; see below) spectral components to the background-corrected O 1*s* XPS spectra recorded from the Zr substrate after oxidation at a pO_2 of 2×10^{-6} Pa, **(a)** for 248 s at $T = 373$ K, **(b)** for 528 s at $T = 473$ K, **(c)** for 1285 s at $T = 573$ K, and **(d)** for 7222 s at $T = 773$ K. The background-corrected and the total reconstructed O 1*s* XPS spectra are represented by the opened dots and the solid lines, respectively. The spectral components designated as $O_{dissolv}$, O_{ox}, O_{hydr} and O_{ads} are attributed to oxygen dissolved in the Zr substrate, bonded to Zr within the oxide film, bonded to hydrogen at the hydroxylated surface and chemisorbed at the oxide surface, respectively. The corresponding total oxide-film thicknesses (d_{total}), as calculated from the metallic and oxidic Zr 3*d* PZL intensities resolved from the XPS spectra of the oxidized metal (see Sec. 4.3), have also been indicated. Note that the $O_{dissolv}$ component is only observed for oxidation temperatures $T > 573$ K.

strongly suggests that the predominant O 1*s* component (O_{ox}) is associated with oxygen bonded to Zr in the 'bulk' of the oxide film (it is therefore designated as oxide-film component, O_{ox}). On the basis of their effective depths within the oxide film, the O 1*s* *surface* components O_{hyd} and O_{ads} *cannot* be related to the previously identified Zr 3*d* lower-BE and higher-BE *interface*-oxide species (see Sec. 4.4.1.1). The $O_{dissolv}$ component is only observed for $T > 573$ K and therefore it can also not be related to the Zr 3*d* lower-BE and higher-BE interface-oxide species (which are observed over the entire temperature range from 300 – 773 K). Thus, the observed compositional gradient within the grown oxide films (see Secs. 4.4.1.1 and 4.4.3) is not revealed by the analysis of the measured O 1*s* XPS spectra. Hence, it follows that (*i*) only the local chemical state of the Zr ions in the grown oxide film is significantly affected by the stoichiometric changes within the oxide film, and (*ii*) the O 1*s* main peaks for the different chemical surroundings in the oxide film cannot be resolved (i.e. their relative shifts are too small with respect to the corresponding FWHMs of the O 1*s* main peaks).

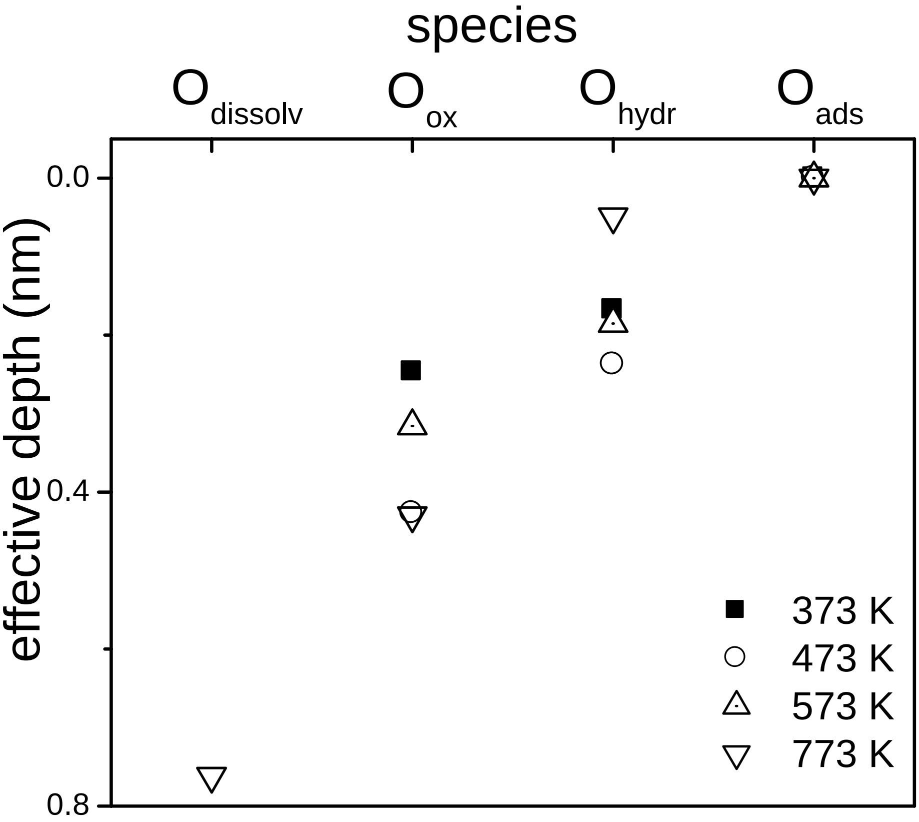

Figure 4.5. Effective depth plot for the oxidic (O_{ox}), hydroxide (O_{hydr}), adsorbed (O_{ads}) and dissolved ($O_{dissolv}$) oxygen components, as resolved from the measured O 1*s* AR-XPS spectra recorded from the bare Zr substrate after oxidation at a pO_2 of 2×10^{-6} Pa for various oxidation times and temperatures (i.e. for 248 s at $T = 373$ K, for 528 s at $T = 473$ K for 1285 s at $T = 573$ K, for 7222 s at $T = 773$ K). The markers indicate the effective depths of the species below the oxide surface.

The observed BE shifts of 1.4 and 3.3 eV of the O_{hydr} and O_{ads} surface components, with respect to the position of the O_{ox} main peak (see Table 4.1), are in agreement with corresponding BE shift ranges of 1.0 – 1.8 eV and 2.2 – 3.5 eV, as reported in the literature [14, 69–72] for hydroxide species and adsorbed (physi- and/or chemisorbed) oxygen species on a metal-oxide surface, respectively. On the basis of the above discussion, the O_{hydr} and O_{ads} components are therefore attributed to hydroxide and adsorbed oxygen species at the outer oxide surface. As discussed in Sec. 4.4.2.3, the $O_{dissolv}$ component, which is located at the largest depth and is only observed for $T > 573$ K, indicates extensive dissolution of oxygen into Zr substrate at these elevated oxidation temperatures.

4.4.2. Oxide-film growth

The average, total oxide-film thickness as a function of the oxidation time (*t*) for the oxidation of the bare Zr substrate in the temperature range of 373 K to 573 K (at $pO_2 = 2\times10^{-6}$ Pa), and as determined by in situ ellipsometry, has been plotted in Fig. 4.6a. As described in Sec. 4.3.2, these *total* oxide-film thickness values (as obtained by in situ ellipsometry) correspond to the sum of the individual thickness values as determined for the stoichiometric ZrO_2 top layer (attributed to the ZrO_2 species) and the non-stoichiometric Zr-oxide bottom layer (attributed to both interface-oxide species; see below). The individual thicknesses of these two oxide sublayers have been plotted in Figs. 4.6b and 4.6c, respectively. For comparison, the total oxide-film thickness versus oxidation time (for 373 K, 473 K and 573 K), as determined from in situ ellipsometry, is plotted together with the corresponding thickness values as determined by AR-XPS in Figs. 4.7a – 4.7c.

4.4.2.1. AR-XPS versus in situ ellipsometry

First of all, it can be concluded that the values for the total oxide-film thickness, as determined from the measured Zr 3*d* XPS spectra of the oxidized Zr substrate (see Sec. 4.3.1), are in good agreement with the corresponding total thickness values (i.e. sum of the thicknesses of the non-stoichiometric and stoichiometric oxide sublayers; see Sec. 4.3.2), as determined *independently* by in situ ellipsometry (see Fig. 4.7). This indicates that the possible effect of roughness of the metal/oxide interface (as effectively also accounted for in the ellipsometric evaluation by using an EMA approach for the interface-oxide sublayer; see Sec. 4.3.2 and Ref. [64]) is in any case very small. Especially for the lowest temperatures studied, the agreement between the independently determined thickness values is very good,

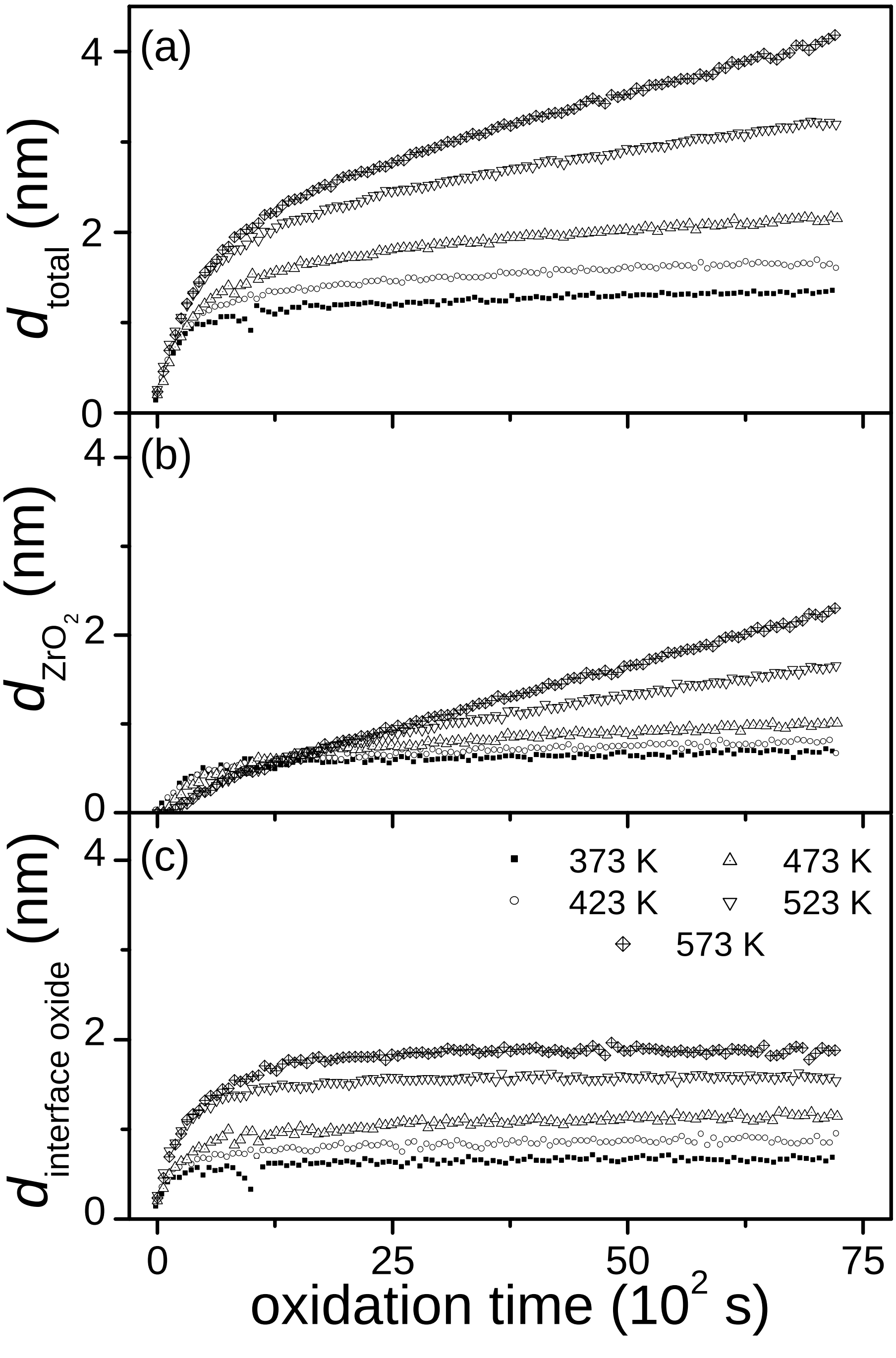

Figure 4.6. **(a)** The total oxide-film thickness (d_{total}), as well as the corresponding individual thicknesses of the **(b)** stoichiometric ZrO_2 top (d_{ZrO_2}) and **(c)** the relative Zr-enriched bottom ($d_{interface\ oxide}$) interface-oxide sublayers, as a function of oxidation time, for the oxidation of the bare Zr substrate at pO_2 of 2×10^{-6} Pa within the temperature range of 373 to 573 K. The oxide-film thickness values were determined from the measured spectra of the phase and amplitude parameters, Δ and Ψ, over the wavelength range of 350 – 650 nm as recorded with in situ multi-wavelength ellipsometry. The ZrO_2 top sublayer and the Zr-enriched bottom sublayer correspond with the stoichiometric ZrO_2 and sum of the lower-BE and higher-BE interface-oxide species as identified with AR-XPS, respectively (cf. Figs. 4.2, 4.3 and 4.8). The scatter, imposed on the growth curve at around 25 and 20 min of oxidation at 373 and 473 K, respectively, was caused by externally induced sample vibrations.

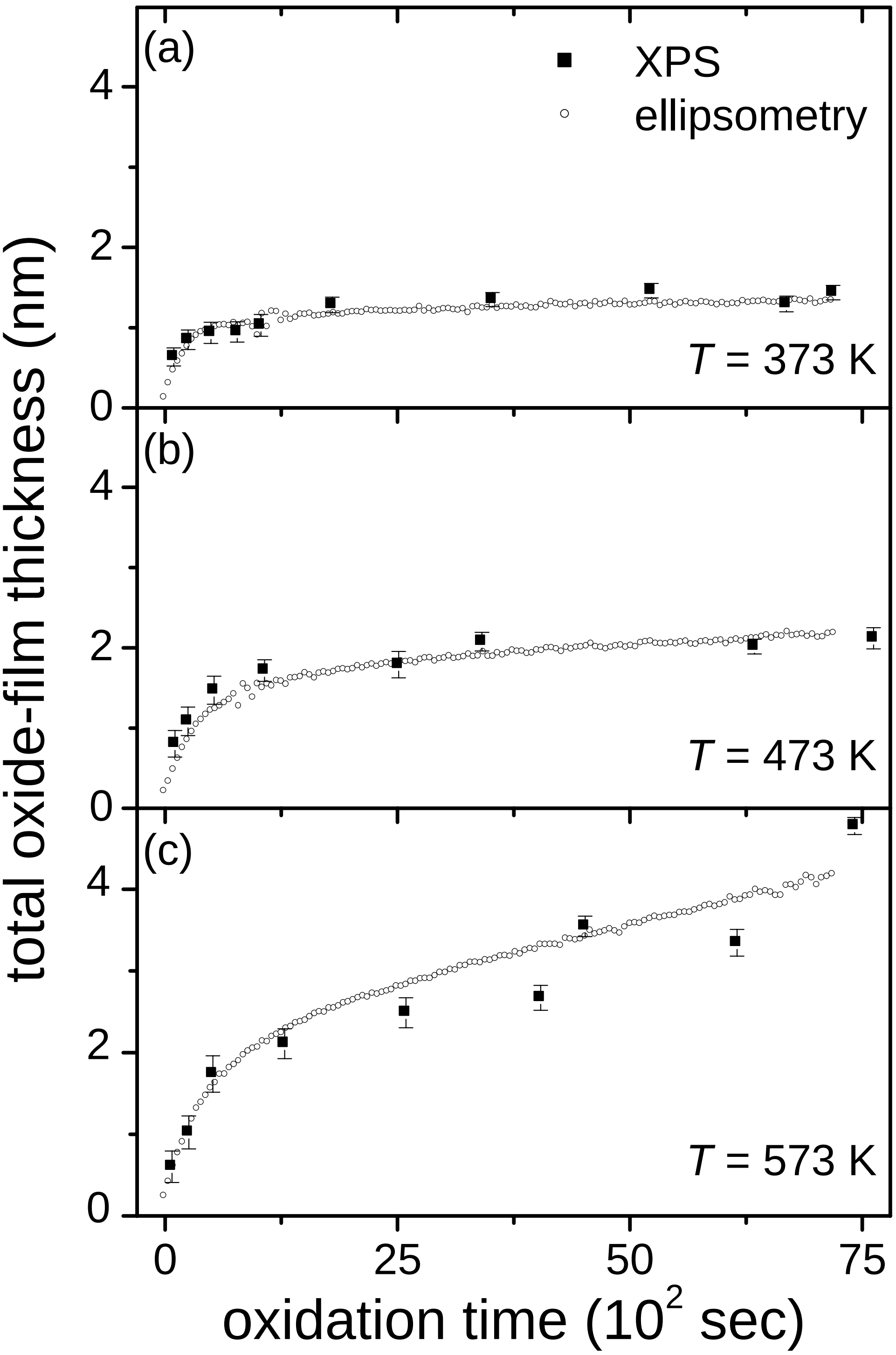

Figure 4.7. Total oxide-film thickness as a function of oxidation time, for the oxidation of the bare Zr substrate at $pO_2 = 2\times10^{-6}$ Pa and temperatures of **(a)** 373 K, **(b)** 473 K and **(c)** 573 K. The total oxide-film thickness values were determined *independently* from (*i*) the measured Zr 3*d* photoelectron spectra recorded from the bare and oxidized Zr substrate using XPS, and (*ii*) from the measured spectra of the phase and amplitude parameters, Δ and Ψ, over the wavelength range of 350 – 650 nm as recorded with in situ ellipsometry. The error bars for the XPS thicknesses correspond to the standard deviation of the six thickness values, calculated by using different combinations of the resolved PZL intensities (see Sec. 4.3.1 and Ref. [64] for details).

presumably because the amorphous oxide films grown at low temperatures (cf. Ref. [64]) are of more uniform thickness than the likely more irregular (cf. Ref. [50, 60]) oxide films expected to be formed at higher temperatures.

It can be verified that the individual thickness of the non-stoichiometric interface-oxide sublayer, as determined by in situ ellipsometry (cf. Fig. 4.6c), indeed corresponds to the sum of the lower-BE and higher-BE interface oxide species, as determined by AR-XPS (cf. Figs. 4.2 and 4.3). To this end, the total thicknesses of the non-stoichiometric and stoichiometric regions in the oxide film were estimated independently from the *sum* of the PZL intensities of the lower-BE and higher-BE interface oxide species, and the PZL intensity of the ZrO_2 species, as resolved from the measured Zr 3*d* spectra of the oxidized Zr metal (cf. Fig. 4.2), by following the procedure as outlined in Appendix A. The individual thicknesses of the non-stoichiometric and stoichiometric oxide sublayers, as thus determined *independently* by XPS and by in situ ellipsometry, are plotted as a function of the oxidation time for the various temperatures studied in Figs. 4.8a-4.8c and Figs. 4.8d-4.8f, respectively. In spite of the rough approximations adopted for the calculation of the individual thickness values from the resolved Zr 3*d* photoelectron intensities (see Appendix A),[6] the estimated thickness values for the non-stoichiometric interface-oxide and stoichiometric ZrO_2 sublayers are consistent with the corresponding (more reliable) thickness values as determined by in situ ellipsometry. The small discrepancies between the calculated XPS and ellipsometry thickness values are most likely caused by errors in the XPS calculation due to the assumption of sharp interfaces between the non-stoichiometric and stoichiometric oxide regions and between the substrate and the oxide film. Hence, it can be concluded that the relatively Zr-enriched interface-oxide layer, as identified by in situ ellipsometry, corresponds to the sum of the lower-BE and higher-BE interface oxide species, as identified with XPS.

4.4.2.2. Oxide-film growth kinetics

Clearly, for all temperatures studied, the *total* oxide-film growth kinetics can be subdivided into two different growth regimes: an initial regime of very fast oxide-film growth, which is followed by a second, much slower growth stage of about constant growth rate, at constant temperature, which increases with increasing temperature (see Fig. 4.6a). For low

---

[6] In the calculation of Appendix A, an oxide-film of uniform thickness with sharp interfaces between stoichiometric and non-stoichiometric interface-oxide sublayers have been assumed.

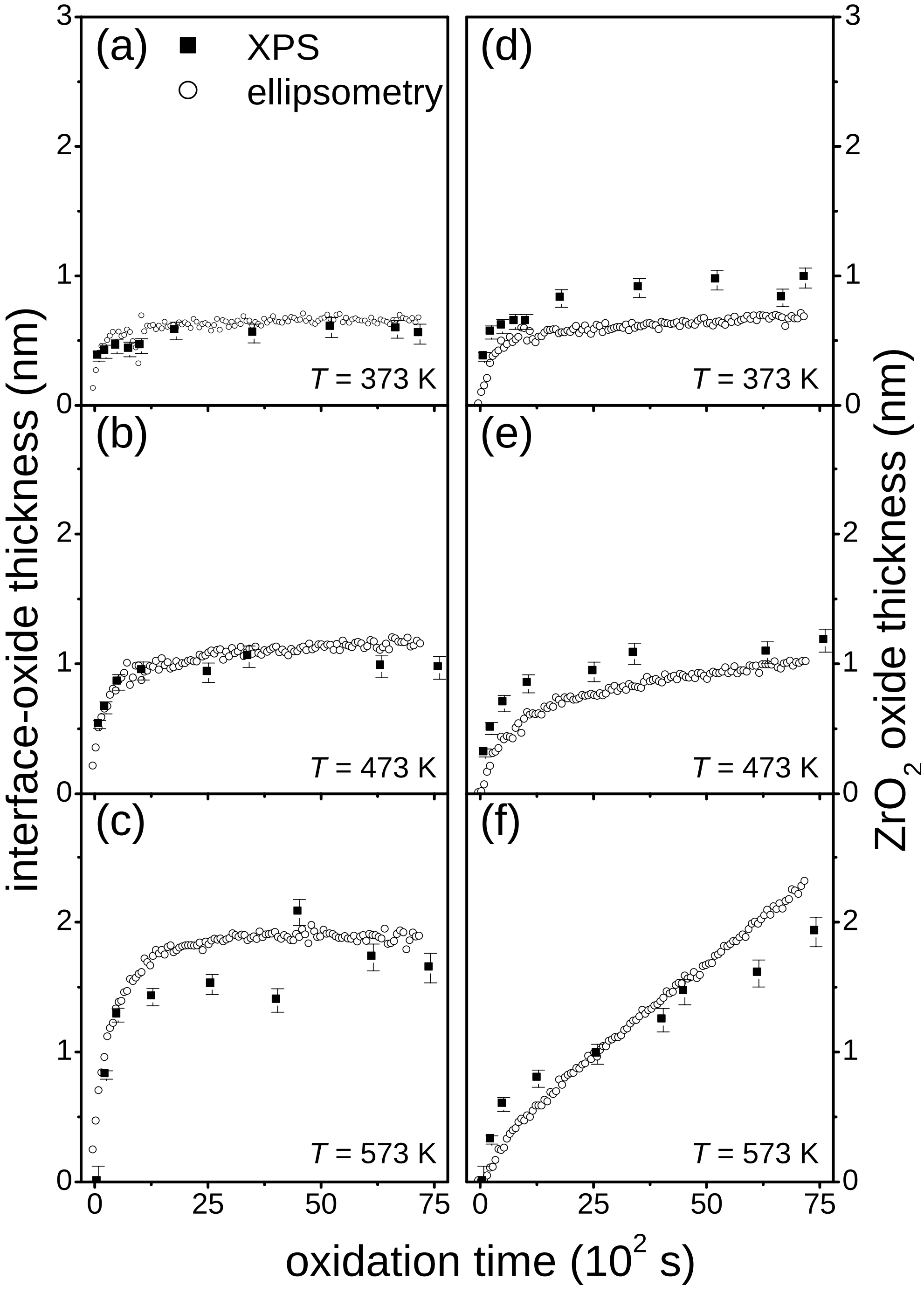

Figure 4.8. Individual thicknesses of **(a-c)** the non-stoichiometric (i.e. relative Zr-enriched) interface-oxide sublayer, and **(d-f)** the stoichiometric ZrO_2 sublayer, as a function of oxidation time for various temperatures, as determined independently from XPS and in situ ellipsometry. The XPS thickness values were calculated from the metallic and oxidic PZL intensities, as resolved from the measured Zr 3*d* spectra of oxidized Zr substrate (see Sec. 4.3.1 and Appendix A). The ellipsometry thicknesses were resolved from the in situ ellipsometric measurements of the oxidizing Zr substrate (see Sec. 4.3.2 and Ref. [64]). The error bars for the XPS thicknesses correspond to the errors introduced in the calculated thickness values for a 10% error in the resolved XPS intensities.

temperatures up to, say, about 473 K, the growth rate drastically drops at the end of the initial growth stage, becoming very small for the second oxidation stage (see Fig. 4.6a).

A distinct difference in growth kinetics is observed for the surface adjacent stoichiometric ZrO_2 sublayer and the non-stoichiometric interface-oxide sublayer, as demonstrated by in situ ellipsometry (see Figs. 4.6b and 4.6c). For the temperature range considered (i.e. 373 – 573 K), the thickness of the interface-oxide sublayer shows a very fast increase during the initial, fast oxidation regime, after which the thickness levels off, attaining a constant 'limiting' thickness at the onset of the second, slow oxidation stage (see Fig. 4.6c). The limiting thickness of the non-stoichiometric oxide reached at the onset of the second oxidation stage increases with increasing temperature: i.e. at 373, 423, 473, 523 and 573 K a 'limiting' thickness of about 0.6 nm, 0.7 nm, 0.9 nm, 1.4 nm and 1.8 nm is reached after about 500, 700, 830, 1110 and 1375 s, respectively (see Fig. 4.6c).

The thickness of the stoichiometric ZrO_2 sublayer also shows a fast increase during the initial stage (although its growth rates are somewhat slower than those of the non-stoichiometric interface-oxide sublayer), but no limiting oxide-film thickness is attained for the stoichiometric sublayer during the second slow growth stage for $T > 423$ K. Further, with increasing temperature the onset of growth of the ZrO_2 sublayer becomes slightly delayed (the onset time increases with increasing temperature; compare Figs. 4.6b and 4.6c). The continued growth of the ZrO_2 sublayer during the second growth stage for $T > 423$ K follows an approximately linear growth law, for which the constant growth rate increases with increasing temperature (Fig. 4.6b).

It can be concluded that the onset of oxidation starts with the formation and predominant growth of non-stoichiometric Zr-oxide up to a certain limiting thickness that increases with increasing temperature. Continued growth of the oxide film during the second growth stage is then solely determined by the continued, approximately linear growth of stoichiometric ZrO_2 on top of the non-stoichiometric oxide.

4.4.2.3. Oxygen dissolution and oxide decomposition

Additional oxidation experiments were performed at more elevated temperatures of 673 and 773 K (cf. Sec. 4.2). It was not possible to properly describe the in situ recorded ellipsometric data for the oxidation of the Zr substrate at 673 and 773 K using the doubled-layer oxide structural model, as successfully adopted for the description of the ellipsometric data within the temperature range 373 – 573 K (see Sec. 4.4.2.2). Moreover, analysis of the measured Zr 3*d* XPS spectra of the oxidized metal indicates that the oxide-films grown after 7200s of oxidation at 673 and 773 K are considerably *thinner* than the corresponding oxide films grown at a lower temperature of 573 K for the same time of oxidation (i.e. 1.6 and 2.3 nm for 673 and 773 K versus 4.8 nm for 573 K, respectively). Upon oxidation at these elevated temperatures of 673 and 773 K, an additional component (designated as $O_{dissolv}$) emerges in the measured O 1*s* XPS spectra of the oxidized metal (cf. Sec. 4.4.1.2 and Fig. 4.4d).

The above observations and results can be explained by the co-occurrence of two competing different processes upon oxidation of the bare Zr substrate at $T > 573$ K: (*i*) the formation and continued growth of the oxide film, as described in Sec. 4.2.2, and (*ii*) the dissolution and inward diffusion of oxygen in the Zr substrate (possibly following a parabolic rate; cf. Ref. [4]) in association with partial decomposition of the developing oxide film [4, 16]. The diffusion coefficient of oxygen in the α-Zr at 523 K is (more than) a factor 500 lower than at 673 K and 723 K (1.17×10^{-18} cm^2 s^{-1} at 523 K versus 5.45×10^{-16} cm^2 s^{-1} at 673 K and 4.13×10^{-15} cm^2 s^{-1} at 723 K [17]). Also, the maximum amount of oxygen that can be dissolved in α-Zr increases with increasing temperature: $O_{dissolv}$ (at.%) = $28.6 + \exp(-6748T^{-1}+4.748)$ for $473 \leq T \leq 1478$ K [73]. An alternative explanation of a growth rate decreasing with increasing temperature can be due to a rate of oxygen desorption from the oxide surface increasing with increasing temperature, as observed for the initial oxidation of others metals at relative low pO_2 (cf. Ref. [62]). However, such an effect is generally only observed for the initial, fast oxidation stage and not for the second, slow growth stage as is the case here.

Because of the extensive dissolution of oxygen for $T > 573$ K, the optical properties of the bare Zr substrate change upon oxidation at $T > 523$ K. Consequently, the optical constants of the bare Zr substrate as determined with in situ ellipsometry prior to the oxidation (see Sec. 4.2) can no longer be adopted as constants in the evaluation of the measured ellipsometry data using the double-layered structural model (see Sec. 4.3.2). Therefore, the description of the ellipsometric data using the doubled-layer oxide structural model fails for the oxidation of the Zr substrate at 673 and 773 K (see above).

4.4.3. Oxide-film composition

The composition, expressed as the average O/Zr-ratio, of the grown oxide-films has been plotted as a function of the total oxide-film thickness for temperatures of 373, 473 and 573 K in Fig. 4.9. For all temperatures studied, an initially non-stoichiometric oxide film has formed with an overall O/Zr-ratio lower than the stoichiometric ratio of 2 for ZrO_2 (the initial O/Zr-ratio decreases with increasing temperature). The O/Zr-ratio increases, approximately linearly, with increasing oxide-film thickness until it saturates at an O/Zr-ratio close to 2 during the second, slow oxidation stage at elevated temperatures. The evolution of the oxide-film composition as a function of thickness and temperature can be explained by considering the individual growth kinetics of the stoichiometric ZrO_2 and non-stoichiometric interface-oxide, as resolved by in situ ellipsometry (see Figs. 4.6b and 4.6c) and as discussed in Sec. 4.4.2.2. The oxidation of the bare Zr substrate starts with the formation and growth of a non-stoichiometric (i.e. relative Zr-enriched) oxide up to a certain limiting thickness (that increases with increasing temperature). Continued growth of the oxide film during the second oxidation stage is realised by the overgrowth of stoichiometric ZrO_2, which explains the observed, overall increase of the O/Zr-ratio of the developing oxide film with increasing thickness (see Fig. 4.9).

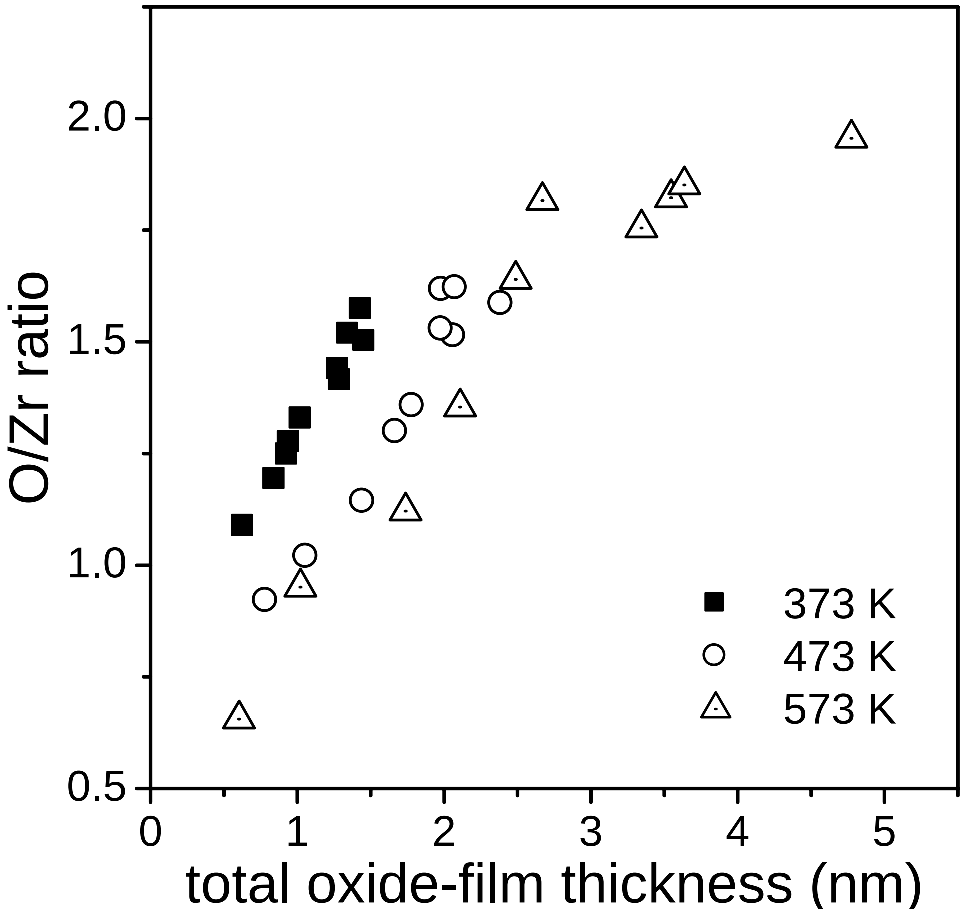

Figure 4.9. The overall composition, expressed as the average O/Zr-ratio, of the grown oxide film as a function of the total oxide-film thickness, for the oxidation of the bare Zr substrate at a $pO_2 = 2\times10^{-6}$ Pa and temperature 373, 473 and 573 K. The values for the O/Zr-ratio were determined from the total oxidic Zr 3*d* and O 1*s* PZL intensities as resolved from the measured Zr 3*d* and O 1*s* photoelectron spectra recorded from the oxidized Zr substrate using XPS (see Sec. 4.3.1).

The overall low O/Zr-ratio of the grown oxide films can be attributed to a Zr-enrichment and O-deficiency (see Sec. 4.4.1.1) of the grown oxide films in the region adjacent to the metal/oxide interface, with the degree of relative Zr-enrichment decreasing from the metal/oxide interface towards to the oxide surface. This gradient in the oxide-film composition leads to the appearance of the associated lower-BE and higher-BE interface-oxide components in the measured Zr 3*d* XPS spectra of the oxidized Zr metal (see Fig. 4.2).

A change in composition (i.e. a relative enrichment of cations) of the oxide film in the region adjacent to the oxide/metal interface has also been observed for other metal substrate/oxide-film systems (cf. Refs. [14, 61]), and has been conceived as a consequence of the contact potential established at the metal/oxide interface to equilibrate the intrinsic Fermi level of the oxide (insulator) with that of the metal substrate (conductor) (cf. Refs. [62, 63]).

4.4.4. Oxide-film growth mechanisms

The occurrence of an initial, very fast oxidation regime, followed by a second stage of much slower, but continued oxide-film growth, as observed here for the oxidation of the bare Zr substrate within the temperature range 373 – 573 K (see Fig. 4.6), is typical for the initial oxidation of metals up to moderately high temperatures (of say, $T < 773$ K). An interpretation of this growth behaviour is possible on the basis of ideas, proposed by Mott and Cabrera [21] and by Fromhold and Cook [23, 24] (see review in Refs. [49, 74]).

The extremely high oxidation rates during the initial growth regime (but after formation of a continuous, closed oxide film on the metal surface) are achieved by the electric-field enhanced migration of cations through the developing oxide film. The electric-field strength, which effectively lowers the activation energy for outward cation diffusion, arises due to the so-called Mott potential setup between the electronic states at the Fermi level in the metal and the acceptor levels provided by oxygen species adsorbed onto the oxide surface. The fast initial oxidation rates are maintained as long as the Mott potential is sustained by the relatively fast, forward and reverse fluxes of electrons tunnelling through the developing oxide film. Because the electron-tunnelling current decreases exponentially with increasing oxide-film thickness, the Mott potential breaks down in a narrow thickness range (usually around 1 nm for most metal-oxide systems; cf. Refs. [62, 74]). Under the constraint of coupled currents of electrons and cations, it then follows that a significant drop in the oxide-film growth rate occurs upon attaining a critical thickness (corresponding with the transition from the initial, fast to second, slow oxidation growth stage; cf. Fig. 4.6a). Since, electron transport due to tunnelling has only a very weak temperature dependence [23, 74], the critical oxide-film thickness is expected to be approximately independent on the oxidation temperature. However, a distinct increase of the critical oxide-film thickness with temperature is observed here (see Fig. 4.6). This observed temperature dependence of the critical thickness must be related to the defect structure of the corresponding, overall non-stoichiometric, oxide-film (i.e. the increase of the critical oxide-film thickness with increasing temperature is accompanied by a decrease of the average O/Zr-ratio of the oxide film; cf. Figs. 4.6a and 4.9) [62, 75].

At low temperatures, the concentration-gradient-driven diffusion of cations and/or anions into and through the oxide film, as well as the rate of electron transport by thermionic emission (a process that is *independent* of the oxide-film thickness), are negligibly small. Therefore, at low temperatures oxidation stops at a limiting thickness. However, at elevated temperatures (here $T \geq 473$ K; see Fig. 4.6a and Ref. [62]), their contributions can no longer be neglected. Then continued oxide-film growth during the second oxidation stage is realised by the coupled currents of electrons (by thermionic emission), and cations and/or anions, under influence of the so-called kinetic (or equilibrium) potential, which lies in between the Mott potential (if electron transport is only due to the tunnelling mechanism) and the ionic diffusion potential (if electron transport is only due to thermionic emission) [24]. The electric field due to the kinetic potential will be directed such as to enhance the transport of the intrinsically slower species. Since the process of electron transport by thermionic emission is orders of magnitude slower than the initial electron tunnelling process, it follows that the resulting electric field due to the kinetic potential will be much weaker than the electric field induced by the Mott potential during the initial, fast oxidation stage. Consequently, the oxide-film growth rate for the second oxidation stage is considerably smaller than the initial oxide-film growth rate (cf. Fig. 4.6a).

4.5. Conclusions

Investigation of the initial oxidation of a bare metal substrate by combining *angle-resolved* XPS (AR-XPS) and *in situ* multi-wavelength ellipsometry, can give consistent, detailed and conclusive information on the growth kinetics, constitution and chemical composition of the initial oxide-film grown on the metal as a function of the oxidation temperature and time. This novel, combined, methodological approach has led to the following results for the initial, thermal oxidation of bare, polycrystalline Zr substrates in the temperature range of 373 – 773 K (at a partial oxygen pressure of 2×10^{-6} Pa).

The initial stage of oxidation of the bare Zr substrate involves very fast, oxide-film growth. At lower temperatures (≤ 423 K), oxidation stops after the first stage at a limiting thickness that increases with temperature (0.6 nm at 373 K; 0.7 nm at 423 K). At elevated temperatures (> 423 K), a second stage of much slower, but continued oxide-film growth occurs. The very fast, initial growth rate during the initial oxidation stage is ascribed to electric-field-controlled, coupled currents of electrons (by tunnelling) and Zr cations under influence of the Mott potential. Subsequent, continued growth during the second oxidation stage for $T > 423$ K is realised by coupled currents of electrons (by thermionic emission) and cations/anions under influence of the kinetic potential.

The first stage of oxidation involves the formation and growth of a non-stoichiometric oxide film with an overall O/Zr-ratio < 2 (the initial O/Zr-ratio decreases with increasing temperature). The overall, non-stoichiometric composition arises from a concentration gradient of Zr-enrichment and O-deficiency in the developing oxide film that decreases from metal/oxide interface towards the oxide surface. It leads to the presence of three oxide components in the oxide film: the surface adjacent ZrO_2, and two non-stoichiometric, relative Zr-enriched oxides, near the interface with the substrate. It is the non-stoichiometric interface-oxide sublayer that attains the limiting thickness (that increases with increasing temperature) at the end of the initial, fast oxidation stage. Continued oxide-film growth during the second growth stage (for $T > 423$ K) proceeds by the approximately linear, overgrowth of the stoichiometric ZrO_2.

At elevated oxidation temperatures ($T > 573$ K), extensive dissolution of oxygen into the Zr substrate occurs, which results in the appearance of an additional component in the measured O 1*s* AR-XPS spectra of the oxidized Zr metal for $T > 573$ K. This oxygen dissolution process is accompanied by the partial decomposition of the developing oxide film, resulting in an effective reduction of the total oxide-film growth rate as compared to lower temperatures.

Appendix A. Calculation of oxide-sublayer thicknesses

The recorded PLZ intensity, I_A, of photoelectrons emitted with the kinetic energy E from the n^th core level of an atom (or ion) A, situated in a solid at depth z below the solid's surface in given by (cf. Ref. [76]):

$$I_\mathrm{A} = K \cdot \sigma_\mathrm{A} \cdot \lambda_\mathrm{A}^\mathrm{eff} \int_{z=0}^{\infty} C_\mathrm{A}(z) \cdot \exp\left(-\int_{z'=0}^{z} \frac{dz'}{\lambda_\mathrm{A}^\mathrm{eff}(z') \cdot \cos\theta} \right) dz \qquad (4.\mathrm{A}1)$$

where K is an instrumental factor depending on the area analysed, the X-ray energy and intensity, etc.; σ_A is the total photoionization cross-section; C_A(z) is the molar density of A atoms (i.e. number of A atoms per unit volume) as a function of depth z below the surface; $\lambda_\mathrm{A}^\mathrm{eff}(z')$ is the effective attenuation length (EAL) of the detected photoelectrons of kinetic energy E in the solid as a function of depth z below the surface; and the detection angle θ is defined as the angle between the sample surface normal and solid acceptance angle of analyser.

In the case of a Zr substrate covered by a homogenous Zr-oxide film of uniform thickness, d, the oxidic and metallic PZL intensities $I_{\mathrm{Zr}^{\delta+}}$ and I_{Zr^0} of the photoelectrons emitted from the Zr 3d core levels of the $\mathrm{Zr}^{\delta+}$ ions in the oxide film and of the Zr atoms in the substrate, are given by:

$$I_{\mathrm{Zr}^{\delta+}} = K'' \cdot \sigma_\mathrm{Zr} \cdot C_{\mathrm{Zr}^{\delta+}} \cdot \lambda_{\mathrm{Zr}^{\delta+}}^\mathrm{eff} \cdot \cos\theta \cdot \left[1 - \exp\left(-\frac{d}{\lambda_{\mathrm{Zr}^{\delta+}}^\mathrm{eff} \cdot \cos\theta} \right) \right] \qquad (4.\mathrm{A}2\mathrm{a})$$

and

$$I_{\mathrm{Zr}^0} = K'' \cdot \sigma_\mathrm{Zr} \cdot C_{\mathrm{Zr}^0} \cdot \lambda_{\mathrm{Zr}^0}^\mathrm{eff} \cdot \cos\theta \cdot \exp\left(-\frac{d}{\lambda_{\mathrm{Zr}^{\delta+}}^\mathrm{eff} \cdot \cos\theta} \right) \qquad (4.\mathrm{A}2\mathrm{b})$$

respectively.

For the case of double-layered oxide-film structure on top of the Zr substrate (with d_t and d_b defined as the thicknesses of top and bottom oxide sublayers, respectively), the metallic and oxidic PZL intensities I_{Zr^0}, $I_{\mathrm{Zr}^{\delta+}}^\mathrm{t}$ and $I_{\mathrm{Zr}^{\delta+}}^\mathrm{b}$ of the photoelectrons emitted from the Zr 3d core-level of Zr atoms in the substrate and $\mathrm{Zr}^{\delta+}$ ions in the top and bottom oxide layers, are given by:

$$I_{\mathrm{Zr}^0} = K''' \cdot C_{\mathrm{Zr}^0} \cdot \lambda_{\mathrm{Zr}^0}^{\mathrm{eff}} \cdot \cos\theta \cdot \exp\left(\frac{d_\mathrm{t} - d_\mathrm{b}}{\lambda_{\mathrm{Zr}^{\delta+}}^{\mathrm{eff}} \cdot \cos\theta} \right) \tag{4.A3a}$$

$$I_{\mathrm{Zr}^{\delta+}}^{\mathrm{t}} = K''' \cdot C_{\mathrm{Zr}^{\delta+}}^{\mathrm{t}} \cdot \lambda_{\mathrm{Zr}^{\delta+}}^{\mathrm{eff}} \cdot \cos\theta \cdot \left[1 - \exp\left(\frac{-d_\mathrm{t}}{\lambda_{\mathrm{Zr}^{\delta+}}^{\mathrm{eff}} \cdot \cos\theta} \right) \right] \tag{4.A3b}$$

and

$$I_{\mathrm{Zr}^{\delta+}}^{\mathrm{b}} = K''' \cdot C_{\mathrm{Zr}^{\delta+}}^{\mathrm{b}} \cdot \lambda_{\mathrm{Zr}^{\delta+}}^{\mathrm{eff}} \cdot \cos\theta \cdot \left[1 - \exp\left(\frac{-d_\mathrm{b}}{\lambda_{\mathrm{Zr}^{\delta+}}^{\mathrm{eff}} \cdot \cos\theta} \right) \right] \cdot \left[\exp\left(\frac{-d_\mathrm{t}}{\lambda_{\mathrm{Zr}^{\delta+}}^{\mathrm{eff}} \cdot \cos\theta} \right) \right] \tag{4.A3c}$$

respectively.

By taking appropriate values for the molar concentrations of Zr in the oxide sublayers, individual thicknesses for the top and bottom oxide sublayers can be calculated by iteration from the intensity ratios $I_{\mathrm{Zr}^0} / I_{\mathrm{Zr}^{\delta+}}^{\mathrm{t}}$, $I_{\mathrm{Zr}^0} / I_{\mathrm{Zr}^{\delta+}}^{\mathrm{b}}$ and $I_{\mathrm{Zr}^{\delta+}}^{\mathrm{t}} / I_{\mathrm{Zr}^{\delta+}}^{\mathrm{b}}$, i.e.

$$\frac{I_{\mathrm{Zr}^0}}{I_{\mathrm{Zr}^{\delta+}}^{\mathrm{b}}} = \frac{C_{\mathrm{Zr}^0} \cdot \lambda_{\mathrm{Zr}^0}^{\mathrm{eff}} \cdot \exp\left(- \dfrac{d_\mathrm{b}}{\lambda_{\mathrm{Zr}^{\delta+}}^{\mathrm{eff}} \cdot \cos\theta} \right)}{C_{\mathrm{Zr}^{\delta+}}^{\mathrm{b}} \cdot \lambda_{\mathrm{Zr}^{\delta+}}^{\mathrm{eff}} \cdot \left[1 - \exp\left(\dfrac{-d_\mathrm{b}}{\lambda_{\mathrm{Zr}^{\delta+}}^{\mathrm{eff}} \cdot \cos\theta} \right) \right]} \tag{4.A4a}$$

$$\frac{I_{\mathrm{Zr}^0}}{I_{\mathrm{Zr}^{\delta+}}^{\mathrm{t}}} = \frac{C_{\mathrm{Zr}^0} \cdot \lambda_{\mathrm{Zr}^0}^{\mathrm{eff}} \cdot \exp\left(- \dfrac{d_\mathrm{t} + d_\mathrm{b}}{\lambda_{\mathrm{Zr}^{\delta+}}^{\mathrm{eff}} \cdot \cos\theta} \right)}{C_{\mathrm{Zr}^{\delta+}}^{\mathrm{t}} \cdot \lambda_{\mathrm{Zr}^{\delta+}}^{\mathrm{eff}} \cdot \left[1 - \exp\left(\dfrac{-d_\mathrm{t}}{\lambda_{\mathrm{Zr}^{\delta+}}^{\mathrm{eff}} \cdot \cos\theta} \right) \right]} \tag{4.A4b}$$

and

$$\frac{I_{\mathrm{Zr}^{\delta+}}^{\mathrm{t}}}{I_{\mathrm{Zr}^{\delta+}}^{\mathrm{b}}} = \frac{C_{\mathrm{Zr}^{\delta+}}^{\mathrm{t}} \cdot \exp\left(\dfrac{-d_\mathrm{t}}{\lambda_{\mathrm{Zr}^{\delta+}}^{\mathrm{eff}} \cdot \cos\theta} \right) \cdot \left[1 - \exp\left(\dfrac{-d_\mathrm{t}}{\lambda_{\mathrm{Zr}^{\delta+}}^{\mathrm{eff}} \cdot \cos\theta} \right) \right]}{C_{\mathrm{Zr}^{\delta+}}^{\mathrm{b}} \cdot \left[1 - \exp\left(\dfrac{-d_\mathrm{b}}{\lambda_{\mathrm{Zr}^{\delta+}}^{\mathrm{eff}} \cdot \cos\theta} \right) \right]} \tag{4.A4c}$$

Chapter 5

The mechanism of low-temperature oxidation of zirconium

L.P.H. Jeurgens, A. Lyapin, E.J. Mittemeijer

Abstract

The mechanism of initial oxide-film growth on a bare Zr substrate was investigated by modelling the kinetics of oxide-film growth as a function of oxidation time, temperature and partial oxygen pressure (pO_2). To this end, the coupled currents of cations and electrons (by both tunnelling and thermionic emission) through a homogeneous surface-charge field were considered. The calculated growth curves are in very good agreement with the experimental growth curves for the initial, thermal oxidation of Zr within the temperature and pO_2 ranges of 304 – 573 K and 1.3×10^{-6} – 1.3×10^{-4} Pa, respectively. It follows that, for all cases studied, the oxide-film growth rate is limited by the field-assisted cation migration into or through the developing oxide film. Up to oxide-film thicknesses in the range of 2 to 3 nm, a constant value for the kinetic potential (practically equal to the Mott potential) is sustained during growth by the relatively fast forward and reverse electron tunnelling currents across the developing oxide film. Beyond this critical thickness, as only reached for elevated oxidation temperatures (> 473 K), the net electron flux by tunnelling drops to zero and the electron transport by thermionic emission becomes rate-*determining* for the oxide-film growth, while the cation transport remains rate-*limiting*. Observed changes of the rate-determining energy barrier for cation motion, as well as of the metal-oxide and oxide-oxygen work functions, with temperature and pO_2 are related to the gradual transformation of the initially amorphous, overall non-stoichiometric oxide film into crystalline ZrO_2.

5.1. Introduction

The initial formation and continued growth of a thin oxide film on a bare metal surface involves a series of steps: transport of oxygen molecules to the surface and their physi- and chemisorption, oxide nucleation and (lateral) growth, formation of a 'closed' oxide film covering the entire metal surface and continued oxide-film growth by transport of charged species (as, possibly, cations, anions, electrons, holes and vacancies) through the developing oxide film towards the oxide-gas interface (surface) and/or the metal-oxide interface. If transport of one of the charged species occurs intrinsically at a relative fast rate, then an electrostatic field develops within the growing oxide film, such that the transport of the intrinsically less mobile (i.e. rate-*limiting*) charged species is enhanced. Consequently, the transport of the charged species is determined by the gradients of both the chemical (related to the concentration) and electrostatic potentials in the developing oxide film (Refs. [1, 49, 74]).

Clearly, a comprehensive theoretical treatment of the oxidation process should incorporate at least one electronic and one ionic current in a so-called coupled-currents concept. This is the point of departure for the model put forward by Fromhold and Cook for the oxidation of metals at low temperatures (i.e. up to, say, about 600 K) [1, 23, 24]. This model is based on the currents of ions (either cations or anions) and electrons, which are coupled by the constraint that no net electric charge is transported through the film. Until now this so-called coupled-currents (CC) model has been applied to experimental data for only a few cases: the initial oxidation of Fe and/or Fe-nitride [49, 74, 75, 77] and Mg [78]. For many metals (including Zr) no consensus has been reached on the rate-limiting step(s) and mechanism(s) governing the oxide-film growth rate on the bare metal surface for different temperature ranges, partial oxygen pressures and film-thickness regimes. Such studies have only been rarely performed up to now (see above), because of the lack of reliable quantitative data on the growth kinetics for the initial oxidation stage. Therefore, it is worthwhile to find out if the coupled-currents approach can explain the kinetic aspects of the initial stages of oxidation of metals in general.

In two recent contributions by the present authors [64, 79], a novel, methodological approach by combining *angle-resolved* X-ray photoelectron spectroscopy and in situ, multi-wavelength ellipsometry was applied to establish the growth kinetics, chemical composition and constitution of the initial oxide films grown on bare, polycrystalline Zr substrates by thermal oxidation within the temperature and partial oxygen pressure ranges (pO_2) of 304 – 773 K and 1.3×10^{-6} – 1.3×10^{-4} Pa, respectively. It was shown that the oxidation of a bare, polycrystalline Zr substrate proceeds by an initial regime of very fast oxide-film growth, followed by a second stage of much slower, but continued oxide-film growth (for temperatures > 423 K). The onset of oxidation starts with the formation and growth of a non-stoichiometric, predominantly amorphous [9, 64, 79] oxide film (with an overall O/Zr-ratio < 2) up to a certain limiting thickness (that increases with increasing temperature) [66]. The resulting overall, non-stoichiometric oxide-films exhibit gradients of Zr-enrichment and O-deficiency that decrease from the metal/oxide interface towards the oxide surface. At even higher temperatures of $T > 573$ K, oxide-film growth becomes predominated by the extensive dissolution of oxygen into the Zr substrate, which is accompanied by the partial decomposition of the developing oxide film [64, 79].

In the present work, the previously established oxide-film growth kinetics [64, 79] within the temperature and pO_2 ranges of 304 – 573 K and 1.3×10^{-6} – 1.3×10^{-4} Pa (for which the dissolution of oxygen into the Zr substrate can be neglected; see Ref. [79]), are quantitatively described with the coupled-currents model in order to determine the rate-limiting step(s) and mechanism(s) governing the oxide-film growth rate on bare Zr metal surfaces.

5.2. Theoretical background

The coupled-currents constraint (i.e. no net electric charge transport through and no build-up of space charge within the developing oxide film) implies that

$$\sum_i q_i J_i = 0 , \tag{5.1}$$

where q_i is the charge of the i^{th} migrating species (i.e. either cations, anions or electrons), and J_i is the flux (i.e. current density) of the i^{th} species through the oxide film.

For thin oxide films (i.e. thinner than about 2 – 3 nm), free electrons from the Fermi level of the parent metal substrate can traverse the developing oxide film by quantum-mechanical tunnelling and go into the acceptor levels of oxygen molecules or atoms adsorbed onto the oxide surface (Fig. 5.1). At elevated temperatures i.e. for Zr at temperatures $T > 473$ K; see Ref. [79]), additional electron transport can be achieved by thermionic (or Schottky) emission from the Fermi level of the metal into the conduction band of the oxide. As a result, an electrostatic potential or so-called kinetic potential (further designated as V_{K}; see Refs. [1, 23, 24]) is established between the metal substrate and the chemisorbed oxygen species (presumably O_2^- and/or O^-; cf. Refs. [80]). It is assumed that a constant potential

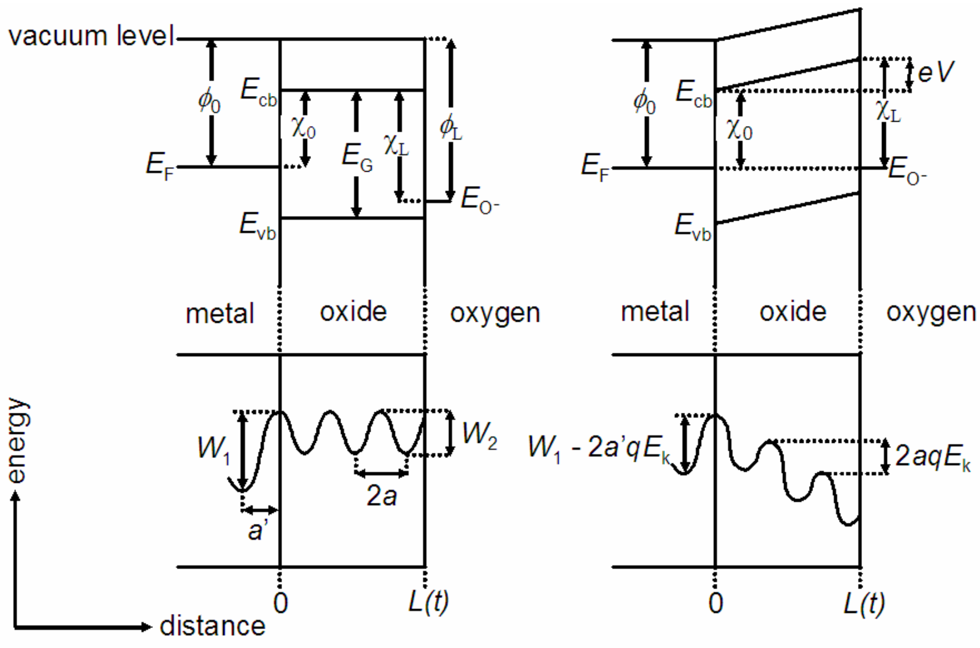

(a) before electron transfer (i.e. without field)

(b) after electron transfer (i.e. with surface-charge field)

Figure 5.1. Schematic electron energy–level diagram of a model metal/oxide/oxygen system (upper part) and potential–energy diagram for cations near the metal/oxide interface and in the atomic arrangement of the oxide (lower part): **(a)** before transport of free electrons from Fermi level (E_F) of the metal substrate towards acceptor levels (E_{O^-}) of oxygen molecules or atom adsorbed onto the oxide surface, and **(b)** when large and (nearly) equal forward and reverse electron currents occur across the developing oxide film (i.e. when electron transport occurs at a much faster rate than the intrinsic cation transport) (see Sec. 5.2). The work functions ϕ_0 (subscript designating position x=0) and ϕ_L (subscript designating position $x = L(t)$, where $L(t)$ denotes the oxide-film thickness at time t) are defined relative to the vacuum level, whereas the work functions χ_0 and χ_L are defined as an energy difference between the bottom of the conduction band and the Fermi level of metal and between the bottom of the conduction band and the O^- acceptor level, respectively. E_G is the band gap of oxide. The resulting surface-charge field with strength $E_k = -(\chi_0 - \chi_L)/L(t)$ lowers the energy barriers for the forward 'hopping' of cations between two adjacent potential minima across the metal/oxide interface (W_1) and within the oxide film (W_2) by an amount of $a'qE_k$ and aqE_k, respectively (where q is the charge of a cation, and a' and a are half the distances between adjacent potential minima across the metal/oxide interface and within the oxide, respectively). For further details, see Sec. 5.2.

gradient exists within the oxide film. The resulting uniform surface-charge field with strength $E_k = -V_k / L(t)$ (where $L(t)$ denotes the oxide-film thickness at time t) lowers the energy barriers for outward (i.e. forward) diffusion of ions into and through potential minima within the developing oxide film (these minima can presumably be associated with interstices of the oxygen sublattice of the oxide). Thus, the forward current of cations is enhanced by the built-in electric field. In the absence of the surface-charge field, the intrinsic (chemical) diffusion of ions through the oxide film due to the concentration gradient(s) would be negligibly small at the low temperatures considered here (i.e. up to 573 K).

In the *one extreme* case, when electron transport occurs at a much faster rate (e.g. due to quantum mechanical tunnelling) than the intrinsic ionic transport rate, the value of the established kinetic potential, V_k, approaches that of the so-called Mott potential, V_M , defined as (see Fig. 5.1 and Refs. [1, 23, 24, 49])

$$V_\mathrm{k} = V_\mathrm{M} = e^{-1}(\chi_0 - \chi_\mathrm{L}) , \tag{5.2a}$$

where e is the magnitude of the elementary charge, and χ_0 and χ_L are the metal-oxide work function and the oxide-oxygen work function (both taken relative to the bottom of the conduction band in the oxide), respectively (Fig. 5.1). The occurrence of the Mott potential implies that the forward and reverse electron (tunnelling) currents large and equal (see also Eq. (5.4) in Sec. 5.2.2). In practice, the Mott potential can only be reached asymptotically; the relatively small unbalance between the forward and reverse electron currents then provides the net current of ionic species required to satisfy the coupled-currents criterion. This extreme case can be considered as a realistic description of the actual growth mechanism only for oxide-film thicknesses up to about 2 – 3 nm, i.e. as long as fast electron transport by the quantum-mechanical tunnelling mechanism is possible (see Refs. [49, 62]).

In the *other extreme* case, when intrinsic electron transport occurs at a much slower rate than the intrinsic ionic transport rate, the value of the established kinetic potential, V_k, approaches that of the so-called diffusion potential, V_d, of the i^th ionic species [1,24], i.e.

$$V_\mathrm{k} = V_\mathrm{d} = \frac{k_\mathrm{B}T}{Z_i e}\ln\left[\frac{C_i(0)}{C_i(L)}\right] \tag{5.2b}$$

where k_B is the Boltzmann constant, T is the absolute temperature, Z_ie is the effective charge per particle of the ionic species transported through the lattice, $C_i(0)$ and $C_i(L)$ are the defect concentrations of the diffusing ionic species at the metal-oxide interface, $L(t) = L(0)$, and at the oxide-oxygen interface, $L(t)$, respectively). The occurrence of the ionic diffusion potential implies that the forward and reverse currents of the i^th ionic species are large and equal. In practice, the diffusion potential can only be reached asymptotically; the relatively small unbalance between the forward and reverse ion species currents then provides the net current of electrons required to satisfy the coupled-currents criterion. The value of the kinetic potential, V_k, may approach that of the ionic diffusion potential, V_d, only in exceptional cases, for oxide-film thicknesses larger than about 2 – 3 nm, when electron transport is only possible by thermionic (or Schottky) emission.[7]

For the oxide-film thickness and temperature ranges considered here (i.e. 0 – 4 nm and 304 – 573 K, respectively; cf. Figs. 5.2 and 5.3), the actual value of the kinetic potential will vary in between the two extremes V_M and V_d.

5.2.1. Ion flux

Diffusion of ions is considered as a thermally activated hopping process in which an ion moves between two adjacent potential minima (as interstices in the oxygen sublattice of the developing oxide film). The corresponding activation energy barriers across the metal-oxide interface and within the oxide film are denoted W_1 and W_2, respectively, in Fig. 5.1. It is assumed that only one of these two barriers is rate-determining, which further is called the rate-determining energy barrier W.

In the steady-state approximation, which implies that the flux is independent of the position in the oxide film, the ionic flux, J_i, under the influence of both a concentration gradient and a homogeneous electric field strength, E_k, is given by:

$$J_i = 4a\nu_i \exp\left(-\frac{W}{k_\mathrm{B}T}\right)\sinh\left(\frac{Z_\mathrm{i}eE_\mathrm{k}a}{k_\mathrm{B}T}\right)\left[\frac{C_i(L)-C_i(0)\exp\left(\frac{Z_\mathrm{i}eE_\mathrm{k}L(t)}{k_\mathrm{B}T}\right)}{1-\exp\left(\frac{Z_\mathrm{i}eE_\mathrm{k}L(t)}{k_\mathrm{B}T}\right)}\right], \tag{5.3}$$

where a is half of the ionic jump distance (taken equal to half of the average distance between two interstices within the oxygen sublattice of the oxide) and ν_i is the ionic attempt frequency for jumping over the rate-determining energy barrier W (either W_1 or W_2; see above and Fig. 5.1).

5.2.2. Electron flux due to tunnelling

At $T = 0$ K, the *net* flux (J_e^tun) of the electrons due to tunnelling through the potential energy barrier of the oxide film is given by [1, 23]:

---

[7] Note that the electron transport by thermionic (or Schottky) emission is a process that, even at high temperatures, is orders of magnitude slower than the quantum-mechanical tunnelling process.

$$J_{\mathrm{e}}^{\mathrm{tun}}=\frac{1}{8\pi^2\hbar L^2}\left[(2\chi_0+eE_{\mathrm{k}}L)\exp\left\{-\frac{2\sqrt{m}L}{\hbar}\sqrt{2\chi_0+eE_{\mathrm{k}}L}\right\}\right.\\\left.-(2\chi_{\mathrm{L}}-eE_{\mathrm{k}}L)\exp\left\{-\frac{2\sqrt{m}L}{\hbar}\sqrt{2\chi_{\mathrm{L}}-eE_{\mathrm{k}}L}\right\}\right], \tag{5.4}$$

where $\hbar = h/2\pi$ (with h as Planck's constant) and m is the effective mass of the electron. Note that whenever the electric field due to the kinetic potential V_{k} approaches the Mott potential (see Eq. (5.2a) and its discussion), the net electron tunnel current reduces to zero. A first order approximation for the relatively weak temperature dependence of J_e^{tun} (as compared to the temperature dependence of the thermionic electron flux, see Sec. 5.2.3) is given by [1, 23]:

$$\frac{J_{\mathrm{e}}^{\mathrm{tun}}(T)}{J_{\mathrm{e}}^{\mathrm{tun}}(0)}=\pi\frac{\sqrt{2m}L}{\sqrt{\chi_0}\hbar}k_{\mathrm{B}}T\bigg/\sin\left(\pi\frac{\sqrt{2m}L}{\sqrt{\chi_0}\hbar}k_{\mathrm{B}}T\right) \tag{5.5}$$

5.2.3. Electron flux due to thermal emission

The net electron flux, J_e^{therm}, due to thermal (or Schottky) emission becomes important at elevated temperatures, beyond a certain film thickness (usually around ~2 nm). It is given by [1, 24]:

$$J_{\mathrm{e}}^{\mathrm{therm}}=\mathrm{A_R}T^2\exp\left(-\frac{Q_{\max}^{\mathrm{f}}}{k_{\mathrm{B}}T}\right)-n_{\mathrm{O^-}}\nu_{\mathrm{e}}\exp\left(-\frac{Q_{\max}^{\mathrm{r}}}{k_{\mathrm{B}}T}\right) \tag{5.6a}$$

where $\mathrm{A_R}$ is the Richardson constant (= $4\pi m k_{\mathrm{B}}^2/h^3$); $n_{\mathrm{O^-}}$ is the surface density of filled $\mathrm{O^-}$ levels at $x = L(t)$ (i.e. at the oxide-oxygen interface), which is related to the surface-charge field strength via: $E_{\mathrm{k}} = e\cdot n_{\mathrm{O^-}}/\varepsilon$ (with ε as the dielectric constant of the oxide film); ν_e is the electron jump frequency into the filled $\mathrm{O^-}$ level; and $Q_{\max}^{\mathrm{f}}$ and $Q_{\max}^{\mathrm{r}}$ are the are the maximum potential energy barrier in the forward and reverse directions (as measured with respect to the Fermi level of the metal), respectively. The energy barrier heights Q^{f} and Q^{r} in the forward and reverse direction depend on the position x within the oxide film according to [1, 24]:

$$Q^{\mathrm{f}}(x)=\chi_0+eE_{\mathrm{k}}\mathrm{x}-\frac{e^2}{16\pi\varepsilon}\cdot\frac{1}{x}-\frac{2\pi e^2\gamma\sigma}{\left(4\pi(\varepsilon+\varepsilon_{\mathrm{ads}})\right)^2}\cdot\frac{1}{(L-x)^2} \tag{5.6b}$$

and

$$Q^{\mathrm{r}}(x) = \chi_{\mathrm{L}} - eE_{\mathrm{k}}(L-x) - \frac{e^2}{16\pi\varepsilon}\cdot\frac{1}{x} - \frac{2\pi e^2\gamma\sigma}{\left(4\pi(\varepsilon+\varepsilon_{\mathrm{ads}})\right)^2}\cdot\frac{1}{(L-x)^2}, \tag{5.6c}$$

respectively. Here, σ is the surface density of physically adsorbed neutral oxygen molecules, γ is the molecular polarizability of an adsorbed oxygen molecule [24, 81] and $\varepsilon_{\mathrm{ads}}$ is the dielectric constant of the adsorbed oxygen layer (which approximately equals the vacuum permittivity ε_0 for low surface density σ). The maximum energy barrier heights $Q^{\mathrm{f}}_{\mathrm{max}} = Q^{\mathrm{f}}(x_{\mathrm{max}})$ and $Q^{\mathrm{r}}_{\mathrm{max}} = Q^{\mathrm{r}}(x_{\mathrm{max}})$ in Eq. (5.6a) are obtained from Eqs. (5.6b) and (5.6c) for $x = x_{\mathrm{max}}$, with the position of the barrier maximum at $x = x_{\mathrm{max}}$ calculated from

$$\frac{dQ^{\mathrm{f}}}{dx} = \frac{dQ^{\mathrm{r}}}{dx} = 0. \tag{5.6d}$$

5.3. Numerical procedure

The continued growth of relatively thick, polycrystalline ZrO_2 layers on Zr substrates at relatively high temperatures (i.e. $T > 800$ K) is generally dominated by the inward diffusion of oxygen anions under influence of electro-chemical potential gradients across the developing oxide layer (cf. Refs. [82, 83]). In this case, grain boundaries in the oxide layer act as fast paths for the inward diffusion of oxygen. However, at relative low oxidation temperatures (up to about 573 K), the initial oxide film grown on the Zr substrate is predominantly amorphous [9, 64, 79]. Then (i.e. in the absence of grain boundaries in the developing oxide film and at relatively low temperatures), the metal cations are generally considered to be mobile and the oxygen anions to be immobile (cf. Ref. [21]). This assertion is supported by the observation [64, 79] that continued oxide-film growth on a Zr substrate at low temperatures is realised by the overgrowth of stoichiometric ZrO_2 on top of an initial, relatively Zr-enriched oxide film, implying that outward cation diffusion contributes considerably to the growth process. Against the above background, in this work the oxidation of the Zr substrates in the low-temperature regime of 373 – 573 K is modelled by adopting a coupled-current description for the transport of zirconium cations and electrons (by both tunnelling and thermionic emission) through a homogeneous surface-charge field within the developing oxide film (the basis of this approach has been given in Sec. 5.2).

To calculate the theoretical growth curves (i.e. the oxide-film thickness, L_{calc}, as a function of oxidation time t), first the values for the surface-charge field strength, E_{k}, were determined by imposing the coupled-currents condition of Eq. (5.1) to the currents $J_{\mathrm{Zr}^{4+}}$, J_e^{tun}

and J_e^{therm} as given by Eqs. (5.3) – (5.6) (after choosing the fit parameters (see below) and adopting appropriate values for the other parameter as given in Table 5.1). Next, the values for the surface charge field strength were substituted into the cation current equation (i.e. Eq. (5.3)) to obtain subsequently the corresponding growth rates according to

$$\frac{\partial L_{\text{calc}}}{\partial t} = R_{\text{Zr}^{4+}} J_{\text{Zr}^{4+}} , \tag{5.7}$$

where $J_{\text{Zr}^{4+}}$ is the flux of Zr^{4+} cations (see Eq. (5.3)) and $R_{\text{Zr}^{4+}}$ denotes the volume of oxide formed per Zr^{4+} cation (see Table 5.1). The theoretical growth curves (i.e. the film thickness as a function of time) were obtained by numerical integration of the growth expression of Eq. (5.7) using a fourth order Runge-Kutta scheme (cf. p. 312 of Ref. [1]), taking an initial experimental oxide-film thickness as a starting value (here 0.5 nm, see discussion below).

Fitting of the calculated to the experimental thickness-versus-time data was performed by minimising of the sum of squared differences between the calculated and experimental growth-curves data for a series of selected, monotonically increasing experimental oxide-film thickness values (as determined using in situ ellipsometry; see Ref. [79]), while varying one or more parameters (using the Nelder-Mead simplex method as implemented in Matlab [84]). It is noted that, for the above described and here applied numerical procedure, the sensitivity of the fitting to the steep gradients in the first part of the experimental oxide-film growth curves (cf. Figs 5.2a and 5.3a) is considerably improved as compared to the numerical procedure applied in Refs. [49, 74, 78] (for which a numerical integration of the growth expression of Eq. (5.7) is not performed; the fitting is simply done by minimisation of the difference between selected experimental and calculated time (instead of thickness) data, see Refs. [49, 74, 78] for details).

A systematic parameter study performed for the experimental growth curves studied here (cf. Fig. 5.2) indicated that the energy barrier for cation transport, W, and especially energy barriers for electron transport, χ_0 and χ_{L}, are the most sensitive fit parameters (out of a large number of parameters in Eqs. (5.2) – (5.7)), in agreement with the finding in Refs. [49, 74]. Therefore, the values of W, χ_0 and χ_{L} were taken as fit parameters in the current fitting procedure (adopting appropriate values for the remaining parameters in Eqs (5.2) – (5.7); see Table 5.1).

At the onset of oxidation, as well as during the first part of the very fast initial growth regime, (*i*) a continuous, closed oxide film presumably has not yet been formed,

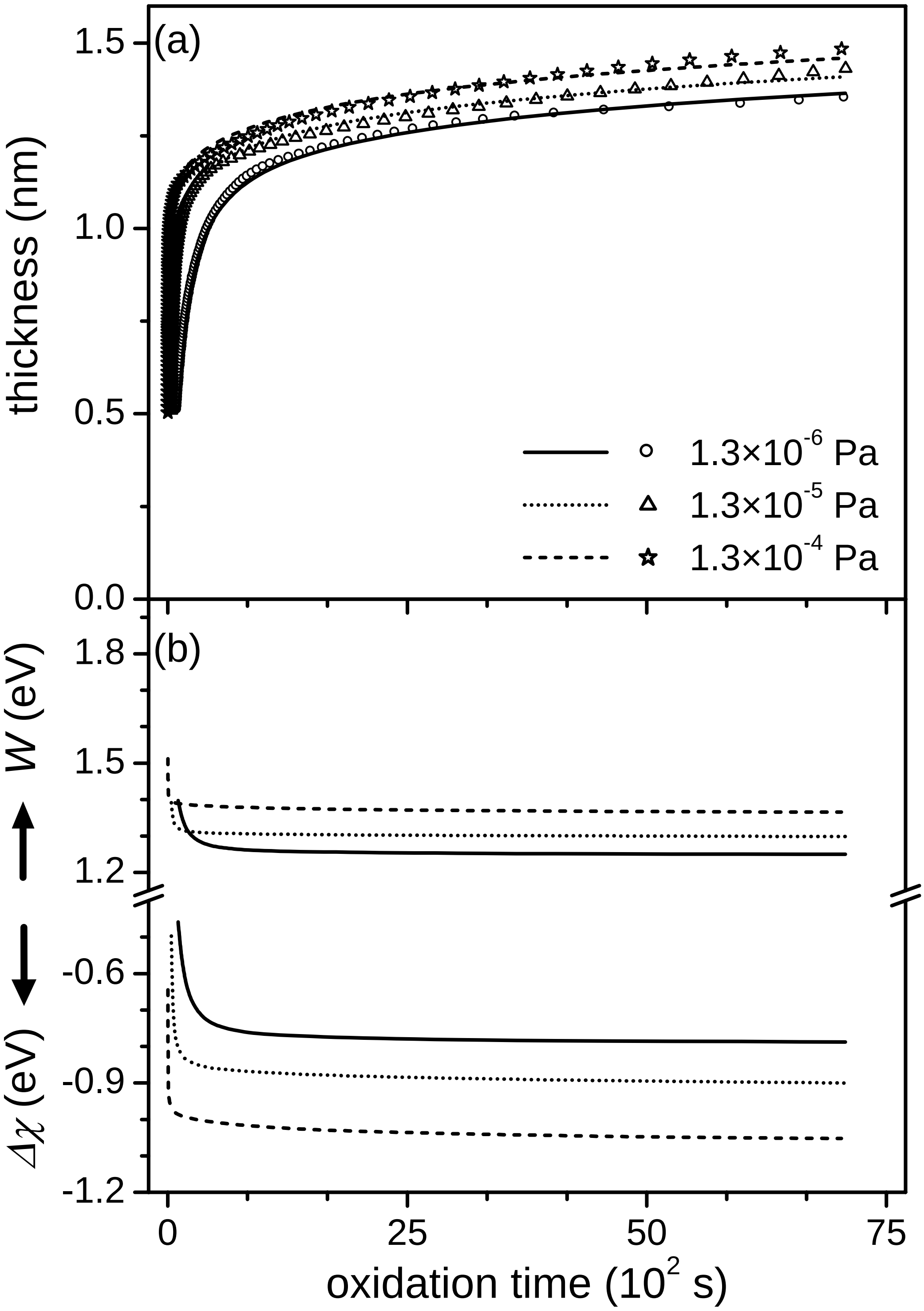

Figure 5.2. (a) Fitted (*lines*) and experimental (*markers*) oxide-film growth curves and **(b)** the corresponding energy barrier for cation transport (W) and the work function difference ($\Delta\chi = \chi_0 - \chi_L$), for the oxidation of a bare Zr substrate at T = 304 K and various pO$_2$'s. The experimental data have been obtained using in situ, multi-wavelength ellipsometry [79]; the calculated growth curves have been obtained using the procedure described in Sec. 5.4.

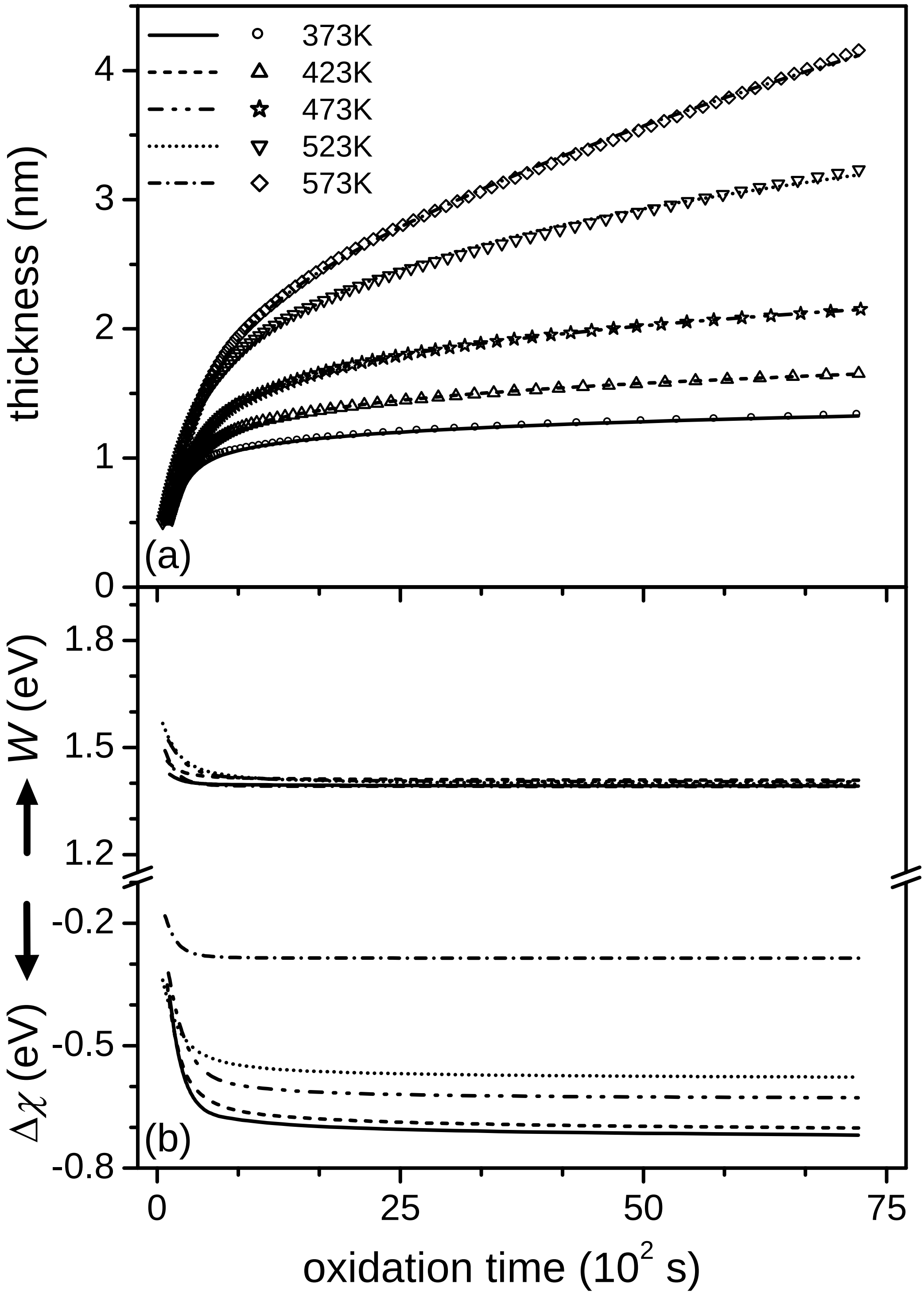

Figure 5.3. **(a)** Fitted (*lines*) and experimental (*markers*) oxide-film growth curves and **(b)** the corresponding energy barrier for cation transport (W) and the work function difference ($\Delta\chi=\chi_0-\chi_L$), for the oxidation of a bare Zr substrate at pO_2 = 2×10^{-6} Pa and various oxidation temperatures. The experimental data have been obtained using in situ, multi-wavelength ellipsometry [79]; the calculated growth curves have been obtained using the procedure described in Sec. 5.4.

Table 5.1. Values for the physical and chemical constants used in the numerical computations (see Eqs. (5.2) – (5.8)).

Symbol	Value	Units	References
$2a$	0.4	nm	
$\nu_{\mathrm{Zr}^{4+}}$	10^{12}	s^{-1}	[23, 24]
ν_{e}	10^{14}	s^{-1}	[23, 24]
$Z_{\mathrm{Zr}^{4+}}$	4		
$C_{\mathrm{Zr}}(0)$	0.01	nm^{-3}	[23, 24]
$C_{\mathrm{Zr}}(L)$	0.0001	nm^{-3}	[23, 24]
$R_{\mathrm{Zr}^{4+}}$	0.036	nm^{3}	
$\varepsilon_{\mathrm{r}} = \varepsilon / \varepsilon_0$	3.77		as obtained from ellipsometry [64, 79]
$\gamma \cdot \sigma$	10^{-20}	$\mathrm{J}^{-1}\mathrm{C}^{2}$	[23, 81]

(*ii*) interfacial reactions (instead of transport into or through the oxide film) may be rate-limiting for the oxidation, and (*iii*) changes in the metal-oxide work function may occur as a result of e.g. the initial incorporation of oxygen into the subsurface of the parent metal substrate (cf. Refs. [3, 49-51, 74, 75, 62]). Consequently, the interfacial defect concentrations of the diffusing ionic species (i.e. $C_i(0)$ and $C_i(L)$), the density of acceptor levels (as provided by oxygen molecules adsorbed onto the surface) and/or the metal-oxide and oxide-oxygen work functions may depend on the oxide-film thickness, $L(t)$, during the very initial stage of oxide-film growth. To exclude the effect of a non-closed oxide film, thickness values below 0.5 nm (for which a closed oxide film presumably has not yet been formed) are not considered in the current fitting procedure (as also in Refs. [49, 74, 78]). To allow a flexible description of the initial part of the growth curve, a sigmoidal thickness-dependence of the fitting parameters W, χ_0 and χ_{L} has been taken, i.e.

$$W(L) = \frac{W^{\mathrm{i}} - W^{\mathrm{f}}}{1 + e^{(L-L_0)/\beta}} + W^{\mathrm{f}}, \tag{5.8a}$$

$$\chi_0(L) = \frac{\chi_0^{\mathrm{i}} - \chi_0^{\mathrm{f}}}{1 + e^{(L-L_0)/\beta}} + \chi_0^{\mathrm{f}}, \tag{5.8b}$$

and

$$\chi_{\mathrm{L}}(L) = \frac{\chi_{\mathrm{L}}^{\mathrm{i}} - \chi_{\mathrm{L}}^{\mathrm{f}}}{1 + e^{(L-L_0)/\beta}} + \chi_{\mathrm{L}}^{\mathrm{f}}, \tag{5.8c}$$

This implies that the value of, for example, the energy barrier *W* can maximally change W^{i} to W^{f} around the central thickness value L_0 with a rate defined by β (cf. Fig. 5.2b). It is noted that, in the current investigation, $W = W^{\mathrm{i}}$ always occurs at a hypothetically *L* value < 0; $W = W^{\mathrm{f}}$ does occur in reality if *L* is sufficiently large as compared to L_0. By adopting this functional description for the thickness dependence of the fit parameters *W*, χ_0 and χ_{L}, the number of fitting coefficients in the fitting procedure remains limited. Taking the same values of L_0 and β for Eqs. 5.8(a)-(c), a total of 8 fitting parameters occur: L_0, β, W^{i}, W^{f}, χ_0^{i}, χ_0^{f}, $\chi_{\mathrm{L}}^{\mathrm{i}}$ and $\chi_{\mathrm{L}}^{\mathrm{f}}$. Thereby the robustness of the fitting procedure is greatly improved as compared to the case where independent values of *W*, χ_0 and/or χ_{L} are fitted for each selected time value (as done in e.g. Refs. [49, 74, 78]), or for selected thickness values.

5.4. Experiment versus model predictions

Using the procedure as described in Sec. 5.3 and taking *W*, χ_0 and χ_{L} as thickness-dependent fit parameters, the model as described in Section 5.2 is fitted to the experimental growth curves at various temperatures (304 – 573 K) and partial oxygen pressures (1.3×10^{-6} – 1.3×10^{-4} Pa), as obtained from in situ multi-wavelength ellipsometry [79]. The fitted growth curves are represented by the lines in Figs. 5.2a and 5.3a; the experimental oxide-film thickness data are represented by the open markers. The energy barrier *W* and the work function difference $\Delta\chi = (\chi_0 - \chi_{\mathrm{L}})$, as results from the fitting, have been plotted as a function of time in Figs. 5.2b and 5.3b. The work function difference $\Delta\chi$ is shown, rather than the individual work functions χ_0 and χ_{L}, because for oxidation temperatures up to 473 K (where the contribution of thermionic emission to the electron transport is negligible), the theoretical growth curves are sensitive to $\Delta\chi$ rather than to the individual values of χ_0 and χ_{L} (see Eq. (5.4); see also Refs. [49, 74]).

Clearly, for all pO_2's and temperatures studied, a very good agreement exists between the fitted and experimental growth curves. Hence, within the studied temperature (304 – 573 K) and pO_2 (1.3×10^{-6} – 1.3×10^{-4} Pa) ranges, the thermal oxidation of a bare Zr substrate can be accurately described by adopting a coupled-currents description of zirconium cations and electrons (by both tunnelling and thermionic emission) in a homogeneous surface-charge field. Further, it follows that the values of W and $\Delta\chi=(\chi_0-\chi_\mathrm{L})$ are approximately constant for the main part of the oxide-film growth curves (being equal to W^f and $\Delta\chi^\mathrm{f}=(\chi_0^\mathrm{f}-\chi_\mathrm{L}^\mathrm{f})$, respectively; see Eqs. 5.8(a) – (c)). This implies that, only for the initial part of the oxide-film growth curves (see Figs. 5.2b and 5.3b), a thickness-dependence of W and especially $\Delta\chi=(\chi_0-\chi_\mathrm{L})$ is required to accurately describe the initial steep gradient of the growth curves at the onset of oxidation (as discussed in Sec. 5.3).

For all pO_2's and temperatures studied, a negative kinetic potential, V_k, (corresponding with a positive electric field strength, $E_\mathrm{M} = -V_\mathrm{M}/L$) is maintained over the entire thickness range concerned. This implies that, in this study, the oxide-film growth rate is always *limited* by cation transport into or through the developing oxide film; electron transport across the oxide film may co-*determine* the growth rate (if the kinetic potential deviates from the Mott potential; see Sec. 5.2 and discussion below). For oxide-film thicknesses up to 2 to 3 nm (somewhat increasing with increasing T), the kinetic potential is approximately equal to the Mott potential. This implies that, up to this critical thickness, electron tunnelling transport occurs at a much faster rate than the intrinsic ionic transport (with large and nearly equal forward and reverse electron tunnelling currents; see Eq. (5.2a) and its discussion).

Due to the very fast increase of the oxide-film thickness in the initial stage of oxidation, the electric-field-assisted motion of cations into and through the developing oxide film becomes already strongly reduced during the initial growth regime (because the electric field strength due to the approximate Mott potential, i.e. $E_\mathrm{M} = -V_\mathrm{M}/L(t)$, decreases with increasing thickness). For oxide-film thicknesses larger than this critical oxide-film thickness (and only for the elevated temperatures of 523 and 573 K; see Fig. 5.3a), after net electronic current by tunnelling has dropped to zero, the much slower electron transport by thermionic emission remains (see inset of Fig. 5.4); a process that is independent of the oxide-film thickness; see Eq. (5.6a). Then the value of the kinetic potential, initially approximately equal to the Mott potential, becomes less negative. This implies that, from this point onwards, electron transport by thermionic emission across the developing oxide film becomes co-*determining* the growth rate, while cation transport remains rate-*limiting*.

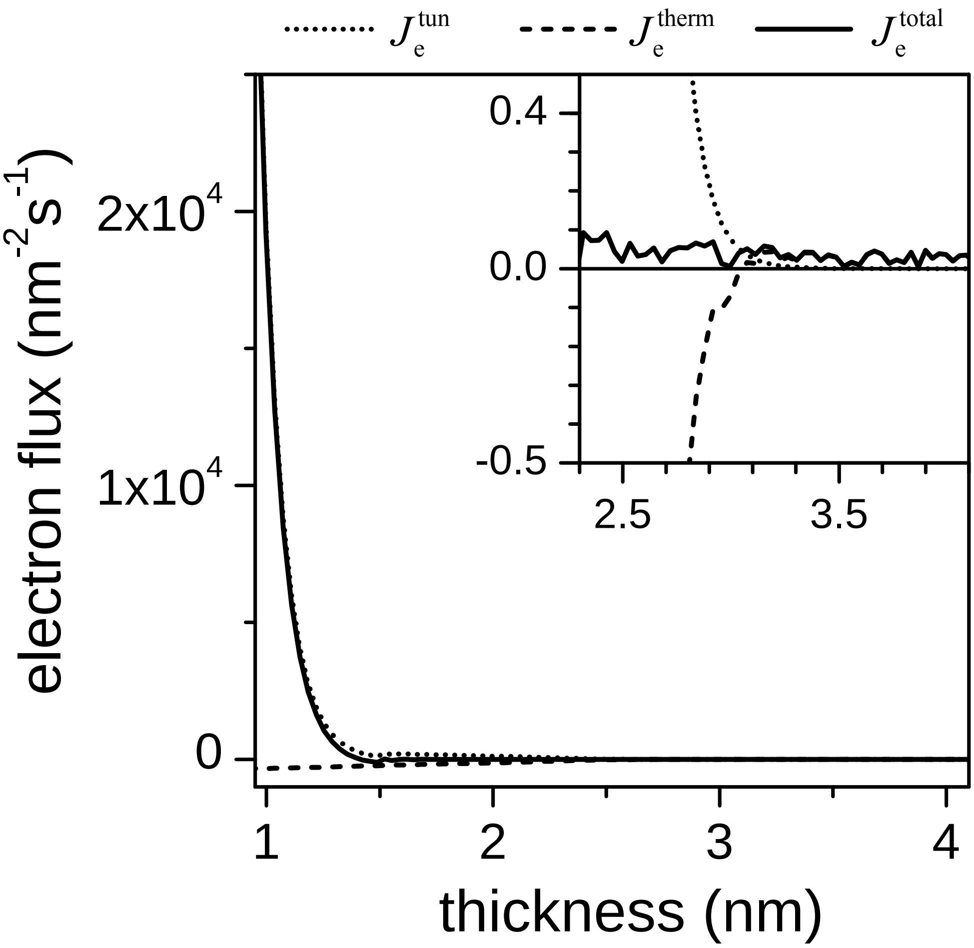

Figure 5.4. Net electron fluxes due to tunnelling, J_e^{tun}, and thermal emission, J_e^{therm}, as well as the (net) total electron flux, $J_e^{total} = J_e^{tun} + J_e^{therm}$, as a function of oxide-film thickness corresponding to the fitted oxide-film growth curve calculated for the oxidation of the bare Zr substrate at $pO_2 = 2\times10^{-6}$ Pa and T = 573 K. The inset shows an enlargement of the electron fluxes for the narrow oxide-film thickness range, in which the net electron tunnelling current approaches zero, and thermionic electron emission becomes the dominating mechanism for electron transport. Note that up to an oxide-film thickness of about 3 nm, the net electron flux by thermal emission is of sign opposite to that of the corresponding tunnel flux. The thermionic electron flux changes sign (becomes positive) as soon as the flux due to electron tunnelling approaches zero.

The values of W^f, χ_0^f, χ_L^f (as obtained during the slow growth stage) are plotted as a function of the pO_2 for the oxidation at 304 K, and as a function of the oxidation temperature at $pO_2 = 2\times10^{-6}$ Pa, in Figs. 5.5a and 5.5b, respectively. It follows that the rate-determining energy barrier for ion motion, W^f, increases with increasing pO_2 for the oxidation at room temperature (Fig. 5.5a), as well as with increasing temperature at $pO_2 = 2\times10^{-6}$ Pa (Fig. 5.5b).

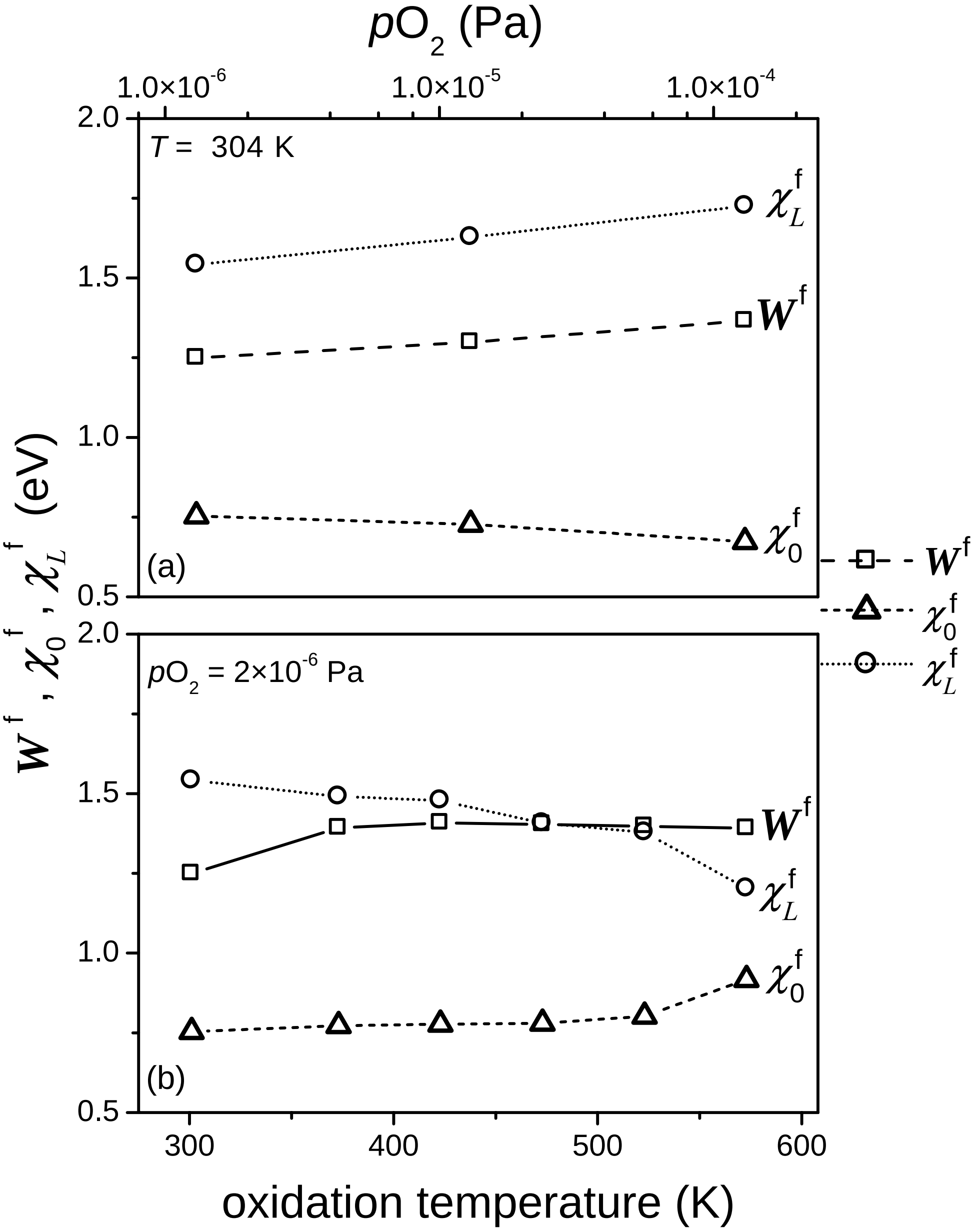

Figure 5.5. The values of the energy barrier for cation transport, W^{f}, the metal-oxide work function, χ_0^{f}, the oxide-oxygen work function, $\chi_{\mathrm{L}}^{\mathrm{f}}$ (all pertaining to the slow, growth stage; see Sec. 5.3 and Eq. (5.8)), as a function of **(a)** the $p\mathrm{O}_2$ at T = 304 K and **(b)** the oxidation temperature at $p\mathrm{O}_2 = 2\times10^{-6}$ Pa, corresponding to the oxide-film growth curves of Figs. 5.2a and 5.3a.

An increase of the energy barrier W with increasing temperature has also been reported for the thermal oxidation of iron [74] and iron nitrides [49], and is accompanied with changes in the composition and the microstructure of the developing oxide film. Thus, in the present work, the observed increase of W^{f} with both temperature and $p\mathrm{O}_2$ is attributed to the gradual transformation of the initially amorphous, overall non-stoichiometric oxide film into a crystalline oxide film mainly constituted of crystalline ZrO_2 (see Refs. [64, 79]).

The slight increase of the absolute work function difference $\left|\Delta\chi^{\mathrm{f}}\right|=\left|\chi_{0}^{\mathrm{f}}-\chi_{\mathrm{L}}^{\mathrm{f}}\right|$ with increasing pO_2 for the oxidation at room temperature (Fig. 5.5a) implies a gradual increase of the (absolute) value of the Mott potential sustained during the (initial stage of) oxide-film growth (see above). At room temperature and for the relatively low pO_2's considered, the coverage of the surface with physisorbed oxygen (and thus the density of electron acceptor levels for the built-up of the surface-charge field; see Fig. 5.1) will be directly proportional to the pO_2 [3]. An increase in the density of electron acceptor levels is accompanied with an increase of the density of chemisorbed, negatively charged oxygen species on the oxide surface [3]. Consequently, the absolute value of the Mott potential increases with increasing pO_2 for the oxidation at room temperature, as manifested in the current model by an increase of $\left|\Delta\chi^{\mathrm{f}}\right|$ (cf. Eq. (5.2a)).

Except for the highest oxidation temperature studied here (i.e. 573 K), the absolute work function difference $\left|\Delta\chi^{\mathrm{f}}\right|$ almost linearly decreases with increasing of temperature as a result of an *increase* of the metal-oxide work function (χ_{0}^{f}) in combination with a *decrease* of the oxide-oxygen work function ($\chi_{\mathrm{L}}^{\mathrm{f}}$) (see Fig. 5.5b). Post-annealing of thermally grown oxide tunnel barriers led to an increase of the electron tunnelling barrier height, i.e. χ_{0}^{f} (cf. Ref. [85]). Both observations suggest that the observed increase of χ_{0}^{f} is associated with a change in the oxide-film microstructure, such as the development of long range order in the dense-random-packing-of-spheres network of oxygen ions of the initial amorphous oxide upon its gradual transformation into a crystalline oxide [86].

5.5. Conclusions

The thermal oxidation of a bare Zr substrate within the temperature (304 – 573 K) and pO_2 (1.3×10^{-6} – 1.3×10^{-4} Pa) ranges can be described adopting a coupled-currents constraint for the fluxes of zirconium cations and electrons (by both tunnelling and thermionic emission) in a homogeneous surface-charge field comprising the growing oxide film, taking the rate-determining activation energy for cation motion, and the metal-oxide and oxide-oxygen work functions, as fit parameters.

For all pO_2's and temperatures studied, the oxide-film growth rate is limited by the electric-field controlled migration of Zr cations into or through the developing oxide film. For oxide-film thicknesses up to 2 to 3 nm (somewhat dependent on temperature), electron tunnelling transport occurs at a much faster rate than the intrinsic ionic transport (with large and nearly equal forward and reverse electron tunnelling currents). Then, the kinetic potential is approximately equal to the Mott potential. For thicknesses larger than this critical oxide-film thickness (and only for relatively elevated temperatures of $T \geq 523$ K), the net electronic current by tunnelling drops to zero, and the much slower electron transport by thermionic emission remains. Then, this electron transport by thermionic emission across the developing oxide film co-*determines* the growth rate, while the cation transport remains rate-*limiting*.

The increase of the rate-determining activation energy for cation motion, W^{f}, as well as the increase of the metal-oxide work function (χ_0^{f}) in combination with a decrease of the oxide-oxygen work function ($\chi_{\mathrm{L}}^{\mathrm{f}}$), with both increasing temperature and increasing pO_2 (for the slow growth stage) are attributed to the gradual transformation of the initially amorphous, overall non-stoichiometric oxide film into a crystalline oxide film mainly constituted of crystalline ZrO_2.

Chapter 6

Summary: The initial stages of the oxidation of zirconium

Thin zirconium-oxide films (< 10 nm) are of great technological importance for many application areas such as catalysis, microelectronics, surface coatings, because of their specific physical and chemical properties (e.g. high corrosion resistance, good thermal and mechanical stability, high dielectric constant, large band gap). In order to tailor the properties of such thin oxide films, as produced by e.g. thermal oxidation of bare Zr substrates, comprehensive knowledge is required on the oxidation process, i.e. on the growth mechanism(s) and the developing microstructure (i.e. morphology, crystallographic structure, chemical composition) as a function of the oxidation conditions.

In this study, the initial oxidation of bare polycrystalline Zr substrates has been investigated using angle-resolved X-ray photoelectron spectroscopy (AR-XPS) and in situ, multi-wavelength ellipsometry for various oxidation conditions (i.e. oxidation time, partial oxygen pressure and temperature). All oxidation experiments were performed under controlled conditions in a UHV reaction chamber (RC; base pressure < 2.5×10^{-8} Pa), which is equipped with a multi-wavelength ellipsometer for in situ determination of the oxide-film growth kinetics. This chamber for thin oxide-film growth is directly coupled to the UHV chamber (base pressure < 5×10^{-8} Pa) for AR-XPS analysis. Due to its high reactivity with the ambient, the polycrystalline Zr substrates are always covered with a native oxide film (several nanometers thick) upon introduction into UHV. Therefore, the zirconium substrates were sputter-cleaned with 3 kV Ar^+ ions prior to their oxidation (further designated as *bare* substrate). Subsequently, the samples were oxidized in pure O_2 gas at various temperatures (T) and partial oxygen pressures (pO_2) within the ranges of 300 – 773 K and 1.3×10^{-7} – 1.3×10^{-4} Pa, respectively.

AR-XPS was applied to determine the thickness, constitution, and chemical composition of the grown oxide films. For the quantitative analysis of the measured XPS spectra, a correct description of the individual backgrounds of inelastic scattered electrons associated with each photoelectron line is required. To this end, a novel procedure for the reconstruction of the different spectral contributions to the measured XPS spectra has been developed, which is based on the convolution of physically realistic functions for the X-ray energy distribution, the core-level main peak, the cross-sections for intrinsic and extrinsic excitations and instrumental broadening (Chapter 2). Surface effects have been accounted for by describing the material as a bulk substrate covered with a thin surface layer of the same material, but with different intrinsic and extrinsic photoelectron-excitation properties. Reconstruction of the measured Zr 3*d* XPS spectra recorded from Zr metal and ZrO_2 (see Figs. 6.1a and 6.1b, respectively) showed that, respectively, about 28% and 21% of the total intrinsic photoelectron intensity (i.e. as required in the quantification) is not contained in the main peaks, but in the associated surface and bulk plasmon peaks. This reconstruction method has been further adapted and applied to the measured Zr 3*d* XPS spectra recorded from the oxidized Zr substrates (i.e. Zr metal covered by a thin film of zirconium oxide). The thus obtained total primary zero loss (PZL) intensities of the resolved metallic and oxidic components have been used to determine the chemical composition (i.e. O/Zr-ratio), constitution and thickness of the grown oxide-films (Chapters 3 and 4).

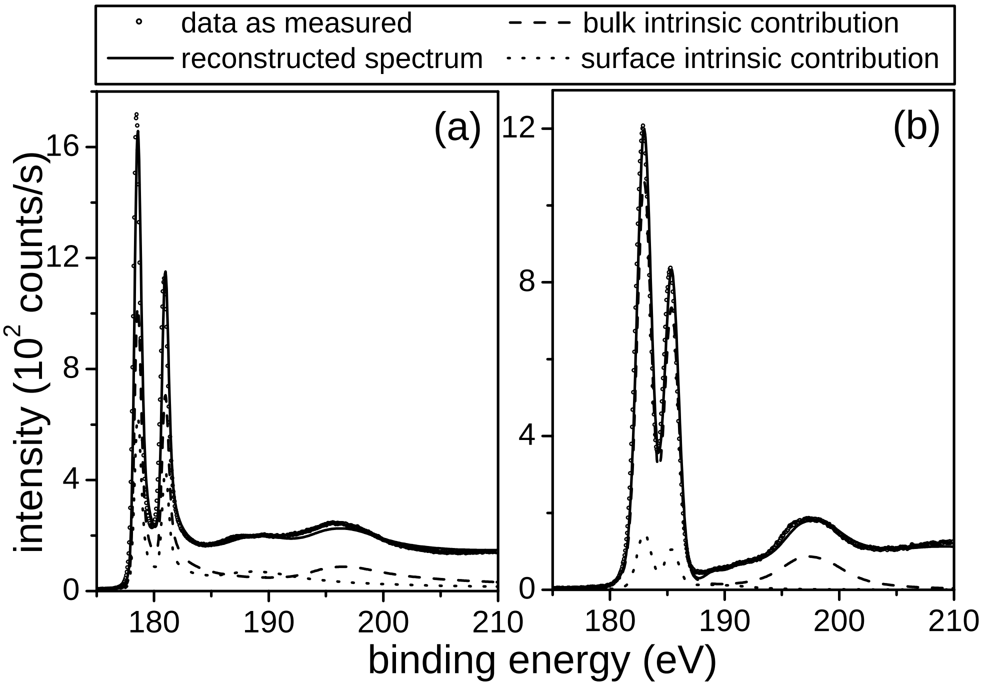

Figure 6.1. The experimental and calculated (i.e. reconstructed) Zr 3*d* XPS spectra of **(a)** zirconium metal and **(b)** zirconium oxide.

In situ, multi-wavelength ellipsometry was applied to determine the oxide-film growth kinetics, as well as the optical properties of the zirconium metal substrate and the Zr-oxide film. To this end, a model for the substrate-film system was constructed, which describes the measured changes in the ellipsometric parameters, Ψ and Δ, as a function of oxidation time over the wavelength range from 300 to 700 nm. The measured ellipsometric data could only be accurately fitted by adopting a model that incorporates a Zr substrate covered with a double-layered oxide structure (see Fig. 6.2b), consisting of a bottom layer of non-stoichiometric Zr-oxide and a (surface adjacent) top layer of stoichiometric ZrO_2 (Chapters 3 and 4). The effective-depth distributions and individual sublayer thicknesses of the non-stoichiometric and stoichiometric oxide species within the developing oxide film, as established with ellipsometry, are in good agreement with the corresponding results as determined *independently* with AR-XPS (see below).

Application of the aforementioned techniques, and employing the appropriate methods in the quantification, led to the following results for the initial oxidation of bare, polycrystalline Zr substrates.

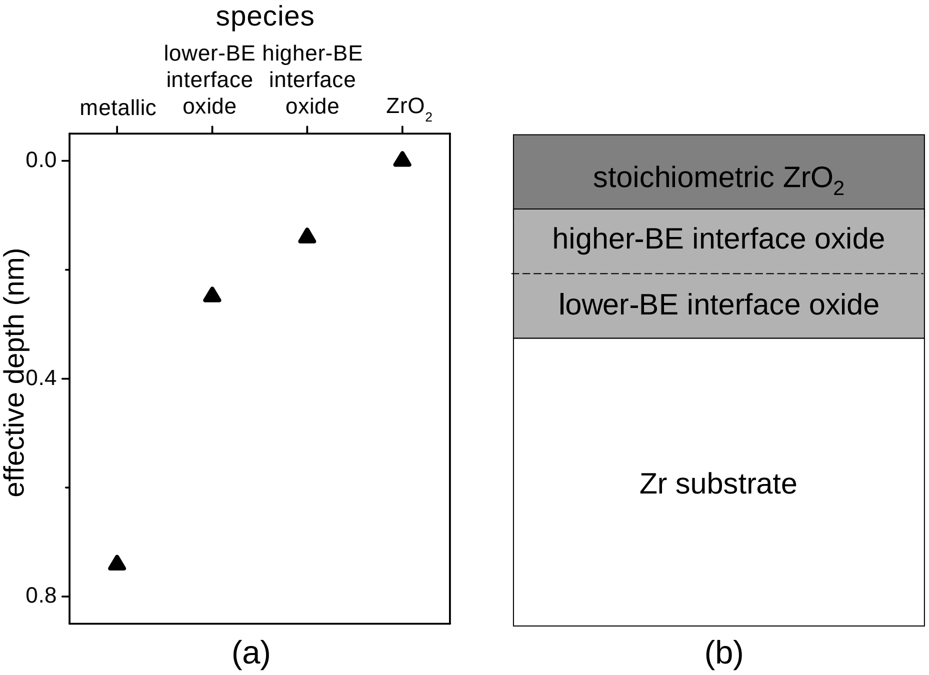

Figure 6.2. The constitution of a zirconium oxide film grown on the top of zirconium substrate by dry, thermal oxidation: **(a)** effective depth plot of the Zr substrate after oxidation for 7200 s at $T = 304$ K and $pO_2 = 1.3\times10^{-5}$ Pa; **(b)** schematic representation of the oxide-film constitution, as evidenced from AR-XPS and in situ ellipsometry.

Detailed analysis of measured Zr 3*d* XPS spectra of the oxidized Zr substrates showed the presence of *three* different chemical species in the oxide film (see Fig. 6.2): one oxidic and two weaker suboxidic components (designated as ZrO_2, lower-BE and higher-BE interface-oxide component, respectively). As evidenced from the analysis of the measured AR-XPS spectra by reconstruction of an effective depth plot (which provides a direct indication of the effective depth of a given chemical species below the oxide-film surface; see Fig. 6.2a), the stoichiometric ZrO_2 species is located at the outer oxide surface, whereas both interface-oxide components are positioned at depths in between those of the Zr substrate and the outer surface region of stoichiometric ZrO_2: the interface-oxide species with the lower BE value is located closer to the Zr substrate than the higher-BE interface-oxide species (Chapters 3 and 4) (Fig. 6.2). It is therefore concluded that the developing oxide films are constituted of stoichiometric ZrO_2 (*ZrO_2 component*) in combination with gradients of Zr-enrichment and O-deficiency in the region of the oxide-film adjacent to the metal/oxide interface. The degree of Zr-enrichment and O-deficiency decrease from the metal/oxide interface towards the oxide surface (*lower-BE interface-oxide component → higher-BE interface-oxide component*) (see Fig. 6.2).

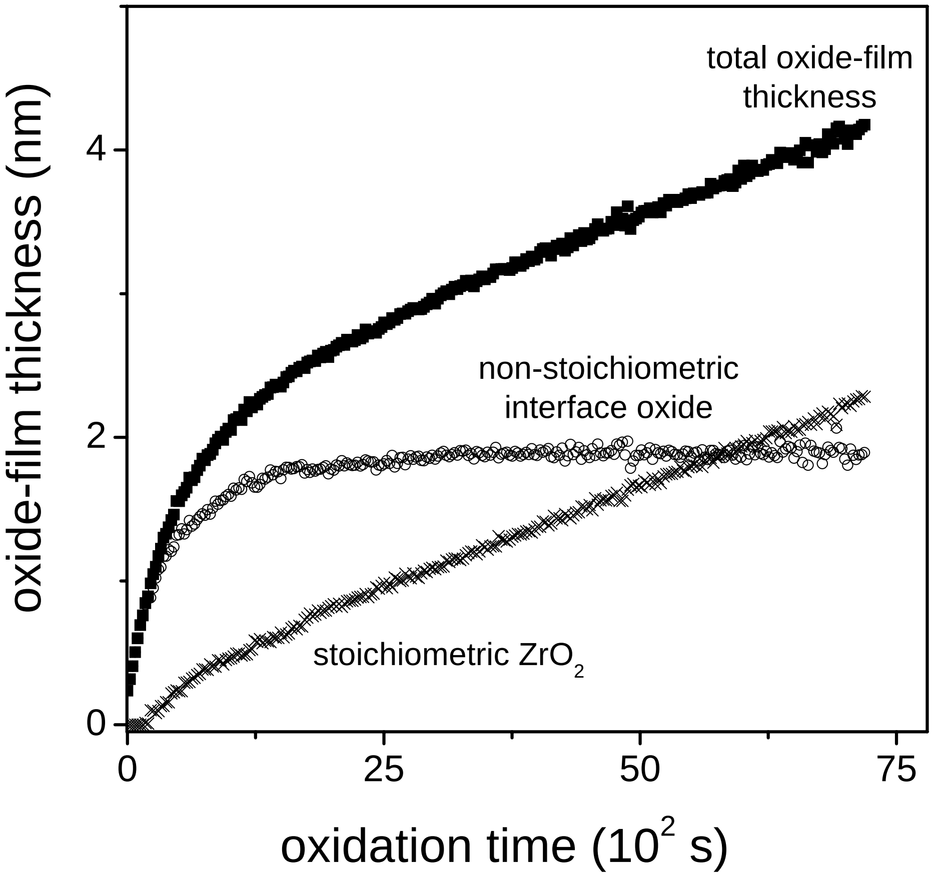

Figure 6.3. The total oxide-film thickness and corresponding individual thicknesses of the stoichiometric ZrO_2 top and non-stoichiometric oxide bottom sublayers, as a function of oxidation time, for the oxidation of the bare Zr substrate at 573 K and $pO_2 = 2\times10^{-6}$ Pa. The individual oxide growth curves were obtained from in situ, multi-wavelength ellipsometry. The ZrO_2 top sublayer and the Zr-enriched bottom sublayer correspond with the stoichiometric ZrO_2 and the sum of the lower-BE and higher-BE interface-oxide species as identified with AR-XPS, respectively (Fig. 6.2).

Two different oxide-film growth regimes have been recognised for the oxidation of the bare Zr substrate: a short, initial regime of very fast oxide-film growth, which is followed by a second stage of much slower, but continued oxide-film growth for oxidation temperatures higher than 423 K (Chapters 3 and 4 and Fig. 6.3).

As evidenced by both XPS and ellipsometry, initial oxide formation on the bare Zr substrate starts with the nucleation and rapid growth of a Zr-enriched and O-deficient Zr-oxide with an overall O/Zr-ratio of the oxide film lower than 2 (the initial O/Zr-ratio decreases with increasing temperature). At the onset of the second, slow oxidation stage, the growth rate of the non-stoichiometric oxide sublayer levels off, attaining a constant 'limiting' thickness that increases with increasing temperature (Chapter 4). Subsequent, continued (for 423 K < T < 523 K) growth occurs by the approximately linear overgrowth of stoichiometric ZrO_2 (the constant growth rate increases with increasing temperature) (Fig. 6.3).

At elevated temperatures of T > 573 K, the formation and continued growth of stoichiometric ZrO_2 competes with the dissolution and subsequent inward diffusion of oxygen into the Zr substrate that is accompanied by a partial decomposition of the developing oxide film (Chapter 4). The enhanced dissolution of O into the Zr substrate for T > 573 K is due to the associated increase of the maximum amount of oxygen that can be dissolved in α-Zr in combination with a significant increase of the oxygen dissolution rate for T > 573 K.

The mechanism of initial oxide-film growth on the bare Zr substrate was investigated by modelling the kinetics of oxide-film growth as a function of the oxidation time, temperature and pO_2 (see Chapter 5). To this end, a couple current description for the fluxes of Zr cations and electrons (by both tunnelling and thermionic emission) in a homogeneous surface-charge field comprising the growing oxide film were considered, while adopting the oxide-oxygen work function (i.e. the energy difference between the bottom of the conduction band in the oxide and the O^- level of the adsorbed oxygen), the metal-oxide work function (i.e. the energy difference between the bottom of the conduction band in the oxide and the Fermi-level of the metal) and the rate-determining energy barrier for cation motion, as fit parameters. The calculated growth curves are in very good agreement with the experimental growth curves for the initial oxidation within the temperature and pO_2 ranges of 304 – 573 K (for which the dissolution of oxygen into the Zr substrate can be neglected) and 1.3×10^{-6} – 1.3×10^{-4} Pa, respectively (Fig. 6.4).

It follows that, for all pO_2 and temperatures studied, the oxide-film growth is limited by the electric-field enhanced migration of Zr cations into or through the developing oxide

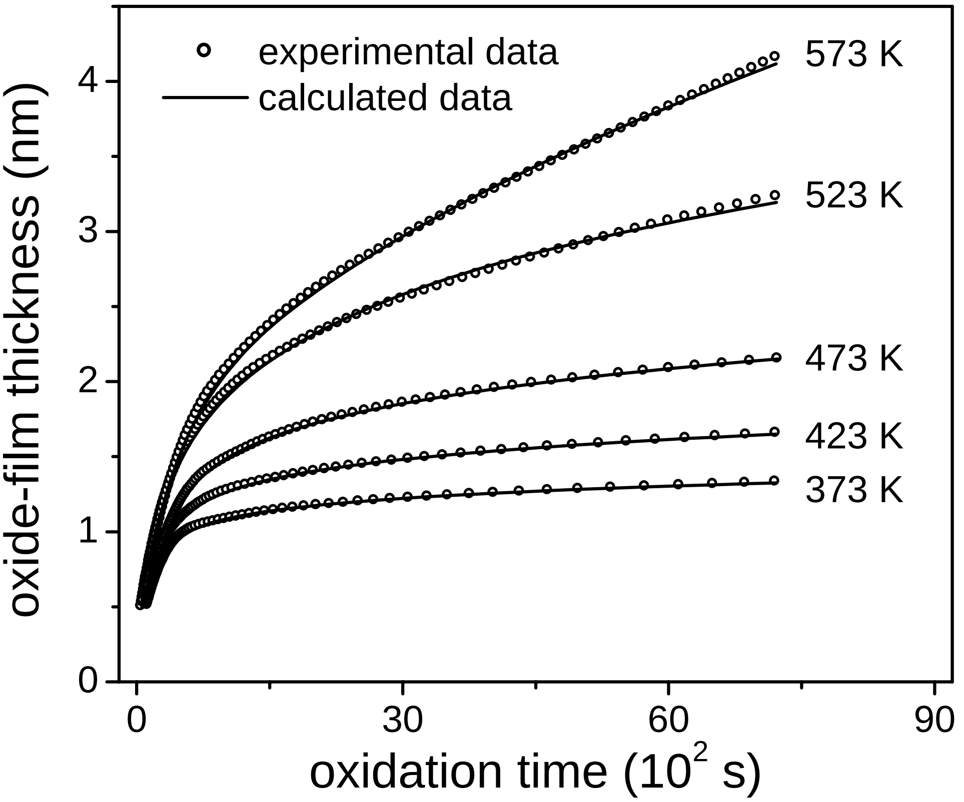

Figure 6.4. Oxide-film thickness as a function of oxidation time for zirconium oxidation at partial oxygen pressure $pO_2 = 2\times10^{-6}$ Pa and T = 373, 423, 473, 523 and 573 K. The fitted growth curves are represented by the lines; the experimental oxide-film thickness data (as determined from in situ ellipsometry) are represented by the open markers. The calculated growth curves have been obtained by adopting a coupled current description for the fluxes of Zr cations and electrons (by both tunnelling and thermionic emission) in a homogeneous surface charge field comprising the growing oxide film (and taking the rate-determining energy barrier for cation motion, and the metal-oxide and oxide-oxygen work functions, as fit parameters).

film. For oxide film thicknesses up to about 2 nm, electron tunnelling transport occurs at a much faster rate than the intrinsic ionic transport (with large, nearly equal forward and reverse electron tunnelling currents). Above this critical oxide-film thickness (and only for relatively elevated temperatures of $T \geq 523$ K, see Fig. 6.4), the net electronic current by tunnelling drops to zero, and the much slower electron transport by thermionic emission remains. Then, this electron transport by thermionic emission across the developing oxide film co-*determines* the growth rate, while the cation transport remains rate-*limiting*. The electric-field-assisted forward motion of cations into and through the developing oxide film becomes already strongly reduced during the initial, fast growth regime, because the strength of the established electric field due to the kinetic potential decreases with increasing oxide-film thickness. As indicated by the model calculations, the gradual transformation of the initially amorphous, overall non-stoichiometric oxide film with increasing temperature into a crystalline oxide film predominantly constituted of crystalline ZrO_2 film (see chapters 3 and 4) is associated with a gradual increase of the rate-determining energy barrier for cation motion, as well as a gradual increase of the metal-oxide work function in combination with a decrease of the oxide-oxygen work function. A higher pO_2 for the oxidation at room temperature leads to an increase of the density of electron acceptor levels provided by adsorbed oxygen species at the oxide surface, which is accompanied by an increase of the density of chemisorbed, negatively charged oxygen species on the developing oxide surface during the initial growth regime. Consequently, the magnitude of the electric field due to the approximate Mott potential increases with increasing pO_2 for the oxidation at room temperature (resulting in an increase of the initial growth rate and an increase of the thickness attained at the onset of the slow growth stage).

Chapter 7

Zusammenfassung: Anfangsstadien der Oxidation von Zirkonium

Dünne Zirkoniumoxidschichten (< 10 nm) sind aufgrund ihrer spezifischen physikalischen und chemischen Eigenschaften (z.B. guter Korrosionsschutz, gute thermische und mechanische Belastbarkeit, hohe dielektrische Konstante, große Bandlücke) von großer technischer Bedeutung in vielen Anwendungsgebieten wie Katalyse, Mikroelektronik oder Oberflächentechnik. Um die jeweils gewünschten Eigenschaften für diese dünnen Oxidschichten, die beispielsweise durch thermische Oxidation von blanken Zr-Substraten hergestellt werden, gezielt einstellen zu können, ist ein tiefgehendes Verständnis des Oxidationsprozesses erforderlich, z.B. der Wachstumsmechanismen und der sich ergebenden Mikrostruktur (sowie Morphologie, Kristallstruktur oder chemische Zusammensetzung) in Abhängigkeit der Oxidationsbedingungen.

Im Laufe dieser Arbeit wurden die Anfangsstadien der Oxidation von blanken, polykristallinen Zr-Substraten mit Hilfe winkelabhängiger Röntgen-Photoelektronen-Spektroskopie (AR-XPS) und *in situ* Ellipsometrie mit mehreren gleichzeitig verwendeten Wellenlängen unter verschiedenen Oxidationsbedingungen (d.h. Oxidationszeit, Sauerstoffpartialdruck und Temperatur) untersucht. Alle Oxidationsexperimente wurden unter kontrollierten Bedingungen in einer UHV Reaktionskammer durchgeführt (Basisdruck < 2.5×10^{-8} Pa), die mit einem Ellipsometer mit mehreren verwendeten Wellenlängen zur *in situ* Bestimmung der Wachstumskinetik der Oxidschicht ausgestattet ist. Diese Kammer für das Wachstum der dünnen Oxidschichten ist direkt mit der UHV Kammer (Basisdruck < 5×10^{-8} Pa) für die AR-XPS Analyse gekoppelt. Wegen der hohen Reaktivität mit der Umgebung sind polykristalline Zr-Substrate immer mit einer natürlichen Oxidschicht bedeckt (mehrere Nanometer dick), wenn sie in das UHV eingeführt werden. Um diese Schicht zu entfernen, werden die Zr-Substrate vor der Oxidation mit 3 kV Ar^+ Ionen besputtert (im weiteren als *blanke* Proben bezeichnet). Anschließend wurden die Proben in reinem Sauerstoff bei verschiedenen Temperaturen (T) und Sauerstoffpartialdrücken (pO_2) zwischen 300 K und 773 K und 1.3×10^{-7} – 1.3×10^{-4} Pa oxidiert.

Mit Hilfe von AR-XPS wurden Dicke, Aufbau und Zusammensetzung der gewachsenen Oxidschichten bestimmt. Für die quantitative Analyse der gemessenen XPS

Spektren wird eine genaue Beschreibung des individuellen Untergrundes inelastisch gestreuter Elektronen zu jedem Photoelektronenpeak benötigt. Deshalb wurde eine neue Methode zur Rekonstruktion der verschiedenen Anteile des Spektrums aus dem gemessenen XPS Spektrum entwickelt, die auf der Faltung von physikalisch realistischen Funktionen für die Röntgenstrahlenverteilung, das Rumpfelektronenniveau des Hauptpeaks, die Streuquerschnitte für intrinsische und extrinsische Anregungen und die experimentelle Verbreiterung beruht (Kapitel 2). Oberflächeneffekte wurden durch die Beschreibung des Materials als ein Substrat, das mit einer dünnen Oberflächenschicht des selben Materials, aber mit unterschiedlichen Eigenschaften der intrinsischen und extrinsischen Photeelektronenanregung, bedeckt ist, berücksichtigt. Die Rekonstruktion der gemessenen Zr 3*d* XPS Spektren, die von metallischem Zr und von ZrO_2 aufgenommen wurden (siehe Abb. 7.1a bzw. 7.1b), hat gezeigt, dass ca. 28% bzw. 21% der gesamten intrinsischen Photoelektronenintensität (für die Quantifizierung erforderlich) nicht im Hauptpeak enthalten, sondern auf Oberflächen- und Volumenplasmonen verteilt sind. Diese Rekonstruktionsmethode wurde weiterentwickelt und auf alle gemessenen Zr 3*d* XPS Spektren übertragen und angewendet, die von den oxidierten Zr-Substraten (d.h. Zr-Metall bedeckt mit einer dünnen Schicht Zirkoniumoxid) aufgenommen wurden. Die so erhaltenen verlustfreien primären Intensitäten (PZL: Primary zero loss) der metallischen und oxidischen Komponenten wurden verwendet, um die chemische Zusammensetzung (d.h. das O/Zr-Verhältnis), die Konstitution und die Dicke der gewachsenen Oxidschichten zu bestimmen (Kapitel 3 und 4).

In situ Ellipsometrie mit mehreren Wellenlängen wurde benutzt, um die Wachstumskinetik der Oxidschichten sowie die optischen Eigenschaften von Zirkoniummetallsubstraten und Zr-Oxidschichten zu bestimmen. Hierzu wurde ein Modell für das Substrat-Schicht-System entwickelt das die gemessenen Änderungen in den ellipsometrischen Parametern Ψ und Δ als eine Funktion der Oxidationszeit in dem Wellenlängenbereich zwischen 300 und 700 nm beschreibt. Die gemessenen Ellipsometriedaten konnten nur durch ein Modell akkurat gefittet werden, das ein Zr-Substrat enthält, welches mit einer zweischichtigen Oxidstruktur bedeckt ist (siehe Abb. 7.2b). Diese enthält eine Unterschicht aus zwei unterschiedlichen unstöchiometrischen Zr-Oxiden und eine Oberschicht (nahe der Oberfläche) aus stöchiometrischen ZrO_2 (Kapitel 3 und 4). Die Anordnung der effektiven Tiefen und die einzelnen Unterschichtdicken der unstöchiometrischen und der stöchiometrischem Oxidspezies in der entstehenden

Oxidschicht, die mit Ellipsometrie ermittelt wurden, stimmen gut mit den entsprechenden Ergebnissen überein, die *unabhängig* davon mit AR-XPS gewonnen wurden (siehe unten).

Anwendung der oben erwähnten Techniken und Benutzen der geeigneten Quantifizierungsmethoden führten zu den folgenden Ergebnissen für die Anfangsstadien der Oxidation von blanken, polykristallinen Zr-Substraten:

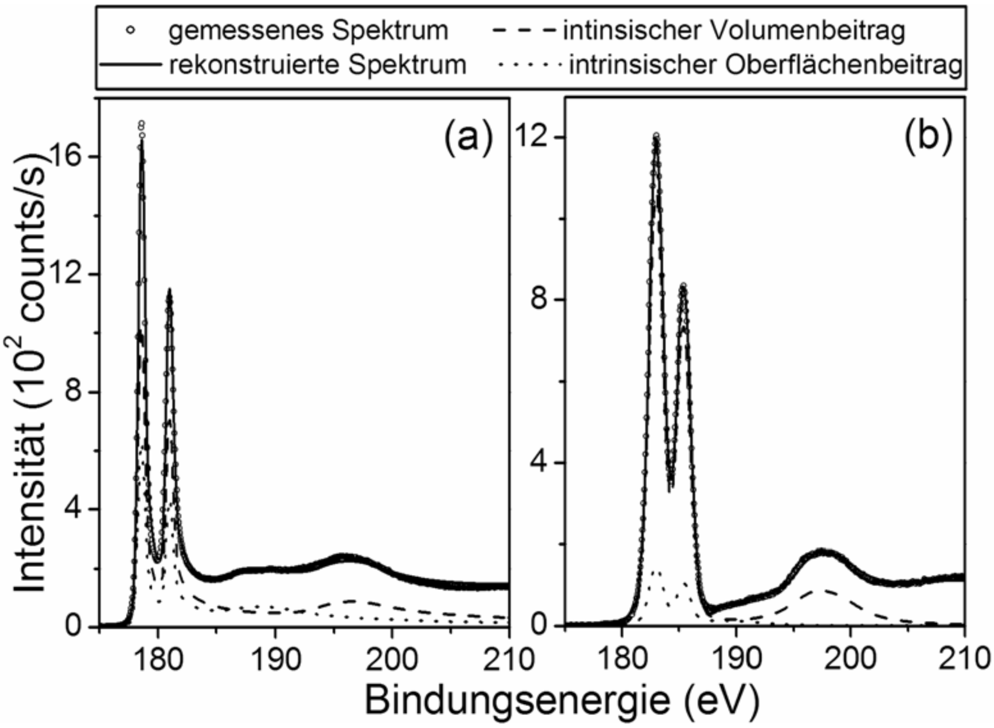

Abbildung 7.1. Die experimentellen und berechneten (d.h. rekonstruierten) Zr 3*d* XPS Spektren von **(a)** Zirkoniummetall und **(b)** Zirkoniumoxid.

Die detaillierte Analyse von gemessenen Zr 3*d* XPS Spektren des oxidierten Zr-Substrats zeigt die Anwesenheit von *drei* verschiedenen chemischen Spezies in der Oxidschicht (siehe Abb. 7.2): eine oxidische und zwei schwächere suboxidische Komponenten (bezeichnet als ZrO_2, sowie Grenzflächenoxid mit niedrigerer bzw. höherer Bindungsenergie (BE)). Basierend auf den Ergebnissen der AR-XPS-Untersuchungen konnte eine Darstellung der effektiven Tiefen der verschiedenen Spezies entwickelt werden; dabei liegt das stöchiometrische ZrO_2 an der äußeren Oxidoberfläche, wogegen beide Grenzflächenoxide in einer Tiefe zwischen der des Zr-Substrats und der äußeren Oberflächenregion des stöchiometrischen ZrO_2 liegen: Das Grenzflächenoxid mit dem niedrigeren BE-Wert liegt näher am Zr-Substrat als das mit dem höheren BE-Wert (Kapitel 3 und 4) (Abb. 7.2). Daraus wird die Schlussfolgerung gezogen, dass sich die entstehende Oxidschicht zusammensetzt aus stöchiometrischem ZrO_2 und einem Bereich an der Metall-

Oxid Grenzfläche, in dem sich Gradienten von Zr-Anreicherung und O-Verarmung befinden. Die Ausmaße der Zr-Anreicherung und O-Verarmung fällen von der Metall-Oxid Grenzfläche hin zur Oxidoberfläche ab (siehe Abb. 7.2).

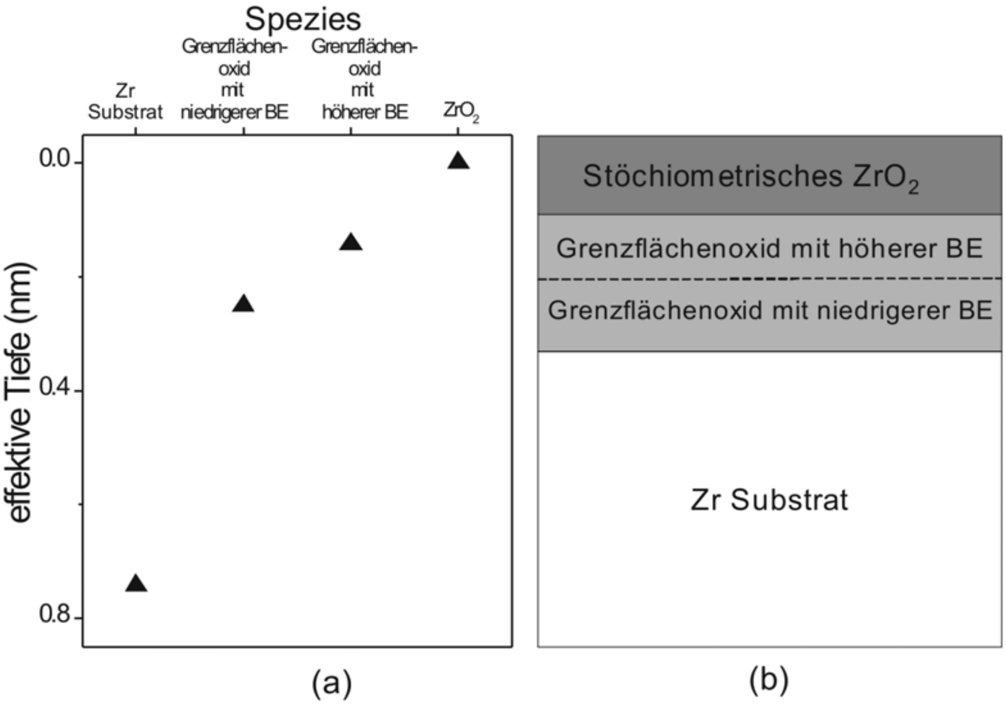

Abbildung 7.2. Der Aufbau einer Zirkoniumoxidschicht, die auf einem Zirkoniumsubstrat durch trockene, thermische Oxidation gewachsen ist: **(a)** Auftragung der effektiven Tiefe des Zr-Substrats nach der Oxidation für 7200 s bei $T = 304$ K und $pO_2 = 1.3\times10^{-5}$ Pa; **(b)** Schematische Darstellung des Aufbaus der Oxidschicht, wie sie durch AR-XPS und in situ Ellipsometrie ermittelt wurde.

Zwei verschiedene Stadien des Oxidschichtwachstums wurden bei der Oxidation von blanken Zr-Substraten beobachtet: ein kurzes, anfängliches Stadium mit sehr schnellem Oxidschichtwachstum, auf das ein zweites Stadium mit viel langsameren aber kontinuierlichem Oxidschichtwachstum bei Oxidationstemperaturen größer als 423 K folgt (Kapitel 3 und 4).

Wie sowohl durch XPS als auch durch Ellipsometrie gezeigt wurde, beginnt die erste Oxidbildung auf dem blanken Zr-Substrat mit Keimbildung und schnellem Wachstum von einem Zr-Oxid, das mit Zr angereichert und an O verarmt ist, mit einem O/Zr-Verhältnis, das insgesamt kleiner als zwei ist (das anfängliche O/Zr-Verhältnis fällt mit steigender Temperatur ab). Zu Beginn des zweiten, langsamen Oxidationsstadiums fällt die Wachstumsrate der unstöchiometrischen Oxidunterschicht ab, wobei eine konstante, ‘begrenzende’ Dicke erreicht wird, die mit steigender Temperatur zunimmt (Kapitel 4). Dann findet (nur für 423 K < *T* < 523 K) kontinuierliches, etwa lineares Wachstum von stöchiometrischem ZrO_2 an der Oberfläche statt (die bezügliche Wachstumsrate nimmt mit steigende Temperatur zu).

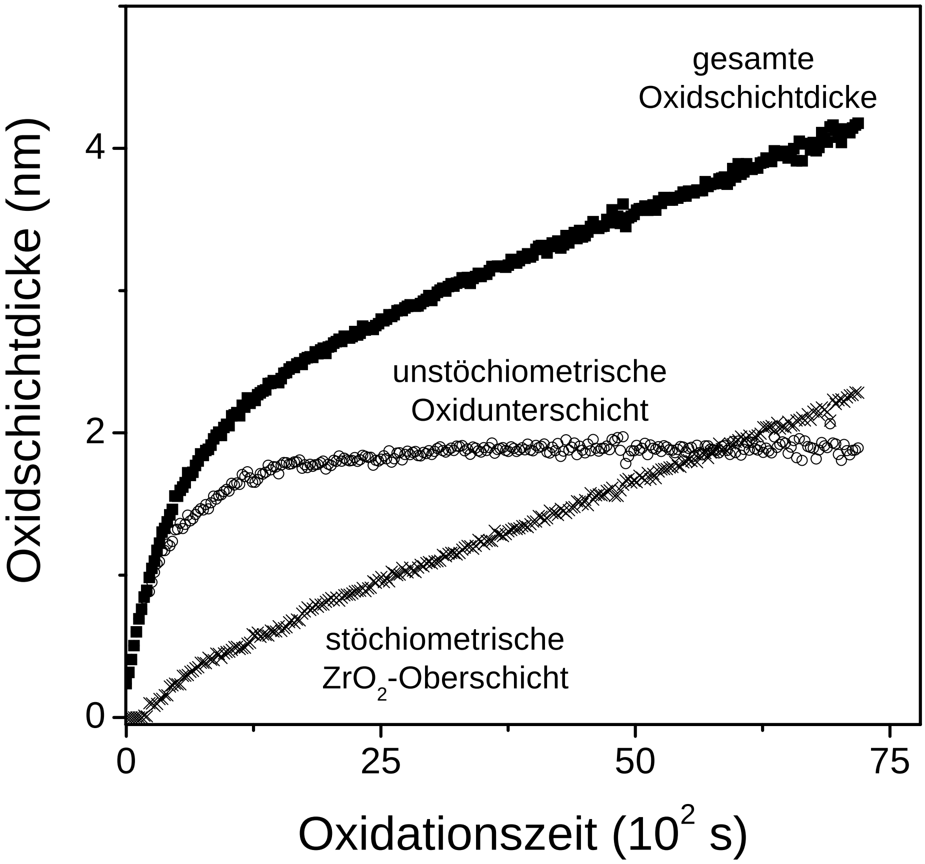

Abbildung 7.3. Die gesamte Oxidschichtdicke und die dazugehörigen Einzeldicken der stöchiometrischen ZrO_2-Oberschicht und der unstöchiometrischen Oxidunterschicht als Funktion der Oxidationszeit für die Oxidation von blanken Zr-Substraten bei 573 K und $pO_2 = 2\times10^{-6}$ Pa. Die einzelnen Oxidwachstumskurven wurden durch in situ Ellipsometrie mit mehreren verwendeten Wellenlängen erhalten. Die ZrO_2-Oberschicht und die mit Zr angereicherte Unterschicht sind identisch mit dem stöchiometrischen ZrO_2 und der Summe der Grenzflächenoxide mit hoher und niedriger BE, die mit AR-XPS gefunden wurden (Abb.7.2).

Bei höheren Temperaturen von *T* > 573 K konkurrieren Bildung und kontinuierliches Wachstum von stöchiometrischem ZrO_2 mit der Aufnahme und ständigen Nachdiffusion von Sauerstoff in das Zr-Substrat, was mit einem teilweisen Abbau der entstehenden Oxidschicht einhergeht (Kapitel 4). Die erhöhte Aufnahme von O in das Zr-Substrat bei *T* > 573 K geschieht auf Grund der ansteigenden Menge von Sauerstoff, die in α-Zr gelöst werden kann und einer erhöhten Auflösungsgeschwindigkeit von Sauerstoff bei $T > 573$ K.

Der Mechanismus des anfänglichen Oxidschichtwachstums auf blanken Zr-Substraten wurde durch Modellierung der Kinetik des Oxidschichtwachstums als Funktion der Oxidationszeit, der Temperatur und des pO_2 untersucht (siehe Kapitel 5). Dafür wurde eine Beschreibung gekoppelter Ströme für die Flüsse von Zr-Kationen und Elektronen (durch Tunneln und thermionische Emission) unter Einfluss eines homogenen Oberflächenladungsfeldes innerhalb der wachsenden Oxidschicht betrachtet. Die Oxid-Sauerstoff-Austrittsarbeit (d.h. der Energieunterschied zwischen der unteren Grenze des Leitungsband in dem Oxid und dem O^--Niveau des adsorbiertem Sauerstoffs), die Metall-Oxid-Austrittsarbeit (d.h. der Energieunterschied zwischen der unteren Grenze des Leitungsbandes in dem Oxid und dem Ferminiveau des Metalls) und die Aktivierungsenergie für den Kationentransport wurden als Fitparameter verwendet. Für das Anfangsstadium des Oxidschichtwachstums in dem Temperaturbereich von 304 – 573 K (in dem die Auflösung von Sauerstoff in das Zr-Substrat vernachlässigt werden kann) und dem Druckbereich von 1.3×10^{-6} – 1.3×10^{-4} Pa stimmen die berechneten Wachstumskurven sehr gut mit den experimentellen Wachstumskurven überein (Abb. 7.4).

Es folgt, dass das Oxidschichtwachstum für alle untersuchten pO_2 und Temperaturen durch die Bewegung von Zr-Kationen in oder durch die wachsende Oxidschicht unter verstärktem Einfluss des elektrischen Feldes begrenzt ist. Für Oxidschichten von bis zu 2 nm, ist die Elektronentransportrate durch Tunneln viel höher als die intrinsische Ionentransportrate (und die Tunnelflüsse von Elektronen in beide Richtungen durch die wachsende Oxidschicht sind groß und etwa gleich). Oberhalb der kritischen Oxidschichtdicke (und nur für relativ hohe Temperaturen oberhalb 523 K, siehe Abb. 7.4) fällt der Nettotunnelstrom auf Null ab und nur der viel langsamere Elektronentransport durch thermionische Emission verbleibt. Ab dann wird der Elektronentransport durch thermionische Emission durch die wachsende Oxidschicht für die Schichtwachstumsrate *mitbestimmend*, während der Kationentransport unter Einfluss des elektrischen Feldes geschwindigkeits*limitierend* bleibt.

Der Kationentransport in und durch die wachsende Oxidschicht unter Einfluss des elektrischen Feldes wird schon während des Anfangsstadiums mit sehr hoher Wachstumsrate stark reduziert, weil die Stärke des sich einstellenden elektrischen Feldes, zurückzuführen auf das kinetische Potential, mit zunehmender Oxidschichtdicke abnimmt. Der durch die Modellrechnungen gegebene Anstieg der Energiebarriere für die Kationenbewegung, so wie

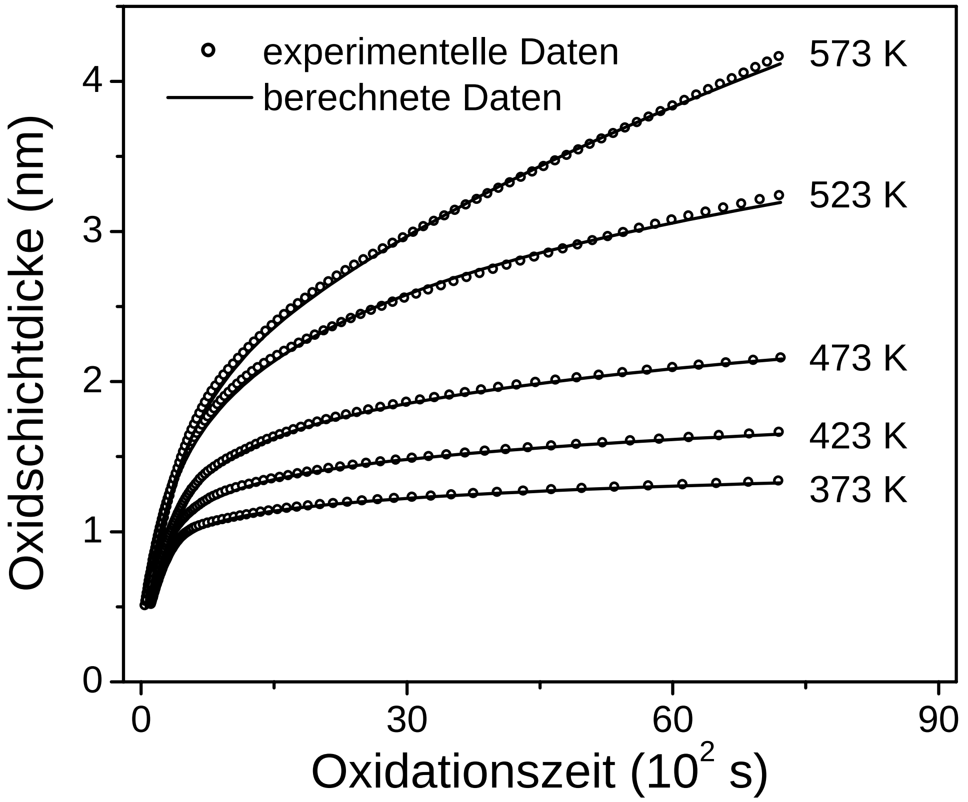

Abbildung 7.4. Oxidschichtdicke als Funktion der Oxidationszeit für die Oxidation von Zirkonium bei einem Sauerstoffpartialdruck von $pO_2 = 2\times10^{-6}$ Pa und T = 373, 423, 473, 523 and 573 K. Die durchgezogenen Linien repräsentieren die theoretischen Wachstumskurven; die offenen Kreise stellen die experimentellen Daten dar (die aus den in situ ellipsometrische Daten bestimmt wurden). Die theoretischen Wachstumskurven wurden mit Hilfe einer Beschreibung gekoppelter Ströme für die Flüsse von Zr-Kationen und Elektronen (durch Tunneln und thermionische Emission) unter Einfluss eines homogenen Oberflächenladungsfeldes innerhalb der wachsenden Oxidschicht berechnet. Die Oxid-Sauerstoff-Austrittsarbeit (d.h. der Energieunterschied zwischen der unteren Grenze des Leitungsbandes in dem Oxid und dem O^--Niveau des adsorbiertem Sauerstoffs), die Metall-Oxid-Austrittsarbeit (d.h. der Energieunterschied zwischen der unteren Grenze des Leitungsbandes in dem Oxid und dem Ferminiveau des Metalls) und die Aktivierungsenergie für den Kationentransport wurden dabei als Fitparameter verwendet.

der Anstieg der Metall-Oxid-Austrittsarbeit in Zusammenhang mit dem Abfall der Oxid-Sauerstoff-Austrittsarbeit, mit ansteigender Temperatur hängt mit der stufenweisen Umwandlung der anfänglich amorphen, insgesamt unstöchiometrischen Oxidschicht in eine Schicht von kristallinem ZrO_2 zusammen. Ein höherer Sauerstoffpartialdruck bei der Raumtemperaturoxidation führt zu einem Anstieg der Dichte der Elektronenakzeptorniveaus, die von adsorbierten Sauerstoffspezies an der Oxidoberfläche angeboten werden. Der Anstieg der Dichte der Elektronenakzeptorniveaus resultiert in einem Anstieg von chemisorbierten, negativ geladenen Sauerstoffspezies an der wachsenden Oxidoberfläche während des Anfangsstadiums des Oxidschichtwachstums. Konsequenterweise steigt die Größe des elektrischen Feldes in der wachsenden Oxidschicht, zurückzuführen auf das kinetische Potential, bei Raumtemperaturoxidation mit ansteigendem Sauerstoffpartialdruck (wie belegt wird durch Anstiege von sowohl der anfänglichen Wachstumsrate als auch der Dicke, die zu Beginn des langsamen Wachstumsstadiums erreicht wird).

References.

[1] Fromhold A.T., Jr., *Theory of Metal Oxidation; Volume I – Fundamentals* (North-Holland, Amsterdam, 1976).

[2] Fehlner F.P., *Low-temperature oxidation* (Jon Wiley & Sons, New York, 1981).

[3] Fromm E, *Kinetics of Metal-Gas Interactions at low temperatures: hydriding, oxidation, poisoning* (Springer: Berlin, 1998; Chap. 5).

[4] Kofstad P., *High-temperature oxidation of metals* (John Wiley & Sons, Inc., New York, London, Sydney, 1966).

[5] Lawless K.R., *Rep. Prog. Phys.,* 1974, **34:** 231.

[6] Zelikman A.N., Krein O.E., Samsonov G.V., *Metallurgy of rare metals* (Jerusalem-Izrael Prog. F. Sci. Transl., 2 ed., 1966).

[7] Ondik H.M., Macmurdie H.F., *Phase diagrams for zirconium and zirconia system* (American Ceramic Society Inc., Westerville, Ohio, 1998).

[8] Kisi E.H., Howard C.J., *Crystal structures of zirconia phases and their inter-reaction* (in *Key Engineering Materials*, Vols. 153-154, 1998, pp. 1-36).

[9] Douglass D.L., Van Landuyt J., *Acta Met.,* 1965, **13:** 1069.

[10] Wilk G. D., Wallace R. M., Anthony J. M., *J. Appl. Phys.,* 2000, **87:** 484.

[11] Miller G.L., *Zirconium* (Butterworths scientific publication, London, 1954).

[12] Foster A.S., Sulimov V.B., Lopez Gejo F., Shluger A.L., Nieminen R.M., *Phys. Rev. B*, 2001, **64:** 224108.

[13] Jungblut B., Sicking G., Papachristos T., *Surf. Interface Anal.,* 1988, **13:** 135.

[14] Morant C., Sanz J. M., Galan L., Soriano L., Rueda F., *Surf. Sci.,* 1989, **218:** 331.

[15] Sen P., Sarma D. D., Budhani R. C., Chopra K. L., Rao C. N. R., *J. Phys. F.,* 1984, **14:** 565.

[16] West P.E., George P.M., *J. Vac. Sci. Thecnol. A,* 1987, **5(4):** 1124.

[17] Zhang C., Norton P.R., *J. Nucl. Mater.,* 2002, **300:** 7.

[18] Shirley D.A., *Phys. Rev. B,* 1972, **5:** 4709.

[19] Azzam R. M. A., Bashara N. M., *Ellipsometry and polarized light* (Norht-Holland: Amsterdam, 1987).

[20] Mott N.F., *Trans. Faraday Soc.,* 1947, **43:** 429.

[21] Cabrera N., Mott N.F., *Rep. Prog. Phys.,* 1949, **12:** 163.

[22] Evans U.R., *The Corrosion and oxidation of metals* (St. Martins Press, New York, 1960).

[23] Fromhold A.T., Jr., Cook E.L., *Phys. Rev.,* 1967, **158** (3): 600.

[24] Fromhold A.T., Jr., Cook E.L., *Phys. Rev.,* 1967, **163** (3): 650.

[25] Kurth M., Graat P.C. J., *Surf. Interface Anal.,* 2002, **34:** 220.

[26] Werner W.S.M., Cabela T., Zemek J., Jiricek P., *Surf. Sci.,* 2001, **470:** 325.

[27] Werner W.S.M., *Surf. Sci.,* 2003, **526:** L159.

[28] Doniach S., Sunjic M., *J. Phys. C,* 1970, **3:** 285.

[29] Hakansson K.L., Johansson H.I.P., Johansson L.I., *Phys. Rev. B,* 1993, **48:** 2623.

[30] Werner W.S.M., Tilinin I.S., Beilschmidt H., Hayek M., *Surf. Interface Anal.,* 1994, **21:** 537.

[31] Werner W.S.M., *Surf. Interface Anal.,* 1995, **23:** 737.

[32] Werner W.S.M., *J. Vac. Sci. Technol. A,* 1997, **15:** 465.

[33] Tougaard S., Hansen H.S., *Surf. Interface Anal.,* 1989, **14:** 730.

[34] Tougaard S., *Surf. Interface Anal.,* 1997, **25:** 137.

[35] Ashley J.C., Cowan J.J., Ritchie R.H., Anderson V.E., Hoelzl J., *Thin Solid Films,* 1979, **60:** 361.

[36] Lyapin A., Jeurgens L. P. H., Graat P. C. J., Mittemeijer E. J., *Surf. Interface Anal.,* 2004, **36 (8):** 989.

[37] Prieto P., Yuberto F., Elizalde E., Sanz J.M., *J. Vac. Sci. Technol. A,* 1996, **14:** 3181.

[38] Kralik B., Chang E.K., Louie S.G., *Phys. Rev. B,* 1998, **57:** 7027.

[39] Tanuma S., Powell C.J., Penn D.R., *Surf. Interface Anal.,* 1991, **17:** 911.

[40] *Matlab function reference* Vol.2, pp. 2-123 – 2-126 (The MathWorks Inc., 2001).

[41] Wagner C.D., Naumkin A.V., Kraut-Vass A., Allison J.W., Powell C.J., Rumble J.R., Jr. (Eds.), NIST Standard Reference Database 20, Version 3.2 (2002), (http://srdata.nist.gov/xps/).

[42] De Gonzalez C. O., Garcia E. A., *Surf. Sci.,* 1988, **193:** 305.

[43] Seah M.P., Gilmore I.S., Spencer S.J., *Surf. Interface Anal.,* 2001, **31:** 778.

[44] Kumar L., Sarma D.D., Krummacher S., *Appl. Surf. Sci.,* 1988, **32:** 309.

[45] Nishino Y., Krays A.R., Lin Y., Gruen D.M., *J. Nucl. Mater.,* 1996, **228:** 346.

[46] American Society for testing and materials, *Surf. Interface Anal.,* 1991, **17:** 899.

[47] Lyapin A., Graat P.C.J., *Surf. Sci.,* 2004, **552:** 160, (Chapter 2 in this thesis).

[48] Jeurgens L.P.H., Sloof W.G., Tichelaar F.D., Borsboom C.G., Mittemeijer E.J., *Appl. Surf. Sci.,* 2000, **161:** 139.

[49] Graat P.C.J., Somers M.A.J., Mittemeijer E.J., *Zeitschr. f. Metallkunde.,* 2002, **93 (6):** 532.

[50] Jeurgens L.P.H., Sloof W.G., Tichelaar F.D., Mittemeijer E.J., *Thin Solid Films*, 2002, **418:** 89.

[51] Jeurgens L.P.H., Sloof W.G., Tichelaar F.D., Mittemeijer E.J., *Surf. Sci.,* 2002, **506:** 313.

[52] Blumenthal W.B., *The chemical behaviour of zirconium* (London–Van Nostrand, 1958).

[53] Shannon R.D., *Acta Cryst.,* 1976, **A32:** 751.

[54] Jablonski A., Powell C.J., *Surf. Sci. Report.,* 2002, **47:** 33.

[55] Reilman R.F., Msezane A., Manson S. T., *J. Electron. Spectrosc. Relat. Phenom.,* 1976, **8,** 389.

[56] *Guide to Using WVASE32^{TM}* (J.A.Woolam Co., Inc., 1997, pp.165-168).

[57] Tröger W.E., *Optische Bestimmung der gesteinsbildenden Minerale*, *5th ed.* (E.Schweizerbart'sche Verlagsbuchhandlung, Stuttgart 1982, Part 1).

[58] Levichkova M., Mankov V., Starbov N., Karashanova D., Mednikarpov B., Starbova K., *Surf. Coat. Technol.,* 2001, **141:** 70 .

[59] De Boer D.K.G., Haas C., Sawatzky G.A., *Phys. Rev. B.,* 1984,**48:** 4401 .

[60] Snijders P.C., Jeurgens L.P.H., Sloof W.G., *Surf. Sci.,* 2002, **496:** 97.

[61] Schmiedgen M., Graat P.C.J., Baretzky B., Mittemeijer E.J., *Thin Solid Films,* 2002, **415:** 114.

[62] Jeurgens L.P.H., Sloof W.G., Tichelaar F.D., Mittemeijer E.J., *J. Appl. Phys.,* 2002, **92:** 1649.

[63] Schäfer J., Atkins C.J., *J. Phys. Condens. Matter.,* 1991, **3:** 2907.

[64] Lyapin A, Jeurgens L.P.H., Graat P.C.J., Mittemeijer E.J., *J. Appl. Phys.,* 2004, **96 (12):** 7126 (Chapter 3 in this thesis).

[65] Chang J.P., Lin Y.-S., Chu K., *J. Vac. Sci. Technol. B,* 2001, **19:** 1782.

[66] Jeurgens L.P.H., Lyapin A., Mittemeijer E.J., *The mechanism of low-temperature oxidation of zirconium*, submitted for publication (Chapter 5 in this thesis).

[67] Powel C.J., *Appl. Surf. Sci.,* 1995, **89:** 141.

[68] Jeurgens L.P.H., Sloof W.G., Borsboom C.G., Tichelaar F.D., Mittemeijer E.J., *Appl. Surf. Sci.,* 2000, **161:** 139.

[69] Zehringer R., Hauert R., Oelhafen P., Güntherodt H.-J., *Surf. Sci.,* 1989, **215:** 501.

[70] Kim K.S., Winograd N., *Surf. Sci.,* 1974; **43:** 625.

[71] Robert T., Bartel M., Offergeld G., *Surf. Sci.,* 1972, **33:** 123.

[72] Wandelt K., *Surf. Sci. Rep.,* 1982, **2:** 1.

[73] Abriata J.P., Garcés J., Versaci R., *Bull. All. Phase Diagr.*, 1986, **7:** 116.

[74] Graat P.C.J., Somers M.A.J., Vredenberg A.M., Mittemeijer E.J., *J. Appl. Phys.,* 1997, **82:** 1416.

[75] Roosendaal S.J., Vredenberg A.M., Habraken F.H.P.M., *Phys. Rev. Lett.,* 2000, **84:** 3366.

[76] Seah M.P., *Practical Surface Analysis.* (Vol.1, 2nd Ed. Eds. Briggs D. and Seah M.P., Wiley, Chichester, 1990, p. 201).

[77] Kooi B.J., Somers M.A.J., Mittemeijer E.J., *Thin Solid Films*, 1996, **281-282:** 488.

[78] Kurth M., *The initial Oxidation of Mg* (Thesis, Stuttgart University, Stuttgart, Germany), 2004.

[79] Lyapin A., Jeurgens L.P.H., Mittemeijer E.J., *Acta Mat.,* 2005, **53:** 2925 (Chapter 4 in this thesis)

[80] Grajewski V., Fromm E., in *Science of Ceramic Interfaces*, edited by Nowotny J. (Elsevier, Amsterdam, 1991), p. 487.

[81] Jackson J.D., *Classical Electrodynamics* (John Wiley & Sons, New York, 1975, pp. 155-156).

[82] Douglass D.L., Wagner C., *J. Electrochem. Soc.* 1966, **113:** 671.

[83] Yoo H.-I., Koo B.-J., Hong J.-O., Hwang I.-S., Jeong Y.-H., *J. Nucl. Mat.,* 2001, **299:** 235

[84] MATLAB version 6.1.0.450, Release 12.1 (The MathWorks Inc., Natick, 2001).

[85] Cimpoiasu E., Tolpygo S.K., Liu X., Simonian N., Lukens J.E., Likharev K.K., Klie R.F. and Zhu Y., *J. Appl. Phys.,* 2004, **96**: 1088.

[86] Snijders P.C., Jeurgens L.P.H. and Sloof W.G., submitted, 2005.

List of publications

1. A. Lyapin, P. C. J. Graat „Quantitative analysis of the X-ray photoelectron spectrum of zirconium" *Surface and Interface Analysis* 2004, **36 (8):** 812-815.
2. A. Lyapin, L. P. H. Jeurgens, P. C. J. Graat, E. J. Mittemeijer „Ellipsometric and XPS study of the initial oxidation of zirconium at room temperature" *Surface and Interface Analysis* 2004, **36 (8):** 989-992.
3. A. Lyapin, P. C. J. Graat „Quantitative Analysis of the X-ray Photoelectron Spectra of Zirconium and Zirconium Oxide" *Surface Science* 2004, **552:** 160-168 (Chapter 2 in this thesis).
4. A. Lyapin, L. P. H. Jeurgens, P. C. J. Graat, E. J. Mittemeijer „The initial, thermal oxidation of zirconium at room temperature" *Journal of Applied Physics* 2004, **96 (12):** 7126-7135 (Chapter 3 in this thesis).
5. A. Lyapin, L. P. H. Jeurgens, E. J. Mittemeijer „Effect of temperature on the initial, thermal oxidation of zirconium", *Acta Materialia* 2005, **53:** 2925 (Chapter 4 in this thesis).
6. L. P. H. Jeurgens, A. Lyapin, E. J. Mittemeijer "The mechanism of low-temperature oxidation of zirconium", submitted (Chapter 5 in this thesis)

Curriculum Vitae

Persönliches

Name	Andrey Lyapin, geb. Guinko
Geburtsdatum, -ort	07.10.1977, St.-Petersburg, Russland
Familienstand	verheiratet
Nationalität	russisch

Schulbildung

1984 – 1994	Allgemeinbildende Schule
Mai 1994	Abitur

Studium

Sep. 1994 – Jul. 1999	Studium der Chemie an der Universität St.-Petersburg (Russland) Fachbereich Analytische Chemie
Sep. 1998 – Jul. 1999	Diplomarbeit: „Adsorption concentration of phenols from natural waters“

Dissertation

Mär. 2001 – Aug. 2004	Doktorand am Max-Planck-Institut für Metallforschung und der Universität Stuttgart Thema: „Anfangsstadien der Oxidation von Zirconium“

Berufliche Tätigkeiten

Sep. 1999 – Feb. 2001	Regionales Analytisches Zentrum „Mekhanobr-Analyt“, St.-Petersburg Oberflächenanalytisches Laboratorium, Wissenschaftlicher Angestellter
seit Aug. 2004	Max-Planck-Institut für Eisenforschung GmbH, Düsseldorf Abteilung Grenzflächenchemie und Oberflächentechnik, Wissenschaftlicher Angestellter

Danksagung

Die vorliegende Arbeit wurde am Institut für Metallkunde der Universität Stuttgart und am Max-Planck-Institut für Metallforschung, Stuttgart, angefertigt.

Meinem Doktorvater Prof. Dr. Ir. E. J. Mittemeijer danke ich besonders für sein außergewöhnliches Engagement bei unseren Besprechungen, sowie generell für meine damit verbundene wissenschaftliche Förderung.

Mein besonderer Dank geht an meine Betreuer Dr. Peter C. J. Graat und Dr. Lars P. H. Jeurgens, welche ständig und unermüdlich für meine Fragen offen waren und von denen ich vieles Lernen durfte, was für die Durchführung dieser Arbeit unerlässlich war. Die Möglichkeit, praktisch jederzeit über die auftretenden Probleme zu diskutieren, war stets außerordentlich bereichernd und hilfreich.

Herzlich danken möchte ich auch allen Mitarbeitern des Max-Planck-Instituts für Metallforschung, die mir stets mit voller Unterstützung bei allen technischen Problemen zur Seite standen.

Bei meiner Frau Tatiana, sowie bei meiner Freunde, bedanke ich mich besonders für seelische Unterstützung.